Development of a New Reconstruction Algorithm for ANTARES Events and Application to a Search for Neutrino Point Sources

Entwicklung eines Algorithmus zur Rekonstruktion von Ereignissen im ANTARES Neutrinoteleskop und Anwendung bei der Suche nach Punktquellen

Der Naturwissenschaftlichen Fakultät
der Friedrich-Alexander-Universität Erlangen-Nürnberg
zur Erlangung des Doktorgrades Dr. rer. nat.

vorgelegt von
Kathrin Roensch
aus Erlangen

Als Dissertation genehmigt
von der Naturwissenschaftlichen Fakultät
der Friedrich-Alexander-Universität Erlangen-Nürnberg

Tag der mündlichen Prüfung:
Vorsitzender der Promotionskommission: Prof. Dr. Jörn Wilms
Erstberichterstatter: Prof. Dr. Ulrich Katz
Zweitberichterstatter: Prof. Dr. Gisela Anton

Abstract

One of the main goals of the ANTARES neutrino telescope is the discovery of high-energy cosmic neutrinos from celestial neutrino sources. This is achieved by detecting Cherenkov photons from charged secondaries created in neutrino-nucleon-interactions. These photons are e.g. emitted by a secondary muon that arises from a charged current interaction between a muon neutrino and an atomic nucleus. So far only limits for neutrino fluxes have been set and no high-energy neutrino event has been observed with the ANTARES detector. The IceCube experiment, located at the geographical South Pole, is by far larger ($\mathbb{O}(1\,\mathrm{km}^3)$) and thus more sensitive and looks at a complementary region of the universe. Two years ago the IceCube project reported the discovery of a $5.7\,\sigma$ excess of events between 50 TeV and 2 PeV within the detector [1, 2]. These were the first events detected with such high discovery potential; they were assigned to a diffuse cosmic neutrino flux. In order to register a neutrino event with a comparable certainty in the ANTARES detection volume ($\mathbb{O}(0.02\,\mathrm{km}^3)$), efficient neutrino reconstruction strategies are of crucial importance.

Therefore, serveral neutrino reconstruction strategies were developed within the ANTARES collaboration. In this context, the *AAFit* reconstruction strategy exhibits the best resolution and the most effective background suppression to date. For the recording period of 2007 to 2008 a median estimated angular resolution of $(0.53 \pm 0.08)^\circ$ was achieved [3]. The evaluation of the recorded data from 2007 until 2010 shows an angular resolution of $(0.43 \pm 0.10)^\circ$ for this reconstruction strategy [4]. *BBFit* represents an alternative strategy that performs much faster, but with less accuracy. Its reachable angular error for an analysis of 2007 data varied between 2° and 7°, depending on which declination band has been investigated [5, 6].

The *BBFit* algorithm primarily uses geometrical considerations to gain information on the probability density of the Cherenkov photons. This density mainly depends on the expected arrival time of photons in the photomultipliers. Additionally, this density is related to the hit amplitude and the distance of a track guess to a hit photomultiplier. The *AAFit* strategy mainly performs with probability density functions (PDFs) that are generated from Monte-Carlo-tables. These tables are filled with the expected arrival time of simulated photons concerning their pulse amplitude in the photomultipliers. This thesis details a new approach, a reconstruction strategy called *OSFFit*.

It is applied on the 2007-2008 dataset. *OSFFit* is based on maximum likelihood fits; one of its key elements is the PDF *SeaPdf*, that is set up by heuristic functions which describe the expected arrival time of photons. Furthermore, a difference in the *SeaPdf* to conventional PDFs available for ANTARES is the usage of an estimated neutrino energy. *BBFit* serves as the first rough track guess for *OSFFit*. This thesis describes the development and improvement of *OSFFit*. Furthermore, *OSFFit* was studied to determine whether it yields high performance in reconstruction, whether it can be specialised to diverse event characteristics and whether it is able to complement the *AAFit* results in certain circumstances.

The analysis of the results for *OSFFit* shows that the median angular error α for cosmic neutrinos with an E^{-2} spectrum is 0.32° with a neutrino efficiency of 84 % with respect to a reference data sample. This is approximately competitive to *AAFit* with a quality cut $\Lambda > -5.2$ with $\alpha = 0.30^\circ$ at 83 % neutrino efficiency. However, after adjusting a test data sample on the same suppression rate of background (1 atmospheric muon in 20.7 days of lifetime), the efficiency of *OSFFit* drops nearly in half, whereas *AAFit* keeps its value. The resulting median angular error of *OSFFit* for neutrinos is $\alpha = 0.29^\circ$ and that of *AAFit* with its complete offical cuts ($\Lambda > -5.2$, $\beta < 1^\circ$ and $\theta > 90^\circ$ [7, 8]) is 0.34°.

A detailed study demonstrates that *OSFFit* can save approximately $2\,\% - 5\,\%$ of the neutrino events discarded by *AAFit*. These amounts enlarge *AAFit's* efficiency output at an unvaried median angular error. Furthermore, in case of a data sample that passed the quality cuts of both algorithms, *OSFFit* is more sensitive than *AAFit* for several event types.

Finally, *OSFFit* was used to search for an excess of cosmic neutrino signals in a 20° cone around 24 γ-ray sources. Corresponding background mainly consists of atmospheric neutrinos. With strong constraints on the background it was not possible to find evidences for a cosmic neutrino emission on a $3\,\sigma$ confidence level. The lowest median upper limit on a 90 % CL that could be reached for Monte Carlo data was $\Phi^{\mathrm{up}}_{90\,\%} = 1.103 \cdot 10^{-7} \cdot \mathrm{GeV}^{-1} \cdot \mathrm{cm}^{-2} \cdot \mathrm{sec}^{-1}$ for the stellar cluster HESS J1614-518 [9] and a flux assumption of $\Phi_{\mathrm{ref}} = \Phi_0 \cdot E^{-2} = 1 \cdot 10^{-7} \cdot E^{-2} \cdot \mathrm{GeV} \cdot \mathrm{cm}^{-2} \cdot \mathrm{sec}^{-1}$. Due to the low number of data events in the final event sample the 5σ discovery values are partly superimposed by the 90 % upper limits for all the neutrino candidates. OSFFit needs a lot of ($\approx 3-4$) well identified galactic neutrino events to indicate a discovery in the 2007-2008 data which have not been found for any of the candidates.

Zusammenfassung

Im Rahmen der vorliegenden Arbeit wird die Entwicklung und Evaluierung des Rekonstruktionsalgorithmus *OSFFit* vorgestellt. Er dient zur Charakterisierung von hochenergetischen Myonneutrinospuren im ANTARES Experiment. Ein weiteres Ziel ist die Herkunftsbestimmung der Teilchen, aus der, bei hinreichender Signifikanz, Rückschlüsse über ihre Beschleuniger sowie ihrer Beschleunigungsmechanismen abgeleitet werden können. Mit OSFFit wurden ferner hochenergetische γ-Quellen in der südlichen Hemisphäre hinsichtlich Neutrinoemissionen erforscht. Alle vorgestellten Berechnungen wurden innerhalb der offiziellen ANTARES Analyse-Software SeaTray durchgeführt, in welche OSFFit seit release 13-05-00 implementiert ist. Die verwendeten Daten beziehen sich auf die Jahre 2007 und 2008; als zugehörige Monte-Carlo-Simulationen wurden in der Regel RBR v 2.0 und RBR v 2.2 verwendet.

ANTARES ist ein Tiefsee Neutrinoteleskop, das sich vor der französischen Mittelmeerküste von Toulon in einer Wassertiefe von etwa 2500 m bis 2000 m befindet. Der Systemaufbau besitzt einen hexagonalen Grundriss und besteht aus zwölf Detektionseinheiten, die als Lines bezeichnet werden. Hierbei handelt es sich um ungefähr 450 m lange Taue, die am Meeresgrund verankert sind und durch den Auftrieb von oben angebrachten Bojen eine nahezu vertikale Ausrichtung annehmen. Zur Detektion von Tscherenkowstrahlung sind die Lines mit insgesamt 885 Photomultipliern bestückt. Tscherenkowlicht wird von Teilchen ausgesendet, die sich schneller als die Lichtgeschwindigkeit in dem jeweiligen Medium bewegen. Für das ANTARES Experiment sind speziell relativistische Myonen von Interesse, welche als Sekundärteilchen aus der Reaktion zwischen einem Neutrino und einem Atomkern hervorgehen können [10].

Das Myonneutrino stellt neben dem Elektronneutrino und dem Tauneutrino einen von drei Neutrinozuständen dar [11]. In dieser Arbeit stehen Myonneutrinos kosmischer Herkunft im Mittelpunkt. Um Myonsignale mit zufriedenstellender Qualitt zu erhalten, ist eine zuverlässige Ausgrenzung von Störgrößen unerlässlich. Als Beispiel einer möglichen Störgröße ist die emittierte Strahlung biolumineszierender Mikroorganismen zu nennen, die sich durch einen plötzlichen Anstieg der Lichtausbeute in den Photomultipliern über Stunden bis hin zu Tagen bemerkbar machen. So fern dies erkannt wird, ist betroffenes Datenmaterial für die weitere Ergebnisauswertung aus der Analyse auszuschließen. Als weitere Störquelle sind atmosphärische Myonen zu nennen.

Trotz deren ausgeprägter Abschwächung durch die in etwa 2000 m dicke Wasserschicht zwischen Meeresoberfläche und Detektor ist es erforderlich, zugehörige Ereignisse über die Rekonstruktionskette zu identifizieren und herauszufiltern. Ferner stellen atmosphärische Neutrinos einen Störeinfluss dar. Aufgrund ihres sehr kleinen Wirkungsquerschnittes (siehe Abbildung 2.7) und der damit verbundenen beachtlichen mittleren freien Weglänge [12] stellen sie eine erhebliche Herausforderung für die Untergrundunterdrückung dar [13]. Bis zu einer Energie von 100 TeV können Neutrinos die Erde ungehindert durchdringen. Atmosphärische Neutrinos lassen sich von kosmischen Neutrinos durch ihr flacheres Spektrum, und damit durch ihren niedrigen Energiebetrag, unterscheiden. In Punktquellensuchen dient außerdem die rekonstruierten Richtung der Teilchen als ein weiteres Filterkriterium. Die genannten atmosphärischen Myonen treten bei vertikalem Einfall um etwa sechs Größenordnungen häufiger auf als atmosphärische Neutrinos.

Mit der Zielsetzung die Spur von Sekundärmyonen zu charakterisieren, wird innerhalb der entwickelten Suchsequenz OSFFit eine stetige, analytische Beschreibung der Wahrscheinlichkeitsdichtefunktion der Zeitverteilung der eintreffenden Photonen verwendet (PDF). Die analytische PDF, genannt Sea-PDF, wurde für das geplante Neutrinoteleskop KM3NeT entwickelt [14]. Sie wurde im Rahmen dieser Arbeit an die ANTARES Geometrie angepasst. Das instrumentierte Volumen von KM3NeT ($\mathbb{O}(1\,\mathrm{km}^3)$) wird ANTARES um grob ein Fünzigfaches übertreffen. Interne Funktionen der Sea-PDF sind nach physikalischen Annahmen der Photonenpropagation aufgestellt. Sie beschreiben die Ankunftszeitverteilung der Tscherenkowphotonen in den Photomultipliern (PMTs). Zudem ist für die genannte PDF eine Schätzung der initialen Neutrinoenergie von nöten. Mit deren Hilfe wird der Energieverlust der Teilchen durch Ionisation, Paarproduktion und Bremsstrahlung berücksichtigt und gewichtet. Für die Energieschätzung bewährte sich das Programm *ANNergy* [15]. Gegenüber den konventionellen Methoden stellt dieser Ansatz eine Neuerung dar. Konventionelle PDFs werden in der Regel mit Hilfe von Monte-Carlo Informationen, zum Beispiel Monte-Carlo-Tabellen, generiert, welche die Ankunftshäufigkeit von simulierten Photonen in den PMTs beinhalten. Diese stammen wiederum von simulierten Myonpfaden. Diese PDFs können ferner mit der generierten Trefferamplitude (Ladung der Photoelektronen) oder geometrischen Überlegungen verknüpft sein. In diesem Sinne hängen derartige PDFs vollkommen von der Fehlerfreiheit der zugehörigen Monte-Carlo-Simulationen ab. Ein Mangel der aktuellen Monte Carlo Version ist beispielsweise das Fehlen einer Simulation für die Photonenstreuung in hochenergetischen Schauerereignissen, bzw. deren Vereinfachung durch die *One-Particle Approximation*. Durch die in OSFFit gewählte, unabhängige Herangehensweise kann die vorliegende Arbeit zudem als eine ergänzende Studie zu den bereits durchgeführten Neutrinosuchen für den Zeitraum 2007-2008 betrachtet werden. Dabei wurde die Qualität der rekonstruierten Myonspur als eine erste Näherung durch die Größe ihres Winkelunterschieds zur Monte-Carlo-Spur klassifiziert.

In dieser Arbeit werden die ersten Ideen zur Aufstellung von OSFFit bis hin zu dessen Umsetzung aufgezeigt. Der erste essentielle Schritt besteht darin, eine hinreichende erste Schätzung für die Lage der Myontrajektorie zu finden, auf welcher weitere Verfeinerungen basieren. Unter mehreren bekannten ersten Fitstufen, so genannten Pre-Fits, etablierten sich vor allem die Algorithmen *FilteringFit* und *BBFit* [16, 5]. Nach einigen Testreihen zeigt sich, dass BBFit für den hier dargestellten Fitalgorithmus als passend erachtet werden kann. Dagegen benötigt FilteringFit eine immense Rechenzeit und schließlich gefundene Myonpfade weichen zu sehr von der initialen, durch Monte Carlo Simulation vorgegebenen, Myontrajektorie.
Ausgehend von dieser ersten Spurannahme wurden Maximum-Likelihood-Berechnungen durchgeführt. Diese bestehen aus einem Minimieralgorithmus, der in einem n-dimensionalen Raum nach dem globalen Minimum sucht. Da in den vorliegenden Szenarien die drei Raumkoordinaten und die zwei Winkel des Teilchenweges bekannt sind, beschränkt sich das aufgespannte Volumen auf fünf Dimensionen. Die Wahrscheinlichkeit oder 'Likelihood', die einer Spurannahme zugeteilt ist, ergibt sich aus der Summation der logarithmischen PDF-Verteilungen eines jeden Photomultipliers. Eine Aufgabe einer Rekonstruktionsstrategie ist daher das Erstellen eines möglichst reinen Treffer Samples. Eine Spurannahme sowie ein Fit entsprechen jeweils genau einem Punkt in dieser Landschaft. Je nach dem vorliegenden Problem stellt sich für eine Likelihood–Landschaft, die große Unregelmäßigkeiten aufweist, ein Minimieralgorithmus mit großer Schrittweise als geeignet heraus. Für Probleme mit mehreren lokalen Minima, welche damit die Gefahr einer irrtümlichen Konvergenz beherbergen, scheint ein Algorithmus geeigneter, der nach dem Metropolis Kriterium auch zu gewissen Sprüngen im Likelihood-Raum fähig ist. Für OSFFit bewährte sich ein Minimierungsverfahren mit abwechselnd großen Schrittweiten.
Neben zu justierender Schrittweite und Grenzen der Minimierung ist die Wahl des Startpunktes variierbar. Unter Berücksichtigung all dieser Größen wurde ein abgestimmtes Verfahren herausgearbeitet. Neben dem Einbeziehen einer analytischen PDF bezieht OSFFit die Variation der ursprünglchen BBFit-Annahme mit ein und damit der Abdeckung eines möglichst großen Bereiches im zulässigen Phasenraum. In Form eines Zylinders mit dem Radius 5 m werden sechs Pfadannahmen äquidistant um den BBFit Track justiert. Der Startpunkt von 16 weiteren Annahmen entspricht dem BBFit-Vertex; diese Kopien werden – ebenfalls in gleichen Abständen – jeweils um 3° um die BBFitspur ausgelenkt. Die 22 Kopien sowie die BBFitspur selbst dienen als Pre-Fits für drei ausgewählte Maximum-Likelihoodfits. Um schließlich die geeignetste Spurannahme zu erhalten, werden die insgesamt 23 resultierenden Fitergebnisse einem Selektionverfahren und einem Schnittprozess unterzogen. Dieser Schnittprozess beinhaltet vielfältige Schnittwerte. Dazu gehören die internen χ^2-Abschätzungen von BBFit welche u.a. die Trefferamplituden berücksichtigen, sowie die Likelihoodwerte der analytischen und der finalen PDF. Des Weiteren sind die Anzahl an Photonentreffern, die rekonstruierte Einfallsrichtung des Myons und Werte, welche die beiden Likelihoods in effektiver Weise miteinander verbinden, enthalten. Bei Betrachtung der erreichbaren

Winkelauflösungen und Ereignismengen von Neutrinos stellt sich OSFFit als vergleichbar gut zu der bis dato bewährten Strategie *AAFit* heraus.
Für die Auswertung wurden die genannten Qualitätsschnitte von OSFFit so festgesetzt, dass die Menge der fehlrekonstruierten atmosphärischen Myonen eines 20.7 Tage Testsamples derjenigen von AAFit in diesem Zeitraum entspricht (1 atmosphärisches Myon). Diese Einschränkung reduziert auch die rekonstruierte (kosmische) Neutrinomenge deutlich. So wurde der Prozentsatz im Bezug auf das getriggerte, reine Neutrino-Referenzsample bei AAFit zu 23% mit einem Winkelfehler von 0.34° und im Falle von OSFFit zu 12% mit einem Winkelfehler von 0.29° errechnet.
Anhand eines größeren Datensamples wurden ferner Ereignissignaturen untersucht, für die sich OSFFit als sensitiver als AAFit erweist. Dabei stellen sich im Vergleich von rekonstruierten Myonannahmen, welche die Schnittkriterien beider Rekonstruktionen erfüllen, Unterschiede in deren Rekonstruktionsqualität heraus. Dieses Verhalten ist mit der Sensitivität der beiden Algorithmen bezüglich diverser Eventklassen begründet. OSFFit findet mehr Neutrinoereignisse, für deren Monte-Carlo-Simulation weniger als vier Lines verwendet wurden und solche, mit weniger als insgesamt 50 beteiligten Photonentreffern, mit einem Winkelfehler von unter 1° als AAFit. Ferner zeigt sich in der Verteilung der Zenitwinkelfehler, dass bei gleicher erfasster Datenmenge, OSFFit für horizontale Neutrinorichtungen und AAFit für direkt nach oben laufende Myonen geringfügig empfindlicher ist. Wegen der Unterschiede, die 1-2% betragen, erschien die Anwendung von OSFFit auf die Datenmenge, welche von AAFit ausgemustert wurde oder erst gar nicht rekonstruiert werden konnte, mit dem Ziel ebendiese Ereignisse in die AAFit Rekonstruktion einzubinden, als sinnvoll. Letztendlich erbrachte dies für AAFit mit einem Schnittparameter $\Lambda_{\mathrm{AAFit}} = -5.2$ eine Erhöhung der verwendeten Datenmenge von 62 % auf 64 % − 67 %, wobei der mittlere Winkelfehler nahezu konstant blieb (0.30°).

Schließlich wurde versucht mit OSFFit eine potentielle Neutrinoemission von 24 hochenergetischen γ-Quellen aufzuspüren. Die Detektion von Neutrinos aus diesen kosmischen Teilchenerzeugern könnte neue Erkenntnisse zu Beschleunigungsmechanismen von ausgehenden Leptonen und Hadronen liefern. So wurde innerhalb eines 20° Konus um eine hypothetische Neutrinoquelle nach einem statistischen Überschuss kosmischer Neutrinos gesucht; der Hintergrund bestand hauptsächlich aus atmosphärischen Neutrinosignalen. Der verwendete Neutrino-Referenzfluss bezüglich eines E^{-2}-Spektrums betrug $1 \cdot 10^{-7}\,\mathrm{GeV} \cdot \mathrm{cm}^{-2} \cdot \mathrm{sec}^{-1}$. Eine quantitative Trennung zwischen der 'Signal mit zusätzlichen Hintergrund'- und der 'nur Hintergrund'-Hypothese wurde mit einem Maximum-Likelihood-Verhältniss der beiden Kenngrößen ermittelt. In der Auswertung dieser Verhältnisse erwies sich die reine Hintergrundannahme für jeden der 24 Quellkandidaten als am wahrscheinlichsten. Ferner wurden die zugehörigen Ausschlussgrenzen für den möglichen Neutrinofluss bestimmt. Diese Grenzen wurden so berechnet, dass höhere Neutrinoflüsse mit einer 90 prozentigen Wahrscheinlichkeit zurückgewiesen werden konnten. Der kleinste Wert ergab sich für den Sterncluster HESS J1614-518 [9] zu

$\Phi^{\mathrm{up}}_{90\,\%} = 1.103 \cdot 10^{-7}\mathrm{GeV}^{-1} \cdot \mathrm{cm}^{-2} \cdot \mathrm{sec}^{-1}$. Die Datengrundlage für die ausgewählten Kandidaten beinhaltete nach Filterkriterien nur sehr wenige Ereignisse. Als eine Folge nehmen die berechneten Grenzen teilweise Werte an, die über dem jeweiligen 5σ Entdeckungspotential liegen. Für eine Entdeckung benötigt OSFFit sehr viele, etwa 3-4, sehr gut rekonstruierte galaktische Neutrinos im 2007/2008 Datensample. Tatsächlich konnten für die Quellen aber nur ungenügend gut rekonstruierte Ereignisse ausgemacht werden. Hinsichtlich bereits existierender Grenzen für das ANTARES Teleskop stellen die in dieser Arbeit errechneten Werte keine sensitiveren Ergebnisse dar. Dennoch repräsentieren sie die bislang ersten Grenzen die mithilfe von analytischen Ansätzen erzielt werden konnten.

Um die vorgestellte Studie abzuschließen soll letztendlich festgehalten werden, dass die größte Herausforderung für OSFFit, wie für alle Rekonstruktionsstrategieen, in der Untergrundunterdrückung liegt. Die verwendeten Likelihoodfits sind vielversprechend; mit einer weiter verfeinerten zugehörigen Hitselektion könnten mis-rekonstruierte Ereignisse besser erkannt und die Analyse verbessert werden, sodass eine insgesamt präzisere Auflösung sowie ein reineres Neutrinosample gewonnen werden könnten. Die verwendeten Likelihoodfits sind vielversprechend; mit einer weiter verfeinerten zugehörigen Hitselektion könnten mis-rekonstruierte Ereignisse besser erkannt werden. Die Analyse könnte mit einem reineren Neutrinosample aussagekräftigere Ergebnisse liefern.

Contents

Introduction

Humans have been exploring our universe for thousands of years – in the past by eye, nowadays by using sophisticated techniques. In contrast to most other scientific disciplines, the investigation of astrophysical objects and processes is mainly performed by the detected electromagnetic spectrum or by measuring primary or secondary cosmic rays. Victor Hess discovered cosmic ray particles only about 100 years ago in 1912 [17].

Today, further science fields have been established to gain more insight into our universe such as, gravitational wave astronomy and neutrino astronomy. The existence of the elementary neutrino particle was first postulated by Wolfgang Pauli in 1930. He explained the energy, momentum and angular momentum conservation violations of the so-far two-body problem of the β-decay, known as an emitted electron and its residual atomic nucleus, with a third particle that carries residual quantities. The neutrino's existence was experimentally verified in 1956 through a nuclear reactor experiment performed under the leadership of Clyde L. Cowan Jr. and Frederick Reines. In the late 1960s, Ray Davis's Homestake-Experiment gave rise to a further mystery around the new particle. The 'solar neutrino problem' is described as a deficit in the neutrino flux and is referred to comparison of data with predictions from the standard solar model [18]. The Sudbury Neutrino Observatory (SNO), observing neutrino interactions in a tank of heavy water, solved this question in 2001. The results are interpreted as neutrino oscillations that force the neutrino to change its flavour on its way between the source and the observer. Additionally, this flavour change makes a non-vanishing mass of the neutrino inevitable [11].

One motivation behind the relatively new field of neutrino astronomy is the question pertaining to acceleration processes and the origin of high-energy cosmic rays that have been measured on Earth. Active galactic nuclei, supernovas, pulsars and γ-ray bursts are suggested, among other astrophysical objects, to be (high-energy) cosmic ray emitters. Cosmic rays consist mainly of protons ($\approx$ 85%), α-particles ($\approx$ 12%) and a few heavier nuclei (atomic number $Z > 3$). These particles can be deflected by magnetic fields and matter; therefore, they cannot or, at highest energies, only carefully be used to backtrack to their origin. γ-rays and neutrinos are electrically neutral, which allows them to penetrate magnetic fields undeflected. γ-rays with energies above 100 TeV that originate from beyond the 'Local Group' undergo at least one absorption

processes involving matter or the extragalactic background light and do not reach us from afar. In contrast to γ-rays, the small cross-section of neutrinos allows the particles to pass through even dense media over long distances. Therefore, neutrinos can even provide information about the inner core of extragalactic sources and directly point back to their origins. This forges the neutrino into a suitable messenger particle [17]. Furthermore, the detection of a neutrino from a cosmic ray source would prove the hadronic character of its acceleration instead of the leptonic scenario [19].

For this reason, several neutrino reconstruction strategies exist for calculating the direction of the neutrino. If a high-energy muon neutrino interacts with an atomic nucleus over the charged current interaction it creates a relativistic muon, that sends out Cherenkov light on its trajectory. The emitted photons have a characteristic angle to the initial muon path: the Cherenkov angle. Usually, the neutrino reconstruction algorithms applied in the ANTARES experiment, are based on the Cherenkov light that is gained from Monte Carlo tables. This thesis presents the development of the strategy OSFFit that also takes advantage of analytical descriptions that are based on physical considerations about the behaviour of Cherenkov photons. The composition of OSFFit will be described in detail and illustrated by several performance plots. Apart from that, this thesis focusses on the discovery of neutrino point sources with OSFFit. Significant signals from 24 potential neutrino sources were searched from the data that the ANTARES detector had taken in 2007 and 2008. As no evidence for a neutrino source could be found with a certainty of 3σ, limits on the expected neutrino flux have been calculated.

This thesis is organised as follows: Chapter 1 provides an overview of the physics behind cosmic rays and introduces the large field of neutrino astronomy, including possible neutrino sources and acceleration sites. Chapter 2 concentrates on neutrino detection principles and possible background sources. Chapter 3 presents the ANTARES setup and its event triggers. Chapter 4 introduces all components for a neutrino reconstruction method and the first test samples, while Chapter 5 describes the full methodology of its creation and optimisation. Chapter 6 reports on the resulting performance and comparisons, as well as on possible complement characteristics to other reconstruction chains. Run and event selection, as well as performance studies of the full 2007/2008 data sample, are finally discussed in Chapters 7 and 8. The topic of Chapter 9 is a point source search. Pseudo experiments have been set up to look for an excess of events. As no source could be validated, quantities such as model discovery potential and limits have been calculated. Final results of the search are presented in Chapter 10. Summary and outlook are eventually the subjects of Chapter 11.

Part I

Basics

Chapter 1

Origin of high-energy cosmic neutrinos

Many years after the discovery of the neutrino it was found that this particle changes its weak eigenstate, which is also called 'flavour', along its trajectory. Since the discovery of neutrino oscillations, huge detectors have been built to find neutrinos that reach us from far beyond our sun. High-energy cosmic neutrinos may help us to solve the question of the powerful accelerators and the mechanisms for speeding up particles to energies far beyond what we can achieve in our labors. In the following chapter the Cosmic Ray (CR) spectrum, possible scenarios for high-energy acceleration sites, as well as the acceleration process itself, will be examined. Energies reaching from 1 TeV to 1 PeV will be abbreviated as VHE (very high energy), ultra-high energies $\geqq$1 PeV as UHE and extremely high energies $\geqq$100 EeV as EHE [20].

1.1 Cosmic Ray spectrum

Since the discovery of CRs, the CR spectrum has been explored within a broad energy range. Measurements have been performed e.g. directly with the help of balloons or cloud chambers and indirectly by detecting air showers that are generated by the interaction of a proton or atomic nucleus with a nucleus in the Earth's atmosphere. The Pierre Auger Observatory (PAO), the High Resolution Fly's Eye Cosmic Ray Detector (HiRes), the Akeno Giant Air Shower Array (AGASA) and others have identified these showers [21] as consisting of diverse particles such as electrons, photons, muons or pions. Figure 1.1 shows the corresponding differential cosmic particle flux $d\Phi/dE$ multiplied with energy over the energy E of the particles. It exhibits a non-thermal, broken power law shape, which points to several energy cut-offs in the cosmic components and can be mathematically expressed as shown in Equation 1.1 [20]. The constant factor Φ_0 stands for the flux normalisation and γ for the spectral index.

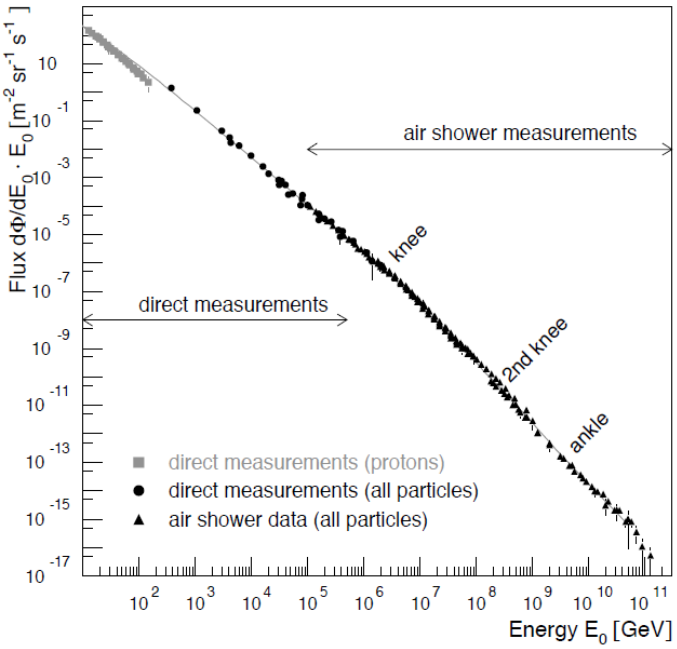

Figure 1.1: Differential cosmic ray spectrum $d\Phi/dE$ over the particles' energies E. The picture is taken from [22].

$$\Phi = \frac{dN}{dE} = \Phi_0 \cdot E^{-\gamma},$$

$$\text{with } \gamma \approx \begin{cases} 2.7 & \text{below the knee, for} \quad E \leqq 3 \cdot 10^{15}\,\text{eV} \\ 3.1 & \text{at the knee, for} \quad 10^{15}\,\text{eV} \leqq E \leqq 10^{16}\,\text{eV} \\ 2.7 & \text{above the ankle, for} \quad E \geqq 10^{19}\,\text{eV} \end{cases} \tag{1.1}$$

The propagation and confinement of CRs by the galactic magnetic field can be described using the so-called 'leaky box' model. The gyromagnetic radius or Larmor radius for a particle with energy E and charge Z in a magnetic field B is given by $R_{\text{gm}} = E/eZB$ [23, 24]. Particles with gyromagnetic radii that do not exceed the size of the galaxy remain confined. Therefore, CRs up to these energies are thought to have a galactic origin, while at higher energies they can escape. CRs with energies up to the start of the knee at $10^{15}\,\text{eV}$ are supposed to be accelerated by diffusive shock acceleration taking place in galactic supernova remnants [24], as described by the Fermi mechanism [25]. This mechanism will be described in Chapter 1.3. The region around the knee represents the maximum energy that can be achieved by cosmic accelerators. Protons with energies from $10^{15}\,\text{eV} \leqq E \leqq 10^{16}\,\text{eV}$ start to leave the Milky Way. Heavier nuclei have larger charges and, therefore, must be accelerated to larger energies to achieve the same gyromagnetic radii as protons. The heavier element cut-off lies at higher energies. Consequently, the composition of CRs for energies above the knee shows a domination of heavier nuclei over the protons. Due to the different cut-off values the spectral index changes from $\gamma \approx 2.7$ to $\gamma \approx 3.1$. Most probably the second knee at roughly

$4 \cdot 10^{17}$ eV indicates the end of the stable elements of the galactic component and the beginning of an extragalactic component [26, 27]. The flattening of the spectrum at the ankle at roughly 10^{19} eV is also explained by the takeover of a harder extragalactic component. In this range known galactic source candidates are running out of power, and even if not, accelerated particles would escape the galaxy since their gyroradius exceeds the size of the galaxy [28]. Further on it is expected that the GZK cut-off, which is known as inelastic interaction between microwave background photons and CR protons, strongly attenuates the spectrum of CRs around $E \approx 5 \cdot 10^{19}$ eV [23]. Measurements performed by PAO, HiRes and the Telescope Array (TA) are consistent with the existence of such a break in the cosmic ray spectrum with more than a $5\,\sigma$ certainty [29, 30, 31], but inconsistent in the correct interpretation of its origin [32]. The GZK cut-off limits possible emitters of ultra-high energy cosmic rays (UHECRs) to inside our local cluster of galaxies.

1.2 Neutrino production

One production scenario of high-energy neutrinos arises from the interaction of a fraction of the accelerated protons with nuclei or photons in or around the source [18]. Therefore, the neutrino spectrum resembles the one of their primaries. The resulting particle cascades are dominated by neutral and charged kaons and pions (see Equation 1.2). As Equation 1.3 reveals, the neutral mesons will decay into photons and the charged mesons into neutrinos [18]. N stands for any atomic nucleus and X_{had} for a system of outgoing hadrons.

$$\left.\begin{array}{l} \mathrm{p} + \gamma \\ \mathrm{p} + \mathrm{N} \end{array}\right\} \quad \pi^+, \pi^-, \pi^0, K^+, K^-, X_{\mathrm{had}}. \tag{1.2}$$

$$\begin{array}{rcll} \pi^0 & \rightarrow & 2\gamma & \\ \pi^+, K^+ & \rightarrow & \nu_\mu + & \mu^+ \\ & & & \mu^+ \rightarrow \overline{\nu}_\mu + \nu_e + e^+ \\ \pi^-, K^- & \rightarrow & \overline{\nu}_\mu + & \mu^- \\ & & & \mu^- \rightarrow \nu_\mu + \overline{\nu}_e + e^- \end{array} \tag{1.3}$$

As can be gathered from Equation 1.3, neutrino flavours should occur in the ratio $\nu_e : \nu_\mu : \nu_\tau = 1 : 2 : 0$, which would change during their long path to Earth into $1 : 1 : 1$ [17]. For a short overview of neutrino oscillations see [11].

1.3 Cosmic ray acceleration

Besides the question of the origin of CRs, it is also unclear how those particles reach their high energies. Solar flares may explain acceleration up to the GeV range, but not higher [19]. Diverse hadronic and leptonic models should be capable of reaching higher energies (see next section). Both models include shock acceleration or *first-order Fermi acceleration*. The scenario describes the acceleration of the initial particle through elastic scattering effects on magnetic inhomogenities which typically precede and follow shock waves. These waves arise in astrophysical environments that are subjects of extreme conditions, such as in explosions, in very strong electrical discharges and in other cases. Iterative reflections on one or even more shock fronts successively provide the particle with an energy gain until it escapes the acceleration region. The energy spectrum of particles undergoing this process theoretically results in an E^{-2} dependency [17, 33, 34]. CRs are affected by several attenuation effects before reaching Earth. They can be absorbed by molecular dust or the interstellar media and deflected by magnetic clouds. Therefore, on Earth an $E^{-2.7}$ dependency is assumed and has actually been measured, as Figure 1.1 and Equation 1.1 illustrate. The acceleration sites that most likely make use of the Fermi mechanism are listed in Chapter 1.4.

In leptonic processes accelerated electrons create photons up to at maximum the TeV range through synchrotron radiation and inverse Compton scattering. In hadronic scenarios, as described by Equation 1.2, hadrons might be provided with energies even up to the EeV range. Thus, the detection of neutrinos (or even PeV γ-rays, see Equation 1.2) on Earth would be obvious proof of a hadronic character of the acceleration model. Fermi acceleration is the most probable and simplest model for plasma and magnetic acceleration today.

1.4 Candidate cosmic ray accelerators

A few astrophysical sources are believed to be responsible for the production and emission of high-energy cosmic neutrinos which have not been discovered yet. As mentioned above, the transition from galactic to extragalactic CRs should occur somewhere between $10^{15}\,\mathrm{eV}$ and $10^{18}\,\mathrm{eV}$ [35]. Section 1.4.1 will focus on source candidates within our galactic surroundings and Section 1.4.2 on potential sources of UHE or even EHE neutrinos. For all these candidates the Fermi mechanism might play a role.

1.4.1 Galactic candidates

The Imaging Air Cherenkov Telescopes (IACT) like the γ-ray telescopes H.E.S.S., MAGIC and VERITAS have discovered a lot of TeV γ-ray sources in our galactic surroundings. These sources are assigned to be supernova remnants, X-Ray binaries, pulsar wind nebulae or microquasars [36, 37].

A **supernova remnant (SNR)** is an expanding shell around a compact object, the collapsed core of a star, that has undergone a supernova explosion. It is assumed that within this structure protons are accelerated in shock fronts according to the Fermi mechanism, leading to an E^{-2} spectrum [25]. As already described in Chapter 1.1, particles accelerated to energies up to the TeV range are predicted [19].

A possible scenario after a supernova explosion is the transformation of the inner core into a pulsar. A pulsar is a highly magnetised rotating neutron star that emits relativistic winds on its poles. These may interact with the supernova envelopes and create a shell around the pulsar called a **pulsar wind nebula (PWN)**. The emitted material may create shock waves within the shell, whereby photons from radio waves up to TeV γ-rays are created, probably by electronic processes (via the Fermi mechanism). Detectable neutrino fluxes are expected to be $\mathbb{O}(1)$ per year for a $1\,\mathrm{km}^3$ neutrino detector [38, 39].

Microquasars (MQs) are **X-Ray binary systems (XRBs)**. They consist of a black hole or neutron star accreting and emitting horizontal and vertical material from an accompanying normal star. In two perpendicular emitted jets, shock fronts accelerate protons and electromagnetic radiation. In this way, significant fluxes of TeV γ-rays and TeV neutrinos emerge due to proton-proton, photo-meson and photo-disintegration processes. This may occur in the wind or the atmosphere of the normal star, as well as in the accretion disk or in the jet [40, 41, 42].

Fermi bubbles are two nearly elliptical structures extending $8 - 9\,\mathrm{kpc}$ out of the galactic centre on either side of the galactic disk. The Fermi LAT detector discovered these two γ-ray emitting bubble-shaped structures in 2010. Their origin is not quite clear [43]. The detection or exclusion of high-energy neutrinos or γ-rays could provide hints regarding hadronic or leptonic acceleration in those structures. A $1\,\mathrm{km}^3$-scale detector in the northern hemisphere, such as the planned KM3NeT neutrino telescope, is – inter alia – predestined to solve this question [44].

1.4.2 Extragalactic candidates

The origin of the highest-energy particles is assumed to be extragalactic. Often cited acceleration regions for UHECRs are γ-ray burst shocks, as well as jets and hot spots of active galactic nuclei and rotating neutron stars accompanied by strong electromagnetic fields. It is also imaginable that a whole cluster of SNRs may successively accelerate particles [20, 17, 35].

Active galactic nuclei (AGNs) are active cores of galaxies consisting of a rotating super-massive black hole, accreting material and emitting material in jets. Shock fronts in these jets are assumed to provide protons and electrons with energies partly even above 10^{20} eV. Hadronic and leptonic cascades arise. Protons can interact with synchrotron photons and matter via processes introduced in Equation 1.2, and release UHE neutrinos that can escape the object. Photons detected on Earth range from radio waves to TeV γ-rays. Subclasses of AGNs include, for instance, radio galaxies, blazars and quasars [20]. However, the GZK cut-off and the large cosmological distances of CRs from Earth (> 100 Mpc) present the major complication concerning a discovery.

Gamma-ray bursts (GRBs) are the brightest phenomena in the universe, emitting only during a period of seconds or tens of seconds. Like many sources introduced above, they may accelerate particles in their jets by internal shocks via the Fermi mechanism. The energy of the neutrinos produced might vary from TeV to EeV [20]. The origin of GRBs is not fully explained yet, but supernovas, hypernovas or the merging of a double-neutron star (NS-NS) or a neutron star-black hole binary (NS-BH) are discussed [45]. In studies performed by ANTARES and IceCube no evidence for a significant neutrino emission has been found so far [46, 47].

Chapter 2

Principles of neutrino detection

Muon track reconstruction is one of the main analysis techniques in the ANTARES experiment and the topic of this thesis. Besides muons events generated in the interaction of muon neutrinos with atomic nuclei, also events created in interactions of tau and electron neutrinos with atomic nuclei and also background events (atmospheric muons and ^{40}K events) may pass the triggering system. In this chapter, different neutrino and lepton signatures will be introduced.

2.1 Neutrino properties

Neutrinos are electrically neutral leptons and interact via the weak force. The nearly massless particles have relatively small interaction cross-sections (see Figure 2.7), which let them traverse compact objects. Up to an energy of 100 TeV, they can penetrate compact objects like the Earth without interactions. The Earth's diameter is $\approx 1.27 \cdot 10^4$ m. The ANTARES detector is built to be sensitive for neutrinos that traverse the Earth with energies above 10 GeV [48]. Beyond an energy of 100 TeV compact objects with similar diameter start to become opaque for neutrinos, up to 1 PeV neutrino energy. Neutrinos with that high energies have to be detected from above; then, the influence from the background is negligible small (see Chapter 2.4.3). Neutrinos can be detected in very large detection volumes if a hadronic or an electromagnetic interaction takes place within or near the detector [18].

2.2 Neutrino-nucleon interactions

There are three known neutrino flavours that undergo different reactions with nuclei or electrons. The relevant neutrino signatures are the deep inelastic charged current

reaction (CC) and the neutral current reaction (NC) [12]:

$$\begin{aligned} \nu + N &= l + X_{\text{had}} \quad \text{(CC reaction)}; \\ \nu + N &= \nu + X_{\text{had}} \quad \text{(NC reaction)}. \end{aligned}$$

N stands for any target nucleon, X_{had} for a system of outgoing hadrons, l for a lepton and ν for the corresponding neutrino. The lepton can be a muon, electron or tauon that appears as an outgoing particle in the CC process. As neutrino telescopes do not distinguish between lepton and anti-lepton nor between neutrino and anti-neutrino, the following particle names will refer to both kinds; particles and anti-particle names will not be mentioned again. The (pseudo-) Feynman diagrams used in Figures 2.1 to 2.4 illustrate the four deep inelastic interactions with the virtual exchange bosons $W^{\pm}$ and Z^0.

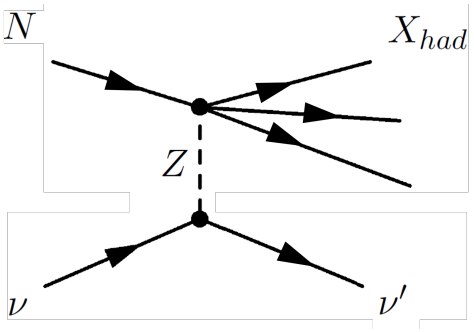

Figure 2.1: NC interaction. The neutrino keeps its flavour and shares its energy and momentum with a set of hadronic outgoing particles.

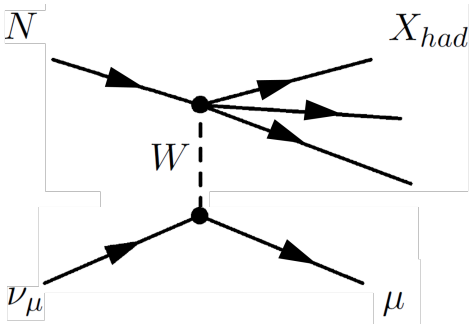

Figure 2.2: CC muon neutrino interaction. A muon and a hadronic shower are the products of the interaction.

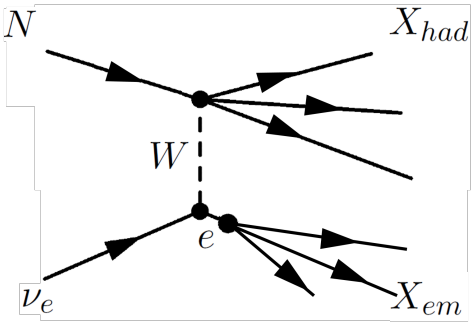

Figure 2.3: CC electron neutrino interaction. An electron and a hadronic shower leave the vertex. The electron immediately loses energy via bremsstrahlung and pair production and produces an electromagnetic shower.

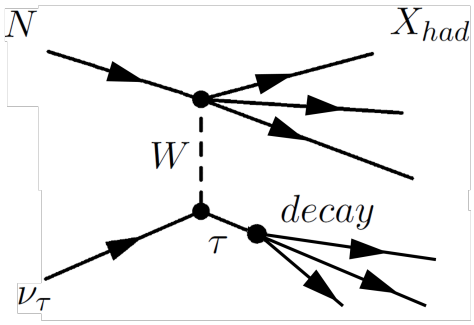

Figure 2.4: CC tau interaction. One branch ends up in a hadronic shower, while the other branch is described by a tau lepton with, once again, many decay possibilities (see Equation 2.3).

Muon neutrino CC process

Figure 2.2 illustrates the CC interaction process between a muon neutrino and a nucleon with a muon and a hadronic particle shower as its outcome. The energy of the incoming neutrino influences the direction of the outgoing muon (see Figure 2.6). Vice versa, from the arising muon track the neutrino direction can be inferred. The average angular separation between neutrino and muon $\Theta_{\nu-\mu}$ is 0.7° for neutrino energies of 1 TeV. It then decreases with increasing neutrino energy following Equation 2.1, which is plotted in Figure 2.5 [48, 12].

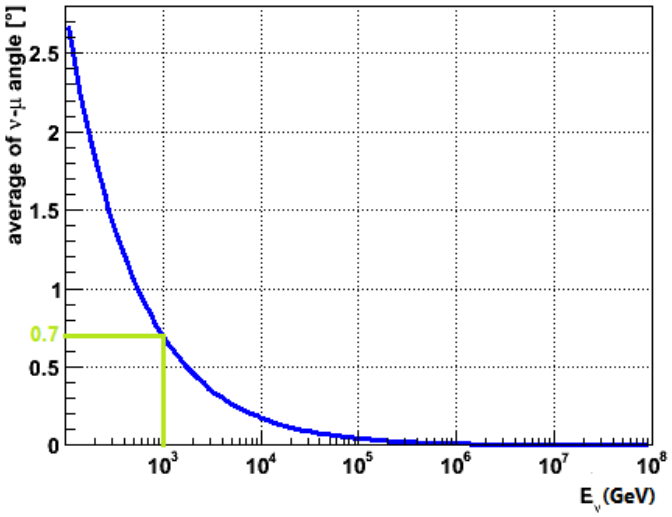

Figure 2.5: Average angular separation between neutrino and muon $\Theta_{\nu-\mu}$, following the equation below. It is 0.7° for neutrinos with 1 TeV and decreases with increasing neutrino energy (see green lines).

$$\Theta_{\nu-\mu} = \frac{0.7^\circ}{(E_\nu(\mathrm{TeV}))^{0.6}} \quad (2.1)$$

The muon loses energy on its way through the detector. Ionisation, bremsstrahlung, pair production and photo-nuclear interactions are dominant energy loss processes, which can be parameterised as shown below:

$$\frac{dE_\mu}{dx} = \gamma(E_\mu) + \beta(E_\mu) \cdot E_\mu, \quad (2.2)$$

where $\gamma(E_\mu)$ represents the energy loss by ionisation and $\beta(E_\mu)$ includes bremsstrahlung, pair production and photo-nuclear interactions. Figure 2.6 shows the mean path length of a muon, tauon and an electromagnetic and hadronic shower over the corresponding energy. It can be seen that a muon with 1 GeV initial energy may still travel a few metres before it decays. For a muon with an energy of 1 TeV, it can even be a few kilometres [24]. These long path lengths are due to the long lifetime of a muon ($\approx$ 2 µs) and its low interactions [49]. Electrons are not added to this diagram since they immediately shower through bremsstrahlung and pair production until the energy of the constituents falls below a critical value and the shower production stops. The sensitive volume of the ANTARES detector where muon paths are still detectable extends to roughly twice the light attenuation length in sea water, $\lambda_{\mathrm{att}} = 55$ m, around the instrumented detector volume [50]. This is depicted in Figure 2.8.

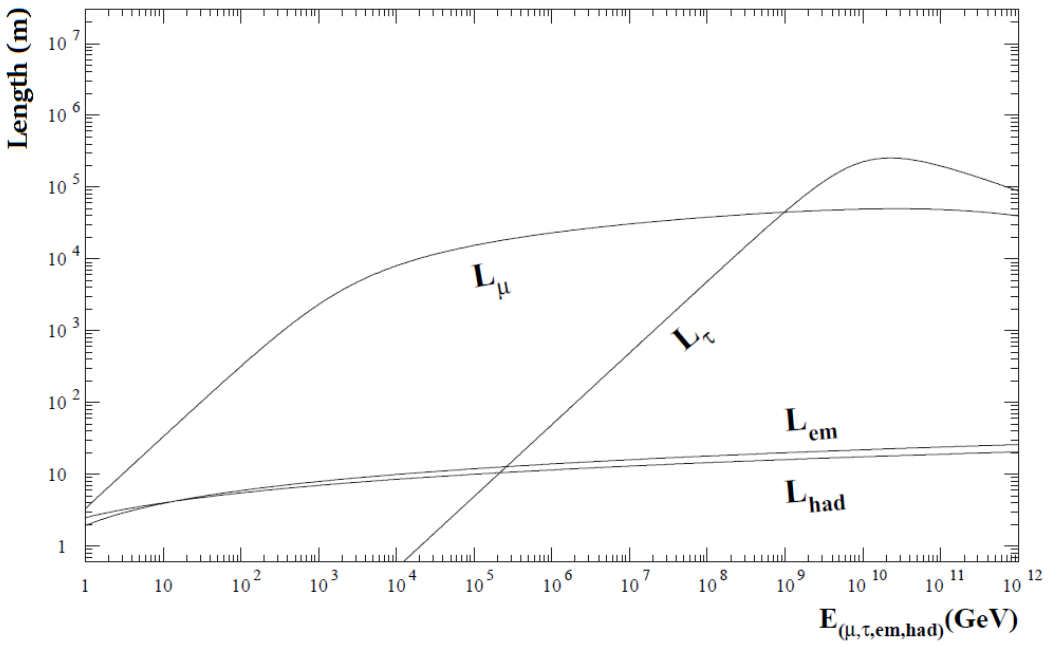

Figure 2.6: Mean path lengths of muons ($\mathbf{L}_\mu$) and tauons ($\mathbf{L}_\tau$) and of hadronic ($\mathbf{L_{had}}$) and electromagnetic cascades ($\mathbf{L_{em}}$). The plot is taken from [51].

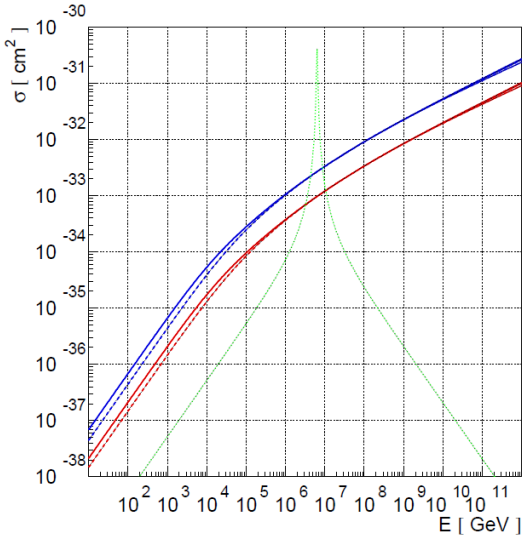

Figure 2.7: Cross-section of neutrinos (solid) and anti-neutrinos (dashed) for the CC and NC interaction in blue and red, respectively. The Glashow resonance is depicted in green. The plot is taken from [13].

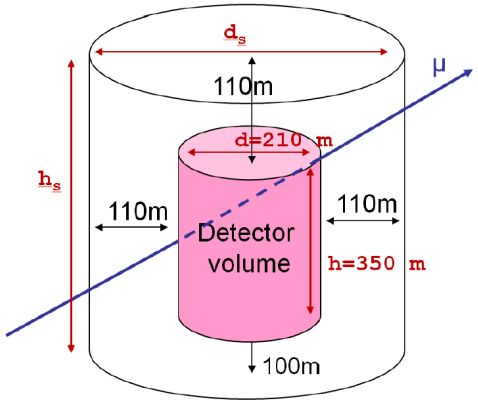

Figure 2.8: Definition of the sensitive cylinder volume. It is formed by a diameter $d_s = 430\,m$ around the detector centre and a total height $h_s = 560\,m$. The schematic is taken from [50].

Electron neutrino CC process

The initial CC interaction of the electron neutrino with an atomic nucleus ends up in a hadronic cascade and an electron that loses energy due to bremsstrahlung. After a few tens of centimeters path length of the electron, pair production and subsequent bremsstrahlung lead to an electromagnetic cascade. Muons and tauons with path lengths up to several kilometres may start far away from the detector and are still detectable. Contrary to this, showers have a broader lateral (in the order of a few tens of centimeters [24]) and a shorter longitudinal extension (up to 10 m) and thus, they have to take place near the instrumented detector volume, in a distance of a few tens of meters, to be detectable (see Figure 2.8). The electron-neutrino interaction channel can be used for diffuse flux measurements, flavour studies or energy measurements, but will not be focused on in this work [12]. Recently, a new shower reconstruction for inter alia galactic muon neutrinos has been established. It reaches a median angular resolution smaller than 3° [52, 53].

Tau neutrino CC process

The interaction of a tau neutrino with an atomic nucleus is associated with a double-bang signature (see Figure 2.4). The first bang is defined by a hadronic shower, while the second bang is caused by the short tauon lifetime ($\approx$ 0.29 ps [49]). In the energy range of interest, the tauon can travel a few meters up to kilometers [24]. Depending on the tau neutrino's energy, three relevant decay scenarios in the following branching ratio are possible [49]:

$$\begin{aligned} &(1) \quad \tau \rightarrow \nu + \overline{\nu} + \mu \quad (17.4\,\%) \\ &(2) \quad \tau \rightarrow \nu + \overline{\nu} + e \quad (17.9\,\%) \\ &(3) \quad \tau \rightarrow \nu + X_{\mathrm{had}} \quad (64.7\,\%) \end{aligned}$$

The second bang arises only for decays (2) or (3) if the tauon energy is above some TeV [12]. Cases (1) and (2) have already been described above, case (3) will be described in the next paragraph. As the tauon and its interactions are not main topics of this work, they will not longer be focused on.

NC processes

As Figure 2.1 demonstrates, the neutrino keeps its flavour (μ, e, τ) in NC interactions, but shares its momentum and energy with an outgoing hadronic cascade. The NC cross-section in Figure 2.7 is about one order of magnitude lower than the CC cross-section, thereby promoting the latter to the dominant process. The cross-section for interactions with electrons is negligible, with the exception of the Glashow resonance.

Glashow resonance
The Glashow resonance can be interpreted as the interaction between an anti-neutrino and an electron. There is a resonant production of the W^- boson at roughly 6.3 PeV neutrino energy. The decay of the W^- boson can result in all above mentioned event signatures [54]. Its cross-section is also shown in Figure 2.7.

2.3 Cherenkov light

A charged particle moving in an electrically polarizable medium such as water with velocities, higher than the speed of light in that medium, excites the molecules along its path. Only, if the charged particle moves faster than the speed of light in that medium, molecules are polarized to an overall dipole moment. When the electrons of the molecules restore themselves to equilibrium, the emitted photons interfere coherently and propagate on a conical shape with a fixed opening angle Θ_C around the particle path away from it (see Figure 2.9) [24]. The Cherenkov angle Θ_C is related to the initial particle velocity $\beta = v/c$ and the refractive index of the medium n via [48]:

$$\cos \Theta_C = \frac{1}{n \cdot \beta} \tag{2.3}$$

The detecting optical sensors of the ANTARES experiment are designed to have their highest efficiency between 400 nm and 500 nm, where the transparency of seawater is maximal and the average refractive index is $n = 1.35$. For the energies $E > 10$ GeV, leptons are highly relativistic ($\beta \approx 1$) and the Cherenkov angle is independent from the energy at a value of:

$$\Theta_C = 42.21^\circ \tag{2.4}$$

A highly relativistic lepton carying unit charge is expected to produce 100 photons in the wavelength bin between 400 nm and 500 nm in 1 cm flight path. On a shell in a perpendicular distance of 40 m around the particle path, there is still one photon per 340 cm^2. Absorption and scattering due to pollution of the water enlarge the distribution of arrival times of photons and can diminish the light yield with respect to the former case. In [48], measurements are described using LEDs to give short light pulses. They are located at distances of 24 m and 44 m in front of an optical module as is used for ANTARES. Still, 95% and 90% of the photons for the 24 m and 44 m LEDs, respectively, were collected within 10 ns. Attenuation effects due to the pollution of seawater turned out to be the main uncertainty at the ANTARES site.

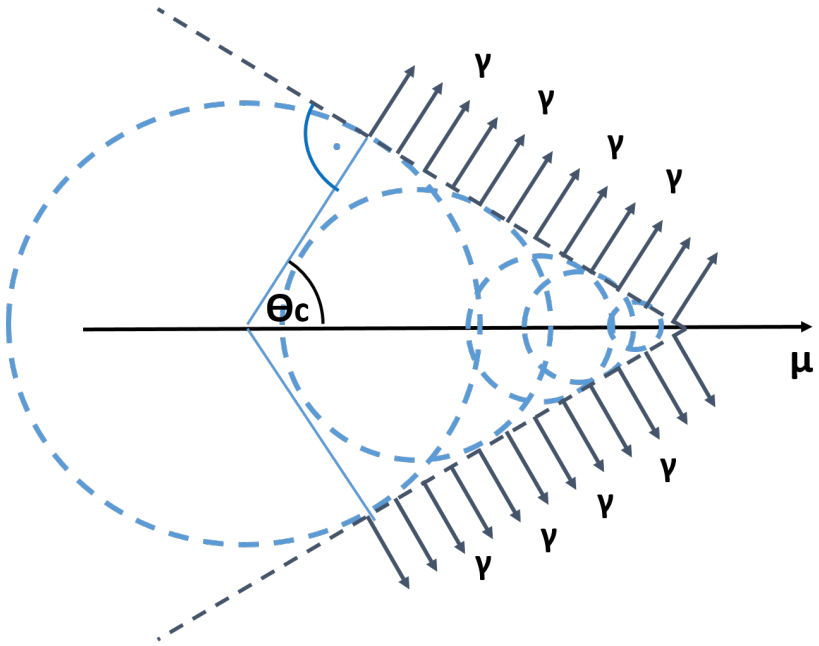

Figure 2.9: Cherenkov cone of a charged muon moving through a dielectric medium faster than the speed of light in that medium. It emits Cherenkov radiation γ under a characteristic angle Θ_C.

2.4 Background sources

Unavoidable background sources reduce the purity of the data. The origin of background sources splits into radioactive decay, bioluminescence and atmospheric particles. Chapter 3.2 describes how these background sources can be reduced.

2.4.1 Radioactive background

Radioactive background refers to mainly the decay of the isotope potassium-40 (^{40}K). Approximately 89% of ^{40}K nuclei decay into ^{40}Ca by β-decay and approximately 11% decay into an excited ^{40}Ar state. To fall back to ground state, this Ar ion emits a photon that, in turn, scatters by electrons through Compton scattering. In both scenarios, resulting electrons have enough energy (1 MeV up to 1.5 MeV) to produce Cherenkov light, which causes a noise rate of $\approx$ 30 kHz per detecting optical sensor (see Chapter 3) [55].

2.4.2 Bioluminescence

The environment of the ANTARES detector is populated by a few microscopic life forms, as well as by fish and algae, of which some send out light. The light pollution

correlate with the season, water velocity and the population size of life forms near the detector. Thus, the biological optical background rate range from 20 kHz to more than 1000 kHz in the form of *bursts* that usually last a few seconds.

Stable bioluminescence conditions together with ^{40}K hits and electronic dark noise in the optical sensors or photomultipliers (≈ 3 kHz) are denoted as the *baseline rate* (at ≈ 55 kHz). The baseline rate is plotted in Figure 2.10 for the runs (time intervalls of up to eight hours, see Chapter 3.2) taken in 2007 and 2008. The black dots correspond to all the runs taken within this period. They are overlaid by light-green dots that mark data analysed in this thesis. A few runs have been excluded; the reasons for this are described in Chapter 7. The burst fraction is illustrated in Figure 2.11 for the same dataset. Technically, it is defined as the fraction of the time in which the rate of the bursts exceed the baseline rate by at least 20% [56]. The mean rate representing the average of introduced rates is displayed in Figure 2.12 for the same data period. Run numbers starting at approximately 31000 are accompanied by constantly lower rates, which indicates less background pollution.

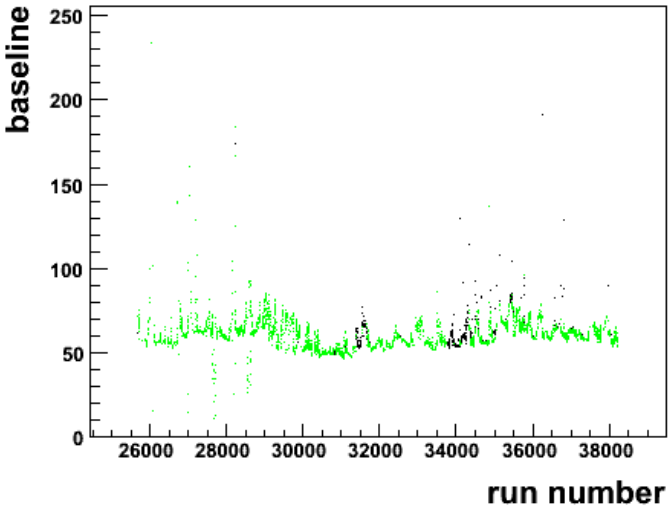

Figure 2.10: Baseline for run numbers 25682 to 38230. The black dots correspond to runs taken in 2007 and 2008, they are overlaid by light-green dots that mark runs analysed in this thesis.

2.4.3 Cosmic ray background

The interaction of cosmic rays with nuclei in the Earth's atmosphere gives rise to hadronic cascades that produce atmospheric muons and neutrinos analogous to the production of muons and neutrinos in astrophysical sources, as already introduced in Chapter 1.2 and Equations 1.2 and 1.3. The number of atmospheric muons exceeds those induced by atmospheric neutrinos by a factor of approximately 10^6 [48] (see Figure 2.14).

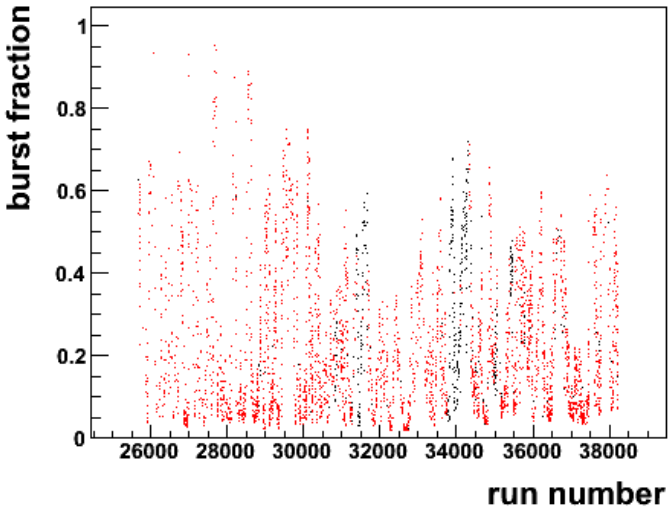

Figure 2.11: Burst fraction for run numbers 25682 to 38230. The black dots correspond to all runs taken, they are overlaid by red dots that mark runs analysed in this thesis.

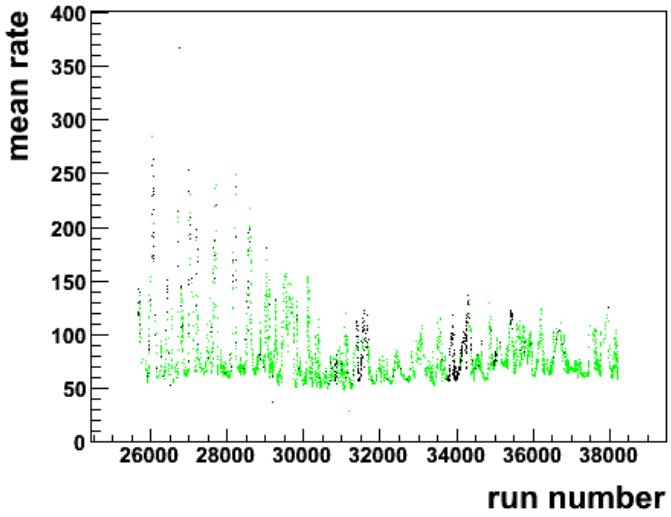

Figure 2.12: Mean rate for run numbers 25682 to 38230. The black dots correspond to all runs taken, they are overlaid by light-green dots that mark runs analysed in this thesis.

Atmospheric muons

The number of atmospheric muons that reach the detector from above is reduced by the huge amount of sea water above the detector. Their amount depends on the muon path length through sea water making the zenith angle an appropriate filter criterion. As can be seen in Figure 2.14, the muon flux decreases with a decreasing zenith angle and completely disappears at zenith angles θ smaller than $\cos\theta = 0.1$ ($\hat{=}\ 84°$, almost horizontal). Nevertheless, muons from air showers can occur in bundles (a few hundred in 2007–2008 data), which yield correlated hit patterns in the PMTs that can imitate an upward-going particle path. The detector design favours a further type of fake event. Figure 2.13 illustrates the scenario of the so-called *ghost solution*. Here, the interaction

vertex may lie outside the detector and one branch of the resulting Cherenkov light front hits at least one outward line accidentally in parallel. It is no longer possible to distinguish whether the initial particle was moving upwards or downwards. This phenomenon becomes noticeable in a typical reconstructed angular error of 84°, which is twice the Cherenkov angle Θ_C.
A cleverly devised reconstruction algorithm is needed to suppress mis-reconstructed tracks.

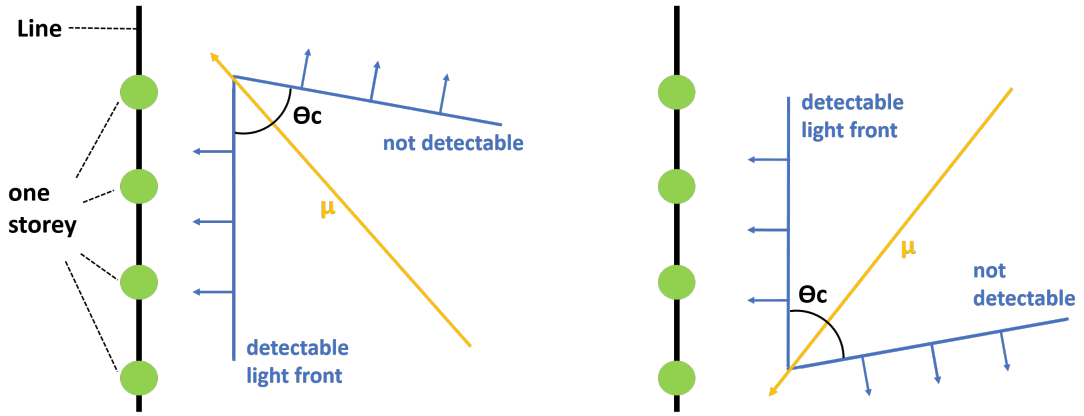

Figure 2.13: Illustration of the ghost solution. It describes the occurrence of a Cherenkov light front parallel to an outward detector line. It is not feasible to find out whether the initial particle was moving upwards or downwards. The mis-reconstruction mirrors a reconstructed angular error of 84°, which is twice the Cherenkov angle Θ_C.

Atmospheric neutrinos

Besides atmospheric muons, air showers also create atmospheric neutrinos. In contrast to atmospheric muons, Earth's shield and sea water above the detector are not effective enough to suppress the number of atmospheric neutrinos significantly. The small cross-section of neutrinos allow them to pass long distances, almost independently on the shielding material (see in Figure 2.14). In a search algorithm they are distinguishable from cosmic neutrinos ($\gamma \approx 2.0$) only by their softer energy spectrum or angular separation from the source. Thus, the pulse amplitude or even the amount of hit PMTs serve as effective distinguishing feature between cosmic and atmospheric neutrinos.
The atmospheric neutrino flux consists of a conventional and a prompt component. The conventional fraction, caused by the decay of pions and kaons, can be described by the Bartol flux model. Its prompt part results from the decay of charmed particles. Theoretically, it slightly flattens the conventional spectrum starting at approximately 10^5 GeV (see Figure 2.15). This behaviour has not yet been observed [57].

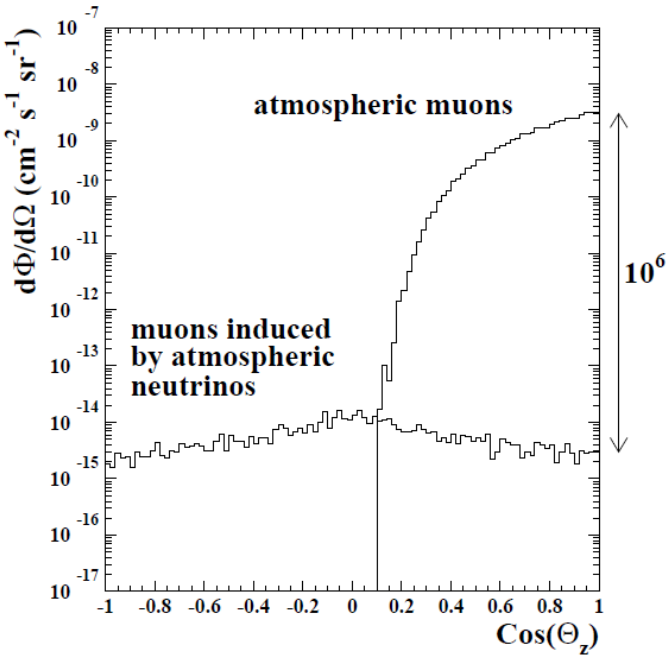

Figure 2.14: Zenith angle distribution of the muon flux above 1 TeV from atmospheric muons and atmospheric neutrino-induced muons at a 2300 m water-equivalent depth. The plot is taken from [48].

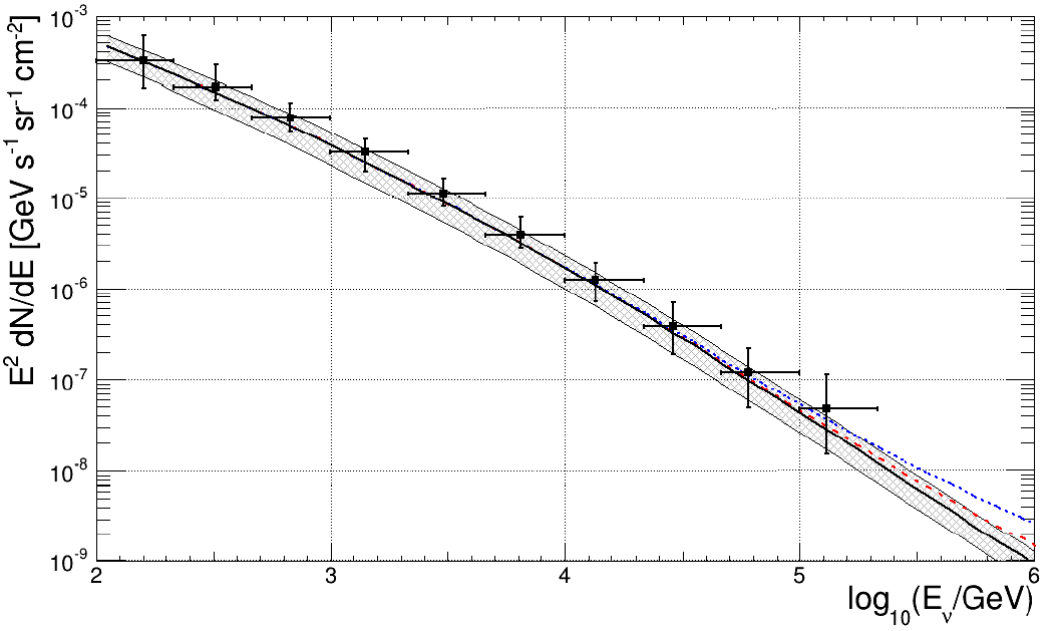

Figure 2.15: Atmospheric neutrino energy spectrum obtained with ANTARES using 2008-2011 data. The flux reported here is multiplied by E^2. The grey band corresponds to the uncertainty in the conventional (Bartol) flux calculation. Along with this conventional flux, calculated prompt fluxes are depicted in red-dashed ([58]) and blue-dashed (Enberg) lines. The plot is taken from [57].

Chapter 3

The ANTARES detector

3.1 Location and setup

The ANTARES neutrino telescope was completed in May 2008 as the first operational neutrino telescope in the Mediterranean Sea. The ANTARES collaboration consists of 29 universities from eight countries (France, Germany, Holland, Italy, Morocco, Romania, Russia and Spain) [59]. Other neutrino telescopes are IceCube at the South Pole and the Lake Baikal Neutrino Telescope in Russia [28]. The ANTARES detector is sensitive for cosmic neutrinos at energies above $E_\nu \approx 10\,\mathrm{GeV}$.

The ANTARES detector is located 40 km off the French coast from Toulon (42° 48′ N, 6° 10′ E). It is positioned at a depth of 2475 m. Figure 3.2 provides a schematic impression of the detector, which is based on the hexagonal footprint displayed in Figure 3.1. The red dots mark the positions of the twelve strings (ropes), which are separated by a distance of roughly 60 m. They extend 480 m in vertical length and are held tight by a buoy at the upper and an anchor at the lower end. One further string is equipped with instruments for detailed oceanographic and water properties measurements. There are 885 optical modules (OMs) distributed in 25 triplets (storeys) on each string, with the exception of string twelve where their amount is 20 storeys. The symmetrical arrangement of the string units, as well as the orientation and position of the OMs, have been optimised for muon neutrinos with energies higher than 100 GeV; thereby, Earth serves as shield against atmospheric particles. Each OM looks downwards at 45° (zenith) and is horizontally separated from the other OMs in the triplet by 120° (azimuth). The vertical distance between each triplet is 14.5 m. The lower 100 m of each detection unit is kept free to avoid pollution close to the seabed [10].

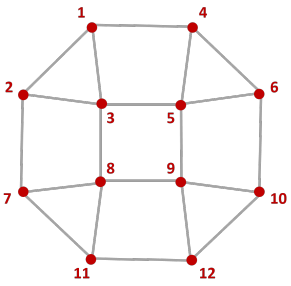

Figure 3.1: Seafloor layout of the twelve detector lines. Line numbering can be seen.

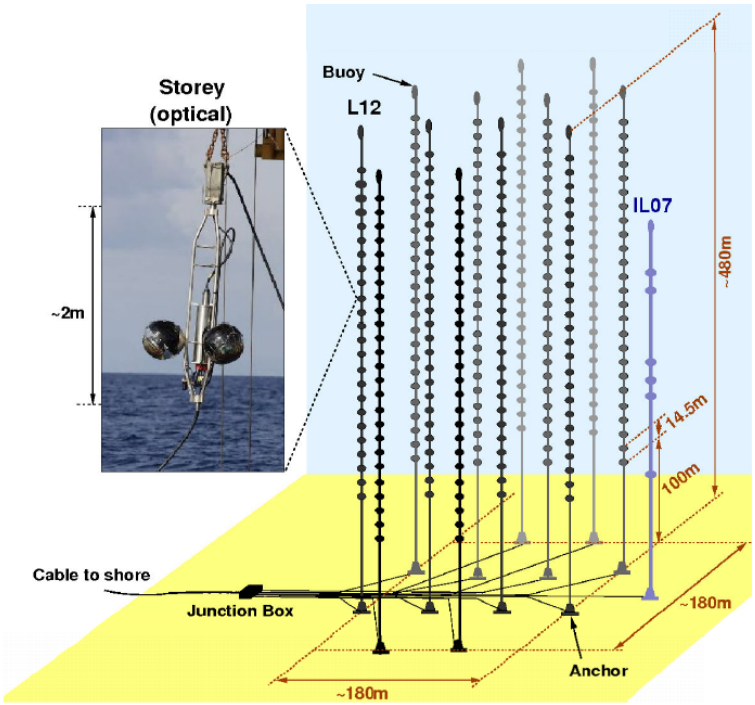

Figure 3.2: Schematic view of the ANTARES detector; the magnified view shows one storey with three OMs, one of them is covert. The picture is taken from [10] with a few modifications from [60].

Figure 3.3 shows the components of an OM. It consists of a ten-inch Hamamatsu photomultiplier (PMT) in a high-pressure resistent glass sphere together with a special gel for optical coupling and a μ-metal cage for magnetic shielding against Earth's magnetic field. A *hit* is defined as the time and amplitude of a signal resulting from a photon hitting a PMT, which, in turn, releases photoelectrons (p.e.). These analogue signals are digitized by two analogue ring samplers (ARSs), which alternately integrate the voltage signal from the PMT. When one ARS has collected data for 25 ns, a dead time of 250 ns follows and the other ARS takes over [61]. This is visualised in the time residual distribution presented in Figure 3.5. The time residual is defined as the difference between expected and measured hit time. Three peaks are observed in the picture, that are related to the first ARS sampling, its switch to the second ARS and the first ARS after the dead time. The small accumulation before the first ARS peak is due to scattered hits.

All strings are connected to a central junction box (JB) located on the seabed. It sends the full data stream to a computer farm on the coast via an electro-optical cable. There, the data is filtered for physical events (see next chapter). Since the ropes move and rotate with the sea current, tiltmeters and compasses are installed on each storey and are polled for data every two minutes (positioning system). A calculation based of the buoyant and drag forces of horizontal displacements was performed to plot the

line shape in Figure 3.4. Even at the high sea current of 20 cm/s, a relatively small deviation of, at maximum, 15 m is visible at the top of the line. Additionally, each string is equipped with five hydrophones as an acoustic second positioning system with a precision better than 15 cm and with four LED optical beacons for time calibration, reaching a precision better than 1 ns.

The main purpose of the ANTARES telescope is defined as the discovery of cosmic neutrino sources through the measurement of high-energy muon tracks. Furthermore, the ANTARES detector provides data for biology, the environmental sciences and oceanography [10].

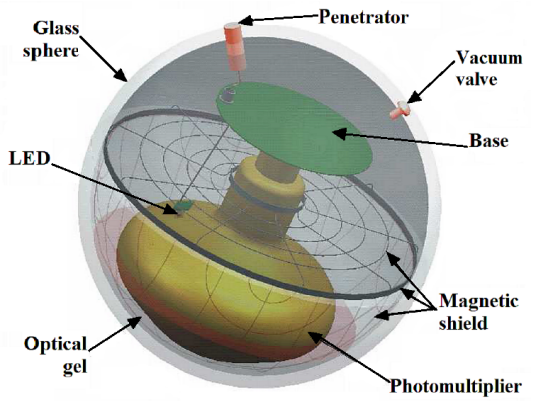

Figure 3.3: Schematic view of an OM. It contains a PMT, gel for the optical coupling of the PMT and the glass, and an LED for calibration purposes and magnetic shields. The picture is taken from [62].

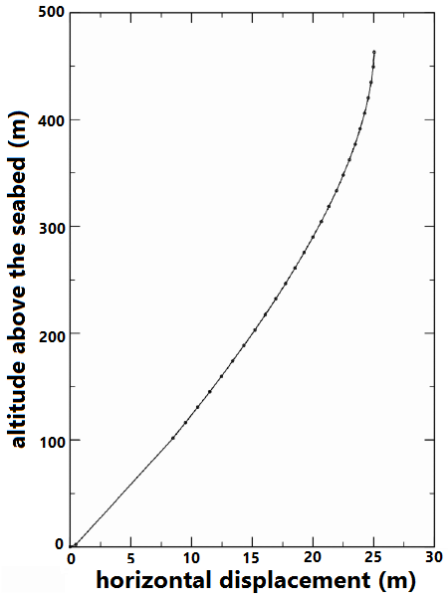

Figure 3.4: Deviation of a line for a sea current of 20 cm/sec. The top of the line is displaced by roughly 15 m. The picture is taken from [62].

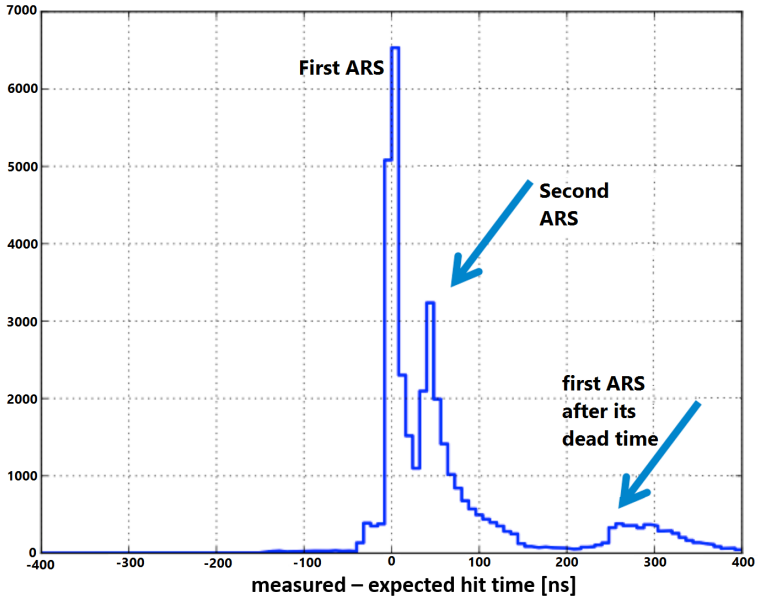

Figure 3.5: Time residual distribution. Plotted with the second RBR test sample that will be introduced in Chapter 4.1.

3.2 Trigger algorithms

On shore trigger algorithms are applied to the collected data stream to search for physical correlations between the hits; these software algorithms can also run in parallel. In general, the data stream is divided into packages labelled as runs, which may not exceed a size of a few GBs. One run typically extends between one and eight hours, depending on the amount of background noise.

To reduce the amount of data, only hits above a threshold of 0.3 p.e. are sent to shore. Below this value electrical noise from the PMT dominates the signal. Corresponding hits are named L0 hits. The so-called L1 criterion is motivated by avoiding the optical background caused by the decay of ^{40}K and bioluminescence; both are assumed to cause uncorrelated 1 p.e. hits. The corresponding L1 hits have typically a charge above 3 p.e. or are defined as at least two L0 hits occurring on the same storey within 20 ns. This time window contemplates scattered hits as well as uncertainties in time calibration and storey positioning. All hits surviving one or more triggers count as L2 hits [63]. Among others, in this thesis it was worked with snapshot hits. These are all hits of an event starting from 2.2 µs before the first LX hit and 2.2 µs after the last LX hit; whereby X stands for any integer starting from 1 (see Table 3.1). Here, event means a set of hits that passed specified triggers. The mentioned enlargement was carried out with the aim of considering all possible correlated hits that a trigger might have missed, as a photon needs this much time to pass through the whole detector [64]. The correlated hit patterns of two L1 hits in adjacent storeys within 100 ns and in the

next-to-adjacent storeys within 200 ns are filtered by the 1T3 trigger [65]. A 3N trigger is referred to as five L1 hits within 2.2 µs. A T3 trigger is a collection of two L1 hits on adjacent storeys in 80 ns or two L1 hits on next-to-adjacent storeys in 160 ns. Table 3.1 lists all the trigger algorithms and hit types that have been used in this work.

K40 trigger	two L0 hits on two OMs of the same storey within 50 ns
1T2 trigger	two L1 hits in adjacent storeys within 100 ns
1T3 trigger	two L1 hits in adjacent storeys within 100 ns, or two L1 hits in next-to-adjacent storeys within 200 ns
2T3 trigger	two 1T3 clusters in the whole detector within 2.2 µs
3N trigger	five L1 hits in a time window of 2.2 µs
T3 trigger	two L1 hits in 80 ns, or two L1 hits in 160 ns
LX snapshot hits	all hits starting from 2.2 µs before the first LX hit and 2.2 µs after the last LX hit (X stands for 1,2,3, ..)
L0 hits	hits where the PMT signal is above a defined threshold (typically 0.3 p.e.)
L1 hits	at least two L0 hits on the same storey within 20 ns, or a PMT signal above threshold (typically 3 p.e.)
L2 hits	hits which fulfill any trigger condition

Table 3.1: List of triggers and hits that have been used in this work.

Part II

Methodology

Chapter 4

Components for track reconstruction

To establish a neutrino reconstruction strategy, a huge toolbox is needed. Besides appropriate *hit patterns* and a *first track guess*, the right combination of *minimizer algorithm* and *likelihood service* plays a significant role. The minimizer's task is to move through the likelihood landscape and to search for the correct minimum. Its starting point is presented by a *track guess (prefit)*. The expression *track* denotes the muon trajectory. The desired global minimum in the likelihood landscape stands for the final reconstructed muon neutrino trajectory or track.

Besides the track quality, also the kind of likelihood influences how the likelihood landscape will look. It may be rough or even fissured, it can taper continuously to a global minimum or exhibit even more minima. Also, minimizers are suited to individual problems. They may operate with gradient methods or focus on single coordinates. A lot of them use the covariance matrix to search for dependencies within the likelihood landscape; others may jump from local minima to other positions. Eventually, diverse *fitters* regulate the starting points for the iterative minimization steps, the step length and minimization borders. In this chapter the constituents of a neutrino reconstruction strategy shall be introduced in more detail. Chapter 5 demonstrates first applications for such a strategy composed of the most suited components.

4.1 Test samples

The reconstruction algorithm was trained on two test samples. The first test sample contained atmospheric muon and cosmic muon neutrino *events*. *Events* are gathered in frames. A *frame* is defined as a kind of container including all Monte Carlo information as hits, diverse reconstruction results, primary neutrinos and so on in time slices of 104 ms [55, 66]. The first test sample was composed of $7.2 \cdot 10^6$ frames of atmospheric muons with a lifetime of roughly 16 h and of $5 \cdot 10^4$ cosmic muon neutrino frames. For detailed information on these input files see Appendix A. The simulated energy window for these muon neutrinos spans from 10 GeV to 10^7 GeV. For both file

types background noise was adjustable and was set to 60 kHz per OM to resemble real but favorable data-taking conditions. To exclude features caused by an asymmetric detector configuration, reconstruction optimisation was performed only for the twelve lines configuration. The first test sample was used up to Chapter 6.2.

Afterwards, final optimisation studies were continued with *Run-by-Run (RBR)* files as the second test sample (Chapter 6.3). RBR files are Monte Carlo simulations copying real detector conditions on a run-by-run basis; RBR version 2.0 and RBR version 2.2 were employed [67]. Here, all signal and background leptons and hadrons, except the tauon neutrino, as well as hadronic and leptonic showers, are provided. The files further include NC and CC interactions, Cherenkov light propagation, scattering and absorption effects. In this thesis the following RBR elements have been used: atmospheric and cosmic ν_e, ν_μ, NC and CC channels. All of them are listed in Table B.1. It is up to the user to give the correct weight to each event (see Chapter 4.2). RBR input files used for the second test sample refer to the twelve line period only, which started in May 2008. The last run that was considered was taken in January 2012. Corresponding run numbers range from 34410 to 62000, whereby only each 4th run that ends with zero has been designated for processing to avoid possible correlation effects (208 runs in total). Not included are sparking runs and a few runs that were not available. The integrated lifetime of this sample is 20.7 days. Run numbers ending with zero may officially be taken for analysis without an unblinding request.

Additionally, the whole dataset from 2007 and 2008 may be used without this request; this was made public according to a talk from P. Coyle at the collaboration meeting in Leiden in May 2014 [68]. This was the third sample in this thesis, composed of data and mentioned RBR files. It was used in the final analysis.

4.2 Weighting procedure

The simulated atmospheric and cosmic particles of NC and CC interactions of both test samples are per se not equipped with the correct weight w_{corr}. For an analysis the user has to re-weight the particles with the required flux assumption $\Phi_{\text{ref}}(E, \theta)$ adjusted on the time duration of interest T_{irr}. The flux depends on the energy E and the zenith θ of the incoming particle. Each event has to be re-weighted with help of the *generation weight* $w2$ via:

$$w_{\text{corr}} = w2(E, \theta) \cdot \Phi_{\text{ref}}(E, \theta) \cdot \frac{T_{\text{irr}}}{N_{\text{gen}}} \qquad [1/\text{y}] \tag{4.1}$$

Thereby, N_{gen} means the number of generated events per Monte Carlo file; $\Phi_{\text{ref}}(E, \theta)$ contains a factor $\Phi_0 \cdot E^{-\gamma}$ depending on the assumed spectrum; Φ_0 is a normalisation constant and $w2(E, \theta)$ has the unit $\text{GeV} \cdot \text{m}^2 \cdot \text{sr} \cdot \text{sec} \ / \ \text{y}$.

For cosmic neutrinos $\Phi_0 = 4.5 \cdot 10^{-8}\,\mathrm{GeV}/(\mathrm{cm}^2 \cdot \mathrm{sr} \cdot \mathrm{sec})$ per neutrino flavour and $\gamma = 2$, as previously described in Chapter 1.1 (Waxmann-Bahcall limit). Real data may not be weighted. Therefore, data have the weight $w_{\mathrm{corr}} = 1$. Atmospheric particles as electron neutrinos and muon neutrinos were weighted with the Bartol flux (see Equation 4.2). This can be performed in SeaTray (see Chapter 4.3) by multiplying each event with the *global weight* $w3$ in the following way:

$$w_{\mathrm{corr}} = w3(E, \theta) \cdot \frac{T_{\mathrm{irr}}}{N_{\mathrm{gen}}} \qquad [1/y] \tag{4.2}$$

Neutrinos within the first test sample were only weighted with $w2 \cdot E^{-2}$; constant factors have been omitted. Atmospheric muons of the first test sample were weighted with Equation 4.2 and data with 1. The second test sample, consisting of RBR cosmic muon neutrinos (RBR v 2.2) and atmospheric muons (RBR v 2.0), was weighted with the help of Equations 4.1 and 4.2. Additionally, these weights were adjusted to 20.7 days of data-taking. It is worked with the final data sample consisting of real data from 2007 and 2008 and associated RBR Monte Carlos in the analysis part (Chapters 7 to 9).

4.3 SeaTray framework

Reconstruction algorithms have been conducted in the *SeaTray framework*. The steering file is usually written in the Python scripting language and is built up in a modular structure. The data flow starts with a *data reader module* and is then passed from module to module in data containers called frames, until a *writer module* stores the final events. A frame can consist of several events, like reconstructed electrons or muons including all their simulated properties. One module may search for a special hit pattern on the optical modules *(hit selector module)*; another module may allow the user to choose a special calibration set concerning the data-taking time of interest *(calibration module)*. Users may also generate their own modules in the style of existing ones. Within the framework, modules are independent and do not affect each other. Next to the modules there exist *services*, representing necessary tools for some modules. The *database access service*, for instance, guarantees access to the database to look for special run specifications, while a *random number generation service* is required by modules that operate with random numbers.
Track reconstruction sequences like AAFit or BBFit can be modularly put together. These *track reconstruction modules* belong to a framework in the framework with the name *Gulliver framework* (see Chapter 4.4). To be available and modificable for all members in the collaboration, all programs are uploaded into the *SVN* (*version control system SVN*, see [69]), which manages the single SeaTray versions.

4.4 Reconstruction components

Mandatory elements for maximum likelihood fits within the Gulliver framework are a *minimization algorithm service*, a *likelihood service*, a *hit selector module*, a *parameterisation service* and a first track guess given by a *prefit*, which is also called *seed*. In the following section, all these components will be introduced in more detail. A *fitter* combines the mentioned modules and services in a dedicated way. The final result of a track reconstruction is a minimized *logarithmic likelihood (LLH)* value of a first track hypothesis. Each track path is related to one LLH value in an n-dimensional LLH space. The *degrees of freedom* n is set to 5 for most track hypotheses due to the three track coordinates and two track directions. The LLH is computed by multiplying all available *probability density functions (PDFs)*. A PDF describes the distribution of the behaviour of a photon hitting one optical module over time. Different kinds of PDFs exist, taking into account diverse quantities such as the hit charge, scattering effects or something else. Within the *parameterisation service* boundaries and step lengths for the minimization algorithm are defined. They have been properly chosen for different reconstructions and shall not be mentioned again.

Fit modules
Within the Gulliver framework different fit methods can be chosen. A lot of fit methods have been inspected. It might be worth investigating for which kinds of events the following fitters work best. This could not be tested within the scope of this thesis.

- **I3SimpleFitter**: The minimization process starts exactly at the seed, represented by one point in the LLH landscape. Then, the minimizer moves through this landscape and scans for a better minimum, following the minimization strategy provided by the *minimizer service*. In case a better LLH value is found, the new point will be returned as the starting point for the next minimization process. After a few minimization steps the hopefully global extremum will be returned as the fit result.

- **I3IterativeFitter**: The *I3IterativeFitter* works similar to the *I3SimpleFitter*, but yields worse results, at least for the given neutrino input files. Firstly, a regular fit is produced with the seed as starting point, as is the case for the *I3SimpleFitter*. The fit is also redone several times, but with a slightly shifted position of the seed. Its motion can be induced by the two quasi-random number generators *SOBOL* and *NIEDERREITER2*. They are implemented in GSL [70]. In *SOBOL* mode for instance, new starting points are extracted homogeneously from a unit square of zenith and azimuth to maximally cover the phase space. Thereby, the zenith window is freely adjustable, whereas azimuth directions span from 0 to $2\,\pi$. Borders of the unit square are transformed accordingly. It turned out that for both random services in most iterations the fit result drifted even

more from the Monte Carlo muon direction than the original seed.

- **I3IterativeRegionFitter**: The *I3IterativeRegionFitter* works in the same way as the *I3IterativeFitter*, but the output of each iteration is smeared in a more complex way within the mentioned unit square.

Minimizer algorithms

Additionally, a selection was made among several minimizer algorithms provided by *MINUIT*. *MINUIT* is conceived as a tool to find the minimum value of a multi-parameter function *(FCN)* and analyze the shape of the function around the minimum. As it offers a variety of minimization algorithms, it can be executed on individual problems [71]. The commands that were tested in this thesis include:

- **Seek**: *Seek* incorporates a Metropolis algorithm that moves through the search region to find a new minimum. With the probability $e^{-F/F_{\min}}$ it can leave the search region with central value $F_{\min}$ to a higher point with function value F. The theoretical ability to jump through function barriers is comparable to tunnelling processes that look for isolated minima. It critically depends on choosing the right average step size for the random jumps [71]. It stops if it reaches a minimum or borders (defined by the *parameterisation service*) or if it reaches the number of iteration steps (defined by the user within the *minimizer service*). The method should be used at the beginning of a fit if no reasonable starting point is known or if the existence of more minima is assumed [72].

- **Migrad**: The *Migrad* routine is based on the variable metric method by Fletcher. It converges extremely quickly near a minimum or in any nearly-quadratic region unless the function is rough. Its main weakness is its heavy dependency on knowledge of the first derivatives. It fails miserably if they are very inaccurate. It breaks at the same stopping conditions as *Seek* [72, 71].

- **Simplex**: The *Simplex* method used here was invented by Nelder and Mead as a very robust downhill routine. In the form of a simplex, the LLH landscape is scanned for minima and in each iteration one of its sides is modified. A simplex consists of $n + 1$ points (vertices) in the n-dimensional parameter space of the FCN. The size of the simplex is defined as the average distance of the geometric centre to all of the vertices. This multidimensional minimization routine is usually much slower than *Migrad*. As it does not use first derivatives, it should be less sensitive to the precision of the LLH landscape. It terminates at the same conditions as *Seek* and *Migrad* [71].

- **Minimize**: *Minimize* is equivalent to *Migrad*. If *Migrad* fails, it reverts to *Simplex* and then it calls *Migrad* again [71].

- **Simulated annealing**: This minimizer algorithm is motivated by the cooling process of molten metals. After slow cooling *(annealing)* the metal will reach a lower energy state than a quickly cooled metal, since the random energy fluctuations in an annealed system has more time to escape from local minima. To assign this idea to a minimization algorithm, a temperature parameter T has to be brought up that is decreased (cooling) during the minimization process. As start values the algorithm needs an initial temperature T_0, an n-dimensional starting vector $\overrightarrow{X}$ containing the n parameters that will minimize the system and an n-dimensional vector $\overrightarrow{V}$ that defines the search space for the algorithm. Within this phase space each parameter is minimized successively. A Metropolis criterion, already inducted in the section about the *Seek* algorithm, decides whether an uphill step will be carried out. In this way *simulated annealing* gives rejected steps a second chance.

- **CMAES**: *CMAES* stands for *Covariance Matrix Adaptation Evolution Strategy*. It neither uses gradients nor does it require their existence. This makes the method feasible on non-smooth and even non-continuous problems. Therefore, its use is recommended if the landscape has sharp jumps. *Evolution Strategy* is in general related to a searching routine among a kind of population, which is described by an amount of vectors filled with numbers ('parents'). After a first optimal amount of events or individuals have been found, several of them are exchanged, first within a small neighbourhood and then on a larger area to avoid stacking in a local minimum ('children'). Pairwise dependencies between these variables are represented by a covariance matrix *(CMA)* that additionally possess the direction for the next optimising process [73, 74, 75].

Probability density functions (PDFs)

As already discussed in the introduction, a difference exists between PDFs adjusted on the Monte Carlo truth and those resulting from continuous functions modelled to physics of particle propagation, scattering effects and so on. It cannot be said which of these approaches describes reality more truthfully. A large part of PDFs work with knowledge of the time residual t_{res}. It is defined as the difference of the actually measured or simulated hit time and the expected arrival time of the photon if it is not attenuated on its way from the vertex point. Several of the PDFs investigated in this thesis have hardly been analysed and applied within the ANTARES collaboration:

- **Pandel PDF**: The *Pandel PDF*, in the following abbreviated with *PandelPdf*, is an analytical PDF and describes the arrival time distribution of light emitted from an isotropic point light source in a medium where scattering and absorption are dominant effects. Time residual and photon path length span a two-dimensional phase space, which is split into sectors. Each sector can be approximated by derived functions. The corresponding main function $p(d, t_{\mathrm{res}})$ is a semi-physical

gamma function Γ with three free parameters; the absorption length λ_{abs} and the two phenomenological parameters τ and λ_{scat}:

$$p(d, t_{\text{res}}) = \frac{1}{N} \cdot \frac{\tau^{-d/\lambda_{\text{scat}}} \cdot t_{\text{res}}^{d/\lambda_{\text{scat}}-1}}{\Gamma(d/\lambda_{\text{scat}})} \cdot e^{-(t_{\text{res}}(1/\tau + c_{\text{med}}/\lambda_{\text{abs}}) + d/\lambda_{\text{abs}})}, \tag{4.3}$$

where d stands for the path length of an unscattered photon, c_{med} for the light velocity in the medium and N for the normalisation. The *Pandel* function has some limitations. It is undefined for $t_{\text{res}} < 0$ and has a pole at $t_{\text{res}} = 0$, which cause numeric difficulties [76, 77, 78]. The *PandelPdf* was first developed for IceCube. C. Kopper adapted it for KM3NeT, which is described in [78]. For this thesis it has been adjusted for ANTARES by fitting $p(d, t_{\text{res}})$ with parameters applicable to the time residual distribution of ANTARES Monte Carlo files. The following fit parameters have been revealed: $\lambda_{\text{abs}} = 62.50$, $\tau = 163.55$ and $\lambda_{\text{scat}} = 66.89$. The *PandelPdf* is the most frequently used PDF within the IceCube collaboration [79, 80, 81].

- **Sea-PDF**: The *Sea-PDF* is a further analytical PDF and describes the photon arrival time on a PMT. For consistency it shall be denoted as *SeaPdf* in the following. The *SeaPdf* was developed by M. de Jong for KM3NeT; C. Kopper implemented it into SeaTray. In contrast to most PDFs, it additionally needs the muon energy as input parameter. It considers direct and indirect light from muons and electromagnetic showers, which result in four final functions. They include a calculation for the amount of Cherenkov photons and their propagation. Light dispersion, absorption and scattering effects are taken into account. Information about the exact angular acceptance of the PMTs and the incidence angle of a photon is also employed [14]. All possible PDF values are stored in four PDF tables, each of them determined with the functions mentioned above. They are overlaid with a spline function for convergence reasons and are convoluted with a Gauss function with a width *tts* (transit time spread), corresponding to the time inaccuracy of a PMT. The *tts* is adjustable by the user and was set to $tts \approx 2\,ns$ to resemble real detector configuration. The PDF tables had to be generated before applying the *SeaPdf*. The KM3NeT geometry had to be corrected to the ANTARES setup. The created tables were uploaded into the *SVN* and have been part of the *release version* since release 13-05-00. The final *SeaPdf* function is shown below:

$$p(E_\nu, t_{\text{res}}) = \frac{e^{-a} \cdot c}{1 - e^{-b}}. \tag{4.4}$$

Each single value a, b and c is derived from a summation over the four PDF tables. The a refers to a probability in respect to a time before Cherenkov photons have been emitted; b refers to the time window the photon is expected, which is also variable by the user and was set to $\pm\,50\,\text{ns}$; c belongs to a distribution according to background noise. In case of secondary cascades an estimated neutrino energy

E_ν is multiplied to a, b and c.

- **AartOriginalPdf**: The *AartOriginalPdf* is the first PDF employed for the ANTARES detector. It is still a major part within AAFit [82]. It only depends on the evolution of the time residual. Hit charge, background distribution and all other effects are neglected. Supplementary, a non-physical tail is imprinted for time residuals r < -5 ns in order to allow the maximisation routine to converge properly. This PDF is plotted in Figure 4.1.

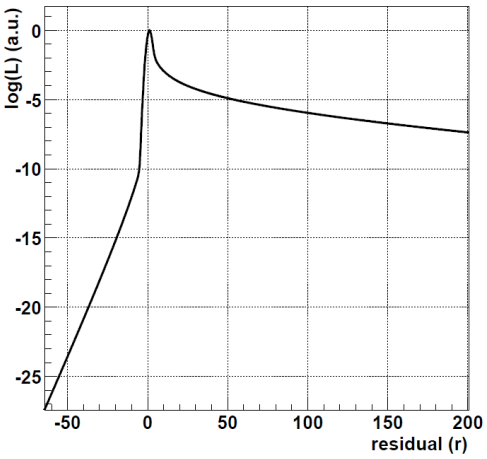

Figure 4.1: Distribution of the time residual for the *AartOriginalPdf*. The picture is taken from [82].

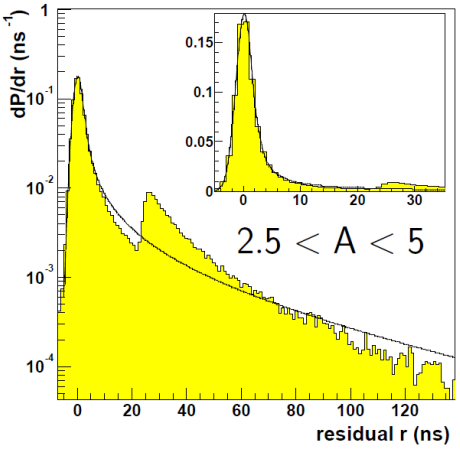

Figure 4.2: Distribution of the time residual for one amplitude bin for the *AartFinalPDF*. The picture is taken from [82].

- **AartMEstimatorPdf**: The *AartMEstimatorPdf* is an actual part of AAFit, too. It is slightly more complex than the simple time residual distribution which defines the *AartOriginalPdf*. It considers the amplitude A_i of hit i and the angular response of the optical module $f_{\text{ang}}(a_i)$. The term $f_{\text{ang}}(a_i)$ includes the quantum efficiency of the PMT, the transparency of the glass sphere and the optical gel and the effective area of the photocathode. The PDF follows the expression below, whereby $\kappa = 0.05$ [82]:

$$p(t_{\text{res}}) = \sum_i \kappa \cdot \left(-2\sqrt{1 + A_i \cdot t^2_{\text{res},i}/2} \right) - (1-\kappa) \cdot f_{\text{ang}}(a_i) \tag{4.5}$$

- **AartFinalPdf**: The *AartFinalPdf* is part of the last fit within AAFit. Such a fit leads to most accurate results, but requires a prior estimate of the muon track parameters that should be close to the true values. In contrast to the last two listed PDFs, it works with background hits:

$$p(t_{\text{res}}, a_i, b_i, A_i) = \frac{1}{N} \cdot \Big(P_{\text{sg}}(A_i, t_{\text{res}}) \cdot N_{\text{sg}}(a_i, b_i, A_i) + P_{\text{bg}}(A_i) \Big) \tag{4.6}$$

$N_{\mathrm{sg}}(a_i, b_i, A_i)$ and $P_{\mathrm{bg}}(A_i)$ represent the amount of signal and background hits concerning their amplitude. The latter is assumed to be flat. $P_{\mathrm{sg}}(A_i, t_{\mathrm{res}})$ depends on the amplitude and the time residual of hits. The function $p(t_{\mathrm{res}}, a_i, b_i, A_i)$ is continuous and differentiable and has been parameterised into five bins in units of the hit amplitude A_i. It results from the joining of three functions with a_i and b_i as their parameters. These functions refer to a time stamp before, after or within the time residual. These functions have been obtained by fits on a set of time residual histograms, which in turn have been gained from Monte Carlo simulations of muons traversing the detector. The resulting shape of the PDF can be seen for one dedicated amplitude bin in Figure 4.2 [82].

Prefits

For all fits a first rough track guess is needed. A variety of prefits are available within the SeaTray framework. *AAFit-prefit*, *LineFit*, *DipoleFit*, *FilteringFit* and the new *BBFit* (*BBFitMEstimatedTrack*) were thought to be lucrative candidates for reaching a small median angular error and a good efficiency. They shall be illuminated in the following discussion.

- **AAFit-prefit**: Within the AAFit strategy the first track guess is a kind of linear prefit. A line is fitted through the positions of hits, with the hit time as an independent variable. In order to obtain a linear relation between hit positions and track coordinates, it is assumed that the hits occur on points that are located directly on the muon track. This is expected to be a reasonable approximation, as the length of the muon track is much larger than the attenuation length of Cherenkov photons. By a simple linear matrix equation connecting these hit positions and track parameters over hit times, it can be calculated back to nearly the true muon track [82].

- **LineFit**: This algorithm produces an initial track guess on the basis of hit times, optionally weighted with the hit charge. It ignores the geometry of the Cherenkov cone and the optical properties of the medium and presumes that light travels with a fitted velocity $\vec{v}$ along a simple plane through the detector. All hit PMTs with positions $\vec{r}_i$ and corresponding hit times t_i can be connected by a line, leading to:

$$\text{track vertex:} \qquad \vec{r}_0 = \langle\, \vec{r}_i \,\rangle - \ \vec{v} \ \cdot \langle\, t_i \,\rangle \tag{4.7}$$

  The muon velocity $\vec{v}$ can be calculated via minimizing a χ^2 :

$$\text{velocity:} \qquad \vec{v} = \frac{\langle\, \vec{r}_i \cdot t_i \,\rangle - \langle\, \vec{r}_i \,\rangle \cdot \langle\, t_i \,\rangle}{\langle\, t_i^2 \,\rangle - \langle\, t_i \,\rangle^2} \tag{4.8}$$

  Finally, *LineFit* yields the vertex point $\vec{r}_0$ of the muon track, and its direction $\vec{v}$ [83].

- **DipoleFit**: The dipole algorithm considers the unit vector from one hit OM to another hit OM $\vec{r}_i - \vec{r}_{i-1}$ as an individual dipole moment. After sorting all the selected hits N_{hits} according to their hit times, the average of all individual dipole moments yields the global moment $\overrightarrow{M}$:

$$\overrightarrow{M} = \frac{1}{N_{\text{hits}} - 1} \cdot \sum_i \frac{\vec{r}_i - \vec{r}_{i-1}}{|\vec{r}_i - \vec{r}_{i-1}|} \tag{4.9}$$

  Two resulting angles (azimuth and zenith) of $\overrightarrow{M}$ define the final fit result [83].

- **FilteringFit**: In the *FilteringFit* algorithm a phase space is scanned consisting of a discrete number of generated track hypotheses, which are isotropically distributed over the sky. For each of these a hit pattern is selected using the largest number of causally connected hits. For this hit selection the time and position of the given direction is fitted by a special linear fit. The *FilteringFit* quality Q is calculable using the resulting χ^2:

$$Q = N_{\text{hits}} - w \cdot \frac{t_{\text{res}}^2}{tts^2 \cdot (N_{\text{hits}} - 3)}, \tag{4.10}$$

  with time resolution $tts = 2\,\text{ns}$ and the weighting factor w which can be set by the user. Therefore the value 0.5 was taken as it yielded good results in some tests. The track with the maximum Q value presents the fit result. S. Wagner and E. Visser have tried to improve *FilteringFit* [16].

- **BBFit**: The *BBFit* algorithm has been developed as a robust and fast reconstruction method. It produces reliable results, although it neglects precise positioning calibration as well as scattering and other effects that could deviate the muon from its straight trajectory. The two sophisticated hit selections deal exclusively with hits arising from direct Cherenkov photons. The hit selections and also the fit procedures for tracks and vertex reconstruction are based on the assumption that most of the detected Cherenkov light must be seen in the vicinity of the point of closest approach between muon path and the detection line. In a first hit selection an OM triplet is assumed as one 'big' OM and hits are merged in a complex way. A second selection operates with coincident hits in two adjacent floors or in two next-to-adjacent floors. *BBFit* treats muon reconstruction and bright point reconstruction separately [5]. The final fit quality is defined as:

$$Q = \sum_{i=1}^{N_{\text{hits}}} \Big(\frac{t_{\text{res}}^2}{tts_i^2} + \frac{a(a_i) \cdot d(d_\gamma)}{\langle\, a \,\rangle \cdot d_0} \Big), \tag{4.11}$$

  where tts_i stands for the error in the time of the hit i; $a(a_i)$ describes the amplitude of the hit and $\langle\, a \,\rangle$ the mean of all hit amplitudes; $d(d_\gamma)$ means the travel distance of the photon and d_0 is a constant.

Chapter 5

A new reconstruction algorithm

All the components of a reconstruction algorithm have been introduced in the previous chapter. This chapter illustrates how the final strategy is composed. It also reports about a lot of investigations that have been carried out.

From amongst several fit strategies, *AO-S-AF* had finally been selected; the setup of all these chains are the topic of Chapter 5.5. The primary idea behind the setup of AO-S-AF is explained in Chapter 5.1. In Chapter 5.2 the final reconstruction chain is stated. Chapters 5.3 and 5.4 report about the last selection criteria and quality filters of AO-S-AF.

In general, the final goal of a reconstruction strategy is the ideal trade-off between small angular errors and high neutrino efficiency. These quantities are defined as:

$$\textbf{Angular error} \mathrel{\hat{=}} \text{angular difference between Monte Carlo muon track and reconstructed muon track in degree.}$$

$$\textbf{Efficiency} \mathrel{\hat{=}} \frac{\text{events reconstructed with an angular error} < 5^\circ}{\text{all 3N3T triggered events}}$$

3N3T triggered events mean events that have been reconstructed, whereby their very first reference hit selection consists of hits that passed the 3N or T3 trigger or both. Among other triggers or trigger compositions, the latter triggers have emerged as proper base concerning the quantities mentioned above. All triggers have been described in Chapter 3.2.

Hits are denoted within the SeaTray framework as *RecoPulses (RPs)*; this terminology will be used further on. For several quality and robustness tests, the Monte Carlo muon track will take the role of the prefit; it will be abbreviated as *mctrack*. Furthermore, it will be differentiated between reconstructed neutrinos and muons. In the following, the term *neutrino* stands for a signal muon that arose from a charged current interaction

between a cosmic muon neutrino and a nucleus. The expression *muon* stands for a muon that belongs to the atmospheric background. The studies presented throughout this chapter perform with neutrino events. Tests for muons have also been performed. They will be mentioned, but will not be illustrated in detail.

5.1 Organisation of the input components

Among all of the possible combinations of fitters, minimizers and PDFs that were introduced in Chapter 4, and with L0 RPs and the mctrack as prefit, the connection of *I3SimpleFitter* and the minimizer *Simplex* achieved the most dramatic results with regard to the angular error and neutrino efficiency, as well as in robustness tests. Therefore, in the following chapters only the *I3SimpleFitter* and minimizer *Simplex* will be applied.

The performance of some promising fits with L0 RPs as hit sample is visualised in Figures 5.1 to 5.3. Other hit samples yielded comparable shapes. In Figure 5.1, the angular error has been drawn over a 10-logarithmic abscissa. It can be seen that fits including analytical PDFs, such as the *SeaPdf* and *PandelPdf*, count more events with a smaller angular error between [-3; -1.2] than fits that include PDFs based on Monte Carlo simulations. The *AartFinalPdf* curve in black and the *AartOriginalPdf* curve in red are more efficient in the range [-1; 0] than the other curves. The black curve differs considerably from the others as it exhibits a clear second peak at higher angular errors (within the range of [0.5; 2]). In the associated median over the neutrino energy plot in Figure 5.2, the medians of the red curve (*AartOriginalPdf*) have been evaluated to be the smallest over nearly the whole energy range. The black curve *(AartFinalPdf)* follows the same trend up to an energy of $\approx 3.5 \cdot 10^5$ GeV; after that, its median values increase, rather following the blue curve (*SeaPdf*). The two analytical PDFs have inferior median values, except for the $\approx 7 \cdot 10^5$ GeV energy bin in the case of the *SeaPdf*-fit. As can be seen, the *Pandel*-fit shape turned out to be inaccurate in reconstruction precision, but it might be appropriate for neutrino energies $< 10^5$ GeV. Studying the efficiency distribution of Figure 5.3, all values reach roughly 100 %, whereby the *PandelPdf* curve is covered by the red *AartOriginalPdf* curve.

A more intense study of the analytical *PandelPdf* might lead to a profitable outcome, as it is able to identify many muon tracks that are very close to the real track (see Figure 5.1). It could be suited as final fit after a pure and precise hit and prefit selection. Furthermore, the *PandelPdf* achieves convincing results as part of the muon strategies applied for the IceCube detector, as already mentioned in Chapter 4. Additionally, the performance of reconstruction algorithms that deal exclusively with analytical PDFs could be studied.

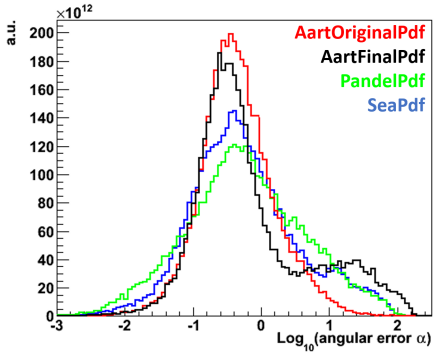

Figure 5.1: Histogram of the angular error distribution of fits with individual PDFs.

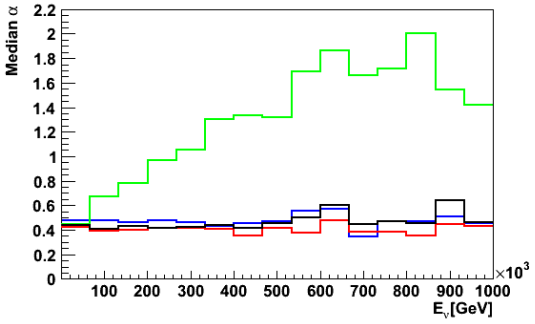

Figure 5.2: Associated median values over neutrino energy.

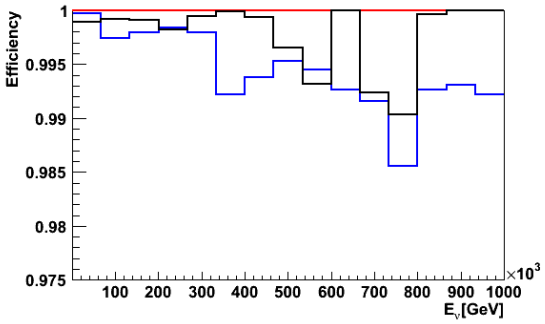

Figure 5.3: Associated efficiency values over neutrino energy.

Fit sequence AO-S-AF

In the following section, a combination of diverse fits will be focused on since it is hard to get reasonable pointing precision by applying only one fit step (see Appendix C). As the plots above indicate extreme distinctions, they have been ordered in a row using each fit as a prefit for the next fit, depending on their characteristics in performance. A variety of arranging facilities exist. Here, only the combination that was finally selected will be treated.

The idea behind the choice of *AO-S-AF*, which consists of a fit including the *AartOriginalPdf (AO)*, followed by a fit with the *SeaPdf (S)* and at last a fit using the *AartFinalPdf (AF)*, were the following (see Figure 5.1):

1. A fit with the *AartOriginalPdf*:
   The fit with the *AartOriginalPdf* exhibited superior efficiency over an appropriate angular error range. A reconstruction chain could begin with this kind of fit as many events close to the mctrack can be kept.

2. A fit with the *SeaPdf*:
   Afterwards, a fit with the *SeaPdf* could be beneficial, because it found far more events in the low angular error region than the previous fit.

3. A fit with *AartFinalPdf*:
   At least a fit with *AartFinalPdf* could be attached, as it divided nearly exact from less accurate reconstructed events.

Choice of an appropriate prefit

As the Monte Carlo truth may not be part of a reconstruction strategy (as it was the case so far), the mctrack has to be replaced by a prefit. The prefits, which were topics of the previous chapter, have been compared with various hit samples concerning the quantities mentioned at the beginning of this chapter. Among L0 snapshot hits, L1 hits, 3N3T triggered hits and 1T3 triggered hits, the L1 hits yielded persuading outcomes for all the prefits. It turned out that *AAFit-prefit*, *LineFit* and *DipoleFit* did not satisfy these requirements as well as *BBFit* and *FilteringFit* (see Figure 5.4). Therefore, the latter two prefits have undergone further tests.

Comparison of BBFit and FilteringFit

In Figure 5.4 a dramatic peak at an angle of roughly 84° can be identified as *ghost solution*, a type of fake event, which has been addressed in Chapter 2.4.3. As this behaviour is avoided more by *BBFit* and since *BBFit* is additionally shifted towards smaller angular errors, *BBFit* was stated as a prefit for all further studies.

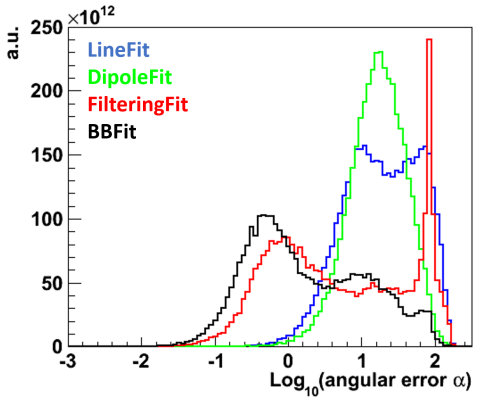

Figure 5.4: Comparison of prefits: *LineFit*, *DipoleFit*, *BBFit* and *FilteringFit*.

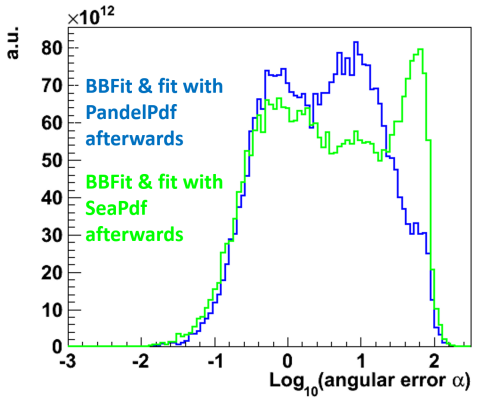

Figure 5.5: *BBFit* as prefit, followed by a fit with the *SeaPdf* (blue curve) and the *PandelPdf* (green curve).

BBFit followed by an 'analytical PDF fit'

Figure 5.5 gives an impression about the reliance of *BBFit* as prefit, followed by a fit with one analytical PDF. As the quality of both combinations are not yet sufficient for a full reconstruction algorithm, more steps are obligatory.

5.2 Final scheme of the reconstruction chain: AO-S-AF

In this chapter the final reconstruction chain is illustrated. Therein, BBFit with its intrinsic hit selections serves as prefit. In Chapter 5.3 it will be explained in more detail why it was decided for the following design.

The BBFit prefit is in total 23 times translated and tilted within the detector in a way that:

- 16 tracks lie equidistant on a cone that is tilted by 3° around the original BBFit track. Their intermediate angle is 22.50°,
- one track is the BBFit track itself, and
- six tracks are shifted by $\pm\,5\,\mathrm{m}$ in x and y directions of the track coordinate system and in z direction of the detector coordinate system, forming the shape of a cylinder.

Then, those 23 tracks are reconstructed with the help of three maximum likelihood (LLH) fits, one applied after the other. Corresponding fit sequence include the *AartOriginalPdf*, *SeaPdf* and *AartFinalPdf* (in this order) and has already been described in the previous section. The first hit sample the consecutive fits start with are 1T3 triggered hits. Then, in front of each fit step a hit selection concerning a time residual of $\pm 150\,\mathrm{ns}$ and a distance of the occurence of a hit to the muon path of 100 m is performed. Chapter 5.3 and 5.4 describe how among the 23 final fits the most suited fit result is chosen. It is named after the initials of the single PDFs: *AO-S-AF*.

5.3 Selection criterion

There is a need to formulate a selection criterion with whose help the most suitable muon track among the 23 possibilities is identifiable. For that reason, tracks were gathered in bundles. Such a bundle is defined as at least two tracks converging within 1° and with a distance of $\leqq 1\,\mathrm{m}$ to each other. If no such cluster can be set up, the track with the best LLH value is taken. Otherwise, the cluster that includes most tracks is defined as the best cluster, and within this collection the track with the best LLH value counts as final result of the reconstruction strategy. In the following sections, tests that were performed to finally propose this selection procedure will be itemised.

Choice of the multiplying process

To enlarge the admitted LLH search volume, the seed is multiplied. An inexact track direction has far more impact on backtracing to the particle's point of origin than a difference of a few 10 m in its sphere coordinates. Therefore, the seed was inclined a few times, forming the shape of a cone. This duplication is determined by two parameters: the tilt angle and the dimension of multiplication. These parameters will be treated in the next sections. Furthermore, to circumvent the risk for the minimizer to be trapped in a local minimum, the seed was parallel shifted a few times, spanning a kind of cylinder around the first track guess. A cylinder radius of 5 m has been proven as an apposite solution. This geometric profile is defined by only six duplicated seeds, assigning less weight to the translation than to the inclining step (see below).

Choice of the tilt angle

For the AO-S-AF combination, different tilt angles were checked in steps of 1°. The 3° and 6° tilt variants, shown in blue and red in Figure 5.6, perform competitively. Smaller tilt angles yield similar results, but are not assumed to cover the phase space properly. Higher tilt angles might bear the risk of becoming stuck in local minima in the case of noisy runs. Thus, the 3° variant was selected. It was also tested, how AO-S-AF performs when the six shifting processes of the initial prefit are omitted and it is operated only with the 17 residual tracks. The final result is depicted in green in Figure 5.6, and is inferior to the other curves (higher second peak). Identical behaviour as shown for the here-mentioned modifications appeared for the *PandelPdf-SeaPdf (PS)* combination (see Appendix B).

Choice of the amount of clustered tracks

It is obvious that a reduction in the 16 tilted tracks to only eight tracks would not surpass the initial number in performance. Executed tests are not attached. Moreover, focus will be on duplicating their amount to 32 tracks. This diminishes their intermediate angles from 22.50° initially to 11.25°. In the angular resolution plot of Figure 5.7 no significant difference can be noticed between multiplying the tracks 32 or 16 times. Due to computing time it was decided for the 16-track variant.

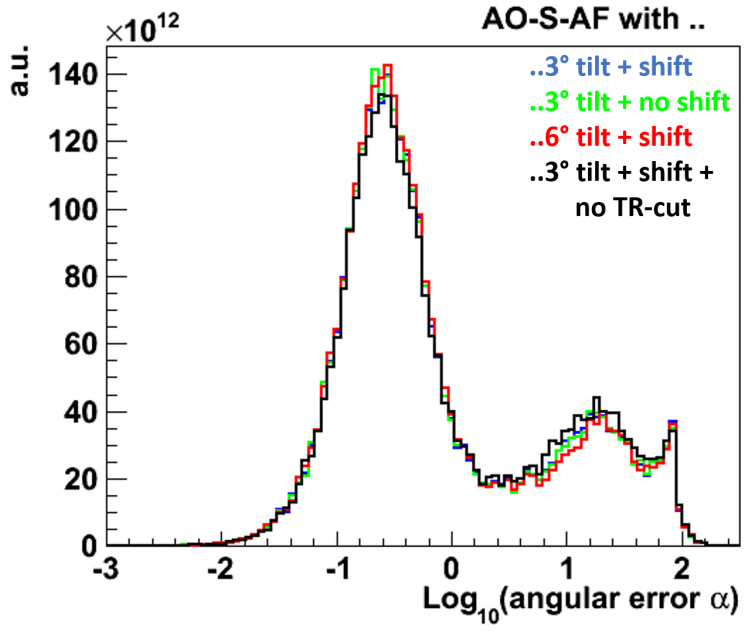

Figure 5.6: Comparison of different shift and tilt values. Blue: AO-S-AF including the BBfit track, 16 tracks tilted by 3° and 6 tracks shifted by ± 5 m. Green: AO-S-AF including the BBFit track and 16 tracks tilted by 3°. Red: AO-S-AF including the BBFit track, 16 tracks tilted by 6° and 6 tracks shifted by ± 5 m. Black: AO-S-AF including the BBFit track, 16 tracks tilted by 6° and 6 tracks shifted by ± 5 m; the time residual for the last fit (AF) was allowed to be much higher (± 350 ns instead of ± 150 ns).

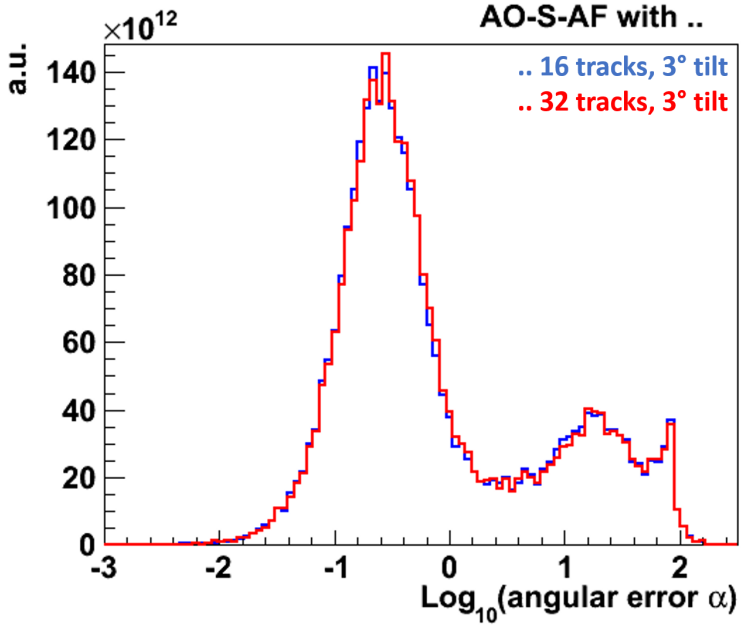

Figure 5.7: Blue: original AO-S-AF with its 16 tilted tracks. Red: AO-S-AF with 32 instead of 16 tilted tracks.

The hit selection

Another influencing quantity is the hit selection. Besides other hit selections, 1T3 hits achieved in [84] highest performance. And also as a start hit sample for the consecutive fits, among 3N3T triggered hits, L2 hits and L1 hits, 1T3 triggered hits have been proven to yield the best results. Then, in front of all three fit steps the same hit search was always applied: A symmetrical time residual distribution from ± 50 ns to ± 350 ns was varied in steps of 50 ns; and the distance from a hit to the particular fit result was from 50 m to 150 m in steps of 50 m. The values of ± 150 ns and 100 m were specified as a successful combination for the AO-S-AF chain. The borders for the time residual distribution for the *AartFinalPdf* in Figure 4.2 are with ± 250 ns much broader than the optimised time residuals for AO-S-AF. There, the distance from a hit to the track was also assumed to be 100 m. The outcome of AO-S-AF for allowed time residuals up to ± 350 ns and the mentioned distance, also enlarged to 150 m, is displayed in black in Figure 5.6 as the worst solution. As the *AartFinalPdf* is also referred to as the last of more fits within the AAFit reconstruction strategy (supposed to be the best strategy within the ANTARES collaboration so far), it can be assumed and was verified that AAFit hosts a very pure hit selection for this last fit step.

Furthermore, the electronic influence of the ARSs was inspected. It has already been outlined in Chapter 3, Figure 3.5 and is also contained in Figure 4.2, that the time residual distribution is cliffy. The SeaTray framework offers a module (*I3RemovePulses-AfterARSDeadTime*) to remove hits that occur after an ARS dead time (250 ns), as well as all information of the second ARS that fires (at around 25 ns). It was put in the chain as it was suggested to smooth the time residual distribution and thus also the LLH landscape, raising the probability for the minimizer to converge to the global minimum. Additionally, affected hits are assumed to be mainly scattered or late pulses and to bear no essential information. The result is visible in Figure D.7 (for one run only). Although this prodecure flattens the time residual curve, it could not improve the final fit result of AO-S-AF, neither for neutrinos or atmospheric muons. It was therefore not applied further.

In summary, it can be said that although the angular error shapes in Figure 5.6 on first sight look nearly the same, the shift and tilt processes listed at the beginning of this chapter were selected for reasons mentioned above.

5.4 Quality criterion

In general, the task of a quality parameter Λ_{pot} is the distinction of well and badly reconstructed events and the filtering out of atmospheric muons. The design of AO-S-AF suggests a dependency of Λ_{pot} on the bundle of selected tracks N_{conv}. Furthermore, an energy estimator like the number of hits N_{hits} could be included. After several extensive tests it was decided for the matrix of Λ_{pot} as it is shown in Equation 5.1; thereby, a, b and c stand for adjustable doubles.

$$\Lambda_{\text{pot}} = \frac{\text{LLH}}{N_{\text{hits}} - a} + b \cdot (N_{\text{conv}} - c) \tag{5.1}$$

The first expression of Equation 5.1 represents a well-proven quality definition: the reduced logarithmic likelihood. It is defined as the logarithmic likelihood (LLH) of the fit divided by the number of degrees of freedom (N_{hits} - a). N_{hits} means the number of hits contributing to the last fit. The variable a diminishes the degrees of freedom by some known parameters. It was finally decided for $a = 5$, as this is the sum of the three coordinates (x, y and z) and the two directions (θ and ϕ) of the muon path. The second term in Equation 5.1 can be regarded as a weight, which was thought to become bigger the more tracks fulfill the cluster criterion described in Chapter 5.3. N_{conv} means the number of tracks within this cluster. The final selected values, that yielded for neutrinos and muons persuading results concernig the quantities mentioned at the beginning of Chapter 5, were: $a = 5$, $b = 0.1$ and $c = 1$. Associated Λ_{pot} will be called 'final Λ_{pot}'. Their influence on neutrino events is illustrated in the diagrams of Figure 5.8.

Apart from that, further quality cuts shall be mentioned. A further cut on the hit charge, which indirectly contributes to the energy of the track, has been investigated (see below). As the quality cuts within the BBFit algorithm operate with the hit charge, these cuts were used first for this purpose. A further common quality cut has been tested, which is represented by a kind of covariance matrix estimator within the LLH landscape.

Modification of Λ_{pot}

Figure 5.8 provides angular error histograms and corresponding cumulative ditributions of AO-S-AF assuming different compositions of the first and second summand of Λ_{pot}. The green AO-S-AF curves contain the Formula 5.1 for Λ_{pot} with a, b and c as mentioned above. AAFit with its own quality parameter $\Lambda_{\text{AAFit}} > -5.2$ is attached in cyan as the last curve in the lower plot. It is hard to specify the most suited Λ_{pot}, as the interplay between efficiency and median varies. Comparing these values it can be seen that the performance of AAFit cannot be reached by any of the AO-S-AF distributions. Applying Λ_{pot} on atmospheric muons delivers similar conclusions, which are not attached.

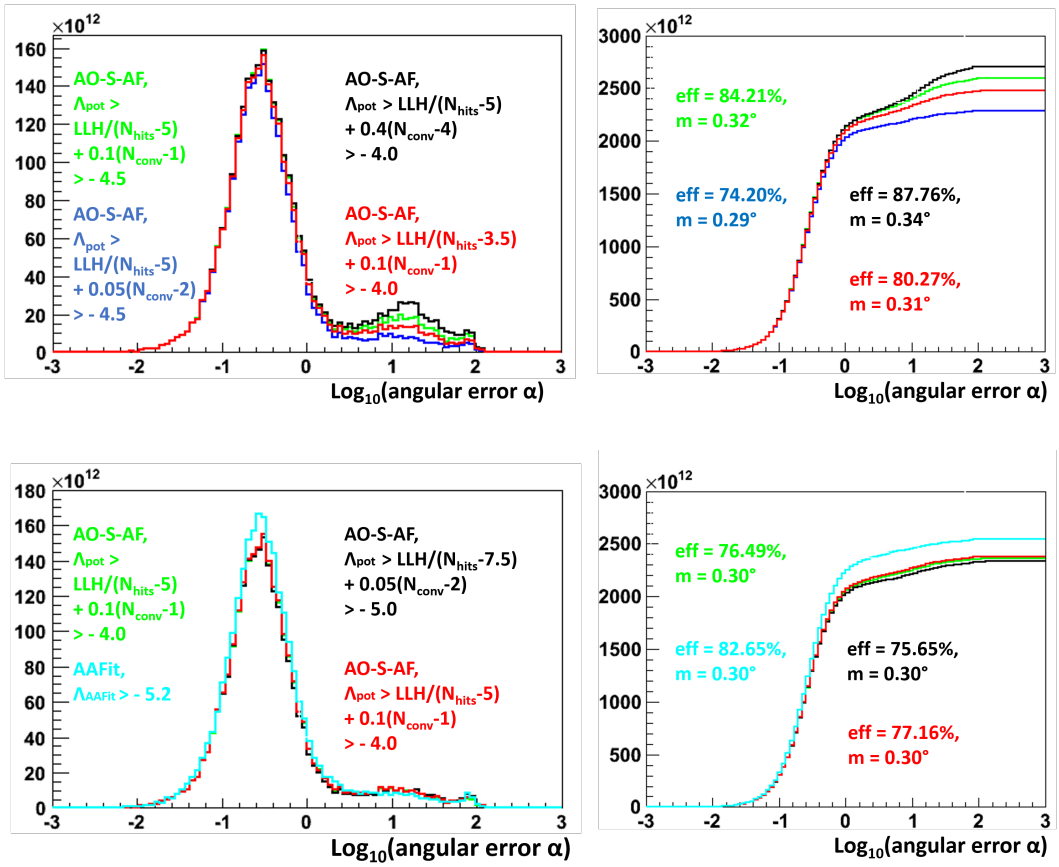

Figure 5.8: Left: Histograms with different Λ_{pot}. Right: Related cumulative distribution. AAFit with $\Lambda_{\text{AAFit}} > -5.2$ is attached in light blue.

As not much information could be gained from the simple plots in Figure 5.8 the cuts have been investigated in more detail. This can be seen in Figure 5.9, which illustrates the dependencies between both summands of Λ_{pot} and the angular error. In the upper two plots the first part of the quality parameter is drawn over the LLH value, in the left plot for angular errors $\alpha > 1°$ and in the right plot for $\alpha < 0.7°$. A cut, highlighted with the red line at $\text{LLH}/(N_{\text{hits}} - 5) = -5.5$, is able to discriminate numerous good from badly reconstructed entries. The two plots below indicate the influence of the second part of Λ_{pot}. The two accumulations at low and high logarithmic angular errors are further pulled apart by this term, facilitating their separation by a cut. More plots as these have been drawn, assigning the above-mentioned values as convenient.

Covariance matrix

The *paraboloid procedure*, a kind of covariance matrix estimator, was first implemented and applied within the AMANDA experiment by T. Neunhöffer [85, 86]. D. Boersma adapted it for the Gulliver framework under the name *I3ParaboloidFitter*; there, it was initially thought to find vertex points. The graphical construct behind can be exem-

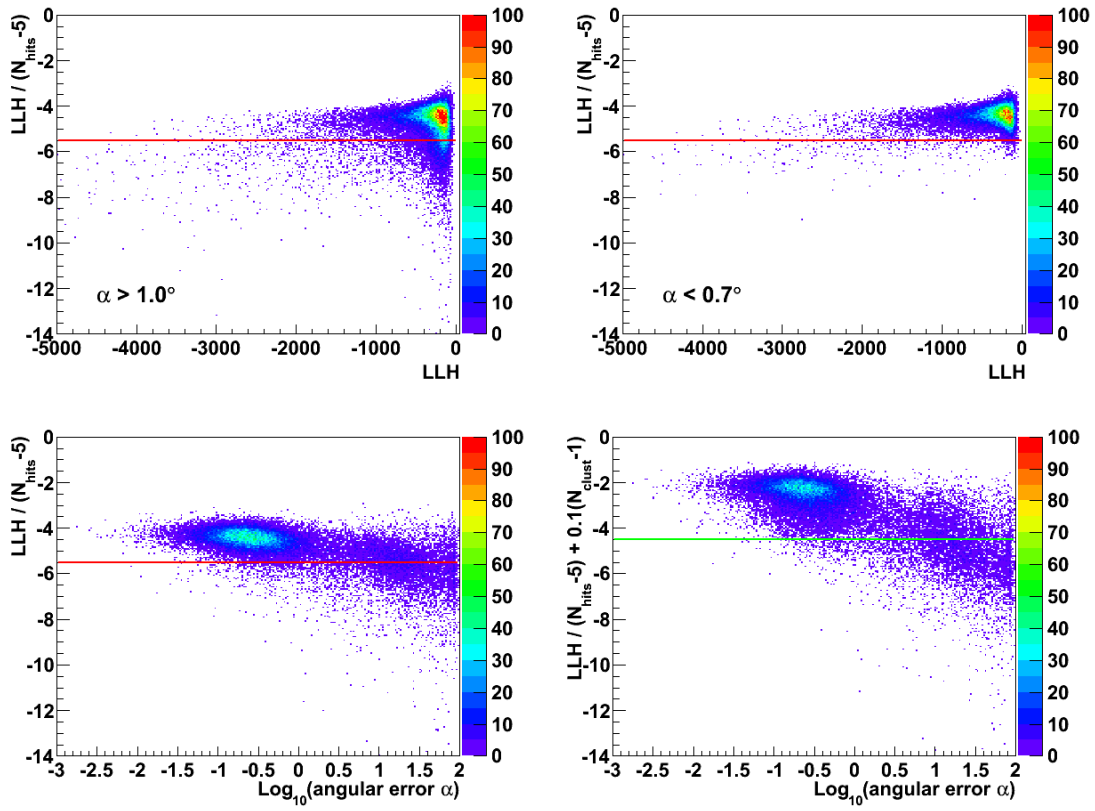

Figure 5.9: Evolution of the quality parameter Λ_{pot}, from upper left to bottom right. In the upper two plots, the first summand within Λ_{pot} is drawn over the LLH value, in the left plot for angular errors $\alpha > 1^\circ$ and in the right one for $\alpha < 0.7^\circ$. The red line at $\text{LLH}/(N_{\text{hits}} - 5) = -5.5$ divides numerous well from badly reconstructed entries. The two plots below indicate the separation of at low and high logarithmic angular errors by the second summand of Λ_{pot}.

plified as a paraboloid with its vertex point at the reconstructed minimum in the LLH landscape. In an ideal case, its surroundings are described by a paraboloid form with a surface in the phase space where '$\Delta(-\log \text{LLH}) = (-\log \text{LLH}_{\text{ell}}) - (-\log \text{LLH}_{\text{min}}) = 1/2$' stands for the 1σ confidence volume. Additionally, this surface stands roughly for the reconstruction precision, which is approximately equivalent to the angular resolution. Technically, an excessive coordinate transformation results in a two-dimensional confidence ellipse at $-\log \text{LLH}_{\text{ell}}$ with major and minor axes σ_{azi} and σ_{zen} [85, 86, 87]. The global uncertainty, abbreviated with σ, serves as a cut value and is calculable via:

$$\sigma = \frac{\sqrt{\sigma_{\text{azi}}^2 + \sigma_{\text{zen}}^2}}{2} \tag{5.2}$$

The dependencies between σ, σ_{azi}, σ_{zen}, angular resolution and the final $\Lambda_{\text{pot}} > -4.5$ are displayed in Figure 5.10. The Λ_{pot} values have been varied in steps of 0.1, starting from $\Lambda_{\text{pot}} = -6.0$ and ending at $\Lambda_{\text{pot}} = -3.0$. An optimal Λ_{pot} could not be elicited. It

becomes clear that an additional cut on the σ-values is not appreciable for AO-S-AF. The same is valid for the angular error plots of atmospheric muons, which are not shown in this work.

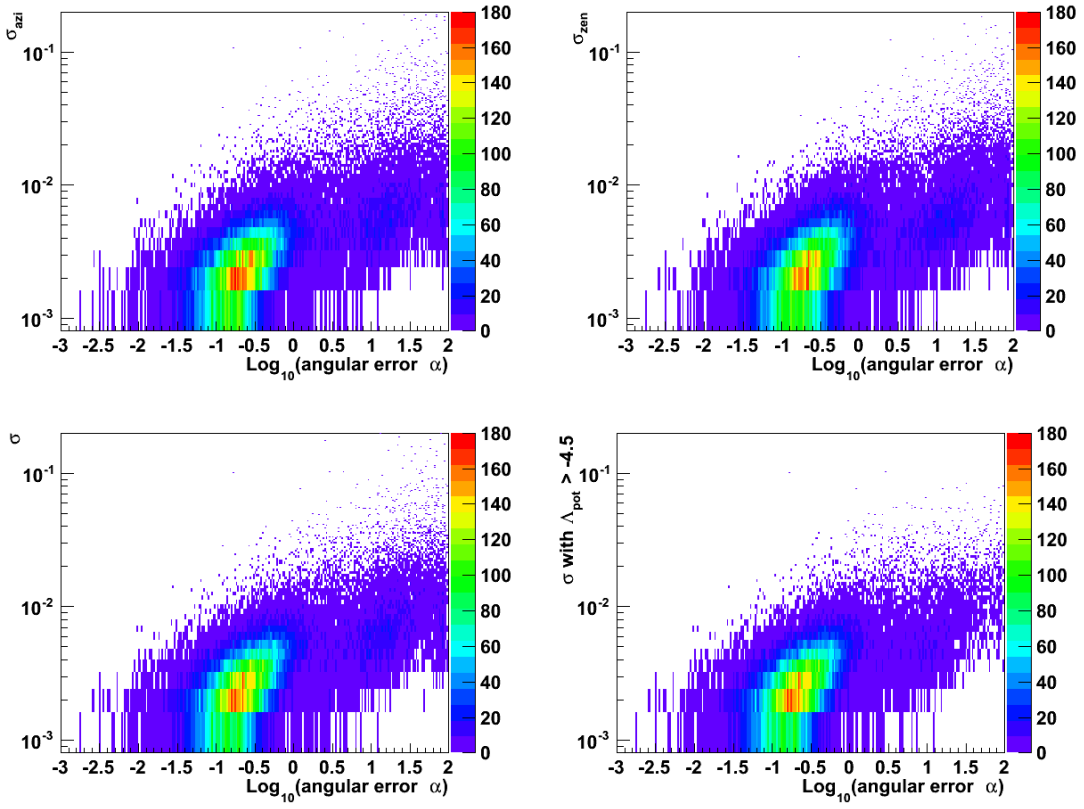

Figure 5.10: Additional quality criterion, cut on the diagonal elements of the covariance matrix of the *I3ParaboloidFitter* (σ, σ_{zen} and σ_{azi}) and on Λ_{pot} over the angular error α. No improvement can be seen.

BBFit quality cut

The BBFit quality cut provided by Equation 4.11 deals with the hit charge, which indirectly stands for the energy of the muon particle. It is proposed in [5], that BBFit's χ^2 is useful for the suppression of atmospheric muons, but not for improving the angular resolution of neutrinos. However, a cut on this value of $\leqq 500$ for neutrinos and $\leqq 400$ for showers has proven beneficial for a pretty tiny sample. This will be discussed in Chapter 6.3.

5.5 Further possible reconstruction chains

Among several fit sequences, AO-S-AF has been proven as the most convenient one. This section is about a quantitative comparison between the most promising ones. The first part of chains is shown here, a few more are mentioned in Appendix C. To investigate their performance, BBFit as well as the Monte Carlo track served as prefits. Table 5.2 summarises all of the tested sequences and their abbreviated names, which will be used in the following discussions.

	PDF 1	PDF 2	PDF 3
AO-S	AartOriginalPdf	Seapdf	–
AO-AM-AF	AartOriginalPdf	AartMEstimatorPdf	AartFinalPdf
AO-AF	AartOriginalPdf	AartFinalPdf	–
AO-S-AF	AartOriginalPdf	Seapdf	AartFinalPdf

Table 5.1: Abbreviations for individual fit sequences and the PDFs involved.

The initial situation for the individual chains was the same design as for the AO-S-AF sequence, before searching for the best track within the track cluster and before establishing convenient selection and quality criteria. For all chains 3N3T triggered events and 1T3 triggered RPs as the hit map turned out to be suitable input conditions. The hit selections for the single fit steps, as well as tilting and shifting operations introduced in the previous section, have undergone some optimisation studies. Tests concerning the hit search have already been described in the last section. As this choice yielded convenient results for all chains, it was kept. In the multiplying step of the BBFit prefit, tilt angles were varied in steps of 0.2°; after extensive studies it was decided for the 3° variant, particularly noticed in the plots below. The shift procedure was also kept. Eventually, the final fit result was defined as the track with the smallest intermediate angle to the Monte Carlo muon path, which makes the sequence independent from the cluster search routine. In the following section, this simplification shall be denoted as *mctrick*. As it had already been decided for the BBFit prefit, no further attempts to improve this tilt angle for the chains with the mctrack as prefit were made. In the following section some performance plots will be provided.

Figure 5.11 shows the angular error shape and Figure 5.12 the corresponding cumulative view for the combinations *AO-S, AO-AM-AF, AO-AF* and AO-S-AF using the mctrack as prefit. The same is repeated in Figure 5.13 using BBFit as prefit. Comparing the left plots, it can be gathered that in Figure 5.13 the efficiency obviously drops and a second peak arises. This discrepancy is mainly provoked by BBFit's hit selection. This behaviour is mirrored in Table 5.2 right column; efficiencies of the diverse prefits account particularly $\approx 74\%$ and $\approx 100\%$. Fit steps performed after multiplying the prefit hardly affect these percentages. In the lower diagrams AAFit is added.

Table 5.2 contains quantitative comparisons split in ranges of the angular error α. The chosen regimes are $\alpha \leqq 0.43°$, $0.43° < \alpha \leqq 1.0°$ and the last $\alpha > 1°$. The first border was set to 0.43°. This is identical to the angular resolution reached by AAFit for four years of data taking [4]. The border at 1° limits a relatively good angle range.

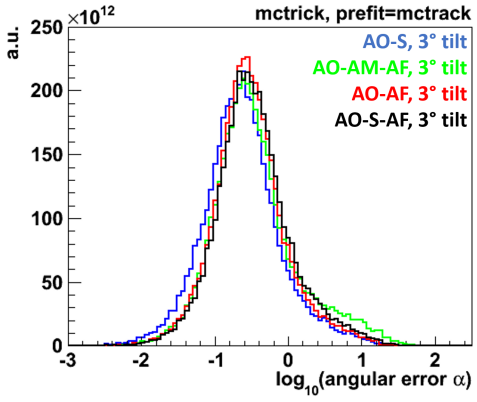

Figure 5.11: Angular error distribution of fit chains with the mctrack as prefit.

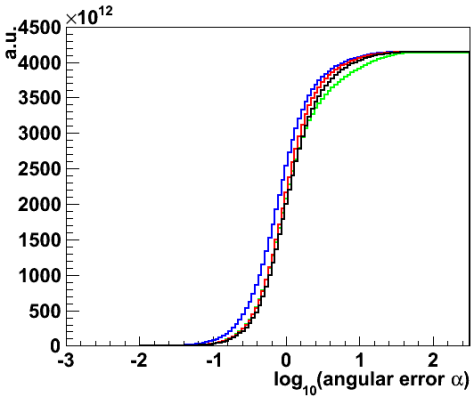

Figure 5.12: Related cumulative distribution.

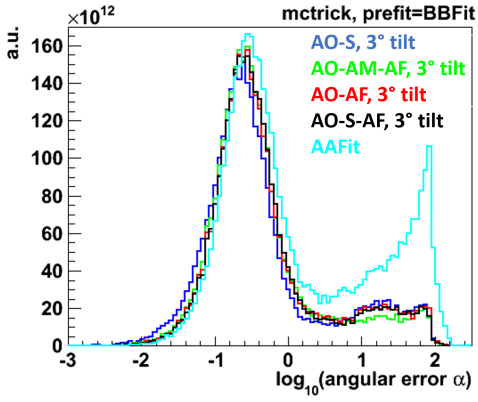

Figure 5.13: Angle error distribution of fit chains with BBFit as prefit.

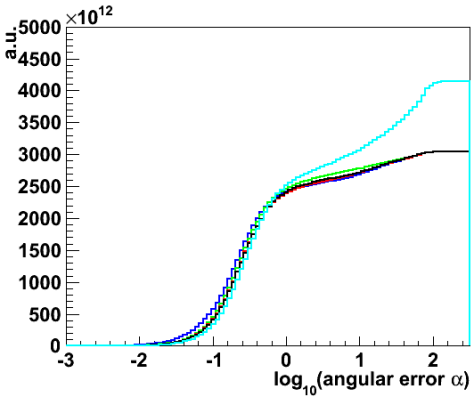

Figure 5.14: Related cumulative distribution.

- By comparing Figures 5.11 and 5.13, it is clearly apparent that among all curves the blue AO-S distribution covers most events at small angular errors and, additionally, it is the most left-shifted. This behaviour is also in agreement with the related cumulative plots (Figures 5.12 and 5.14), as well as with the left column of the efficiency Table 5.2. Furthermore, all fit combinations include more events with $\alpha \leqq 0.43°$ than AAFit, and less events in the range $0.43° < \alpha \leqq 1°$ and $\alpha > 1°$. No cuts have been applied so far.

prefit: mctrack	$\leqq 0.43°$	$> 0.43°$ && $\leqq 1°$	$> 1°$	sum
AO-S	72.46 %	16.20 %	11.28 %	99.94 %
AO-AM-AF	62.02 %	19.01 %	18.59 %	99.62 %
AO-AF	65.55 %	20.78 %	13.46 %	99.79 %
AO-S-AF	61.21 %	22.08 %	16.49 %	99.78 %
prefit: BBFit	$\leqq 0.43°$	$> 0.43°$ && $\leqq 1°$	$> 1°$	sum
AO-S	47.51 %	10.41 %	15.68 %	73.60 %
AO-AM-AF	46.26 %	12.51 %	14.82 %	73.59 %
AO-AF	44.62 %	12.47 %	16.51 %	73.60 %
AO-S-AF	44.56 %	13.01 %	16.02 %	73.59 %
AAFit	43.11 %	16.19 %	39.70 %	99.00 %

Table 5.2: Quantitative comparison among the examined fit sequences, split in ranges of the angular error. The percentage values are related to the number of 3N3T triggered events. Green cells: the highest amount of events within corresponding column. Yellow cells: smallest amount of events within corresponding column. Right column: actual amount of reconstructable events.

- In Figures 5.11 and 5.13, the green AO-AM-AF curve behaves unremarkably. Focussing on the second peak in Figure 5.13, it appears to enclose the fewest events of all curves; this is also reflected in Table 5.2. But, generally, the second peak will be filtered out by a proper quality cut, whose task is to reject misreconstructions. In the cumulative plot Figure 5.12, AO-AM-AF is the first graph that begins to flatten, which is not the case if BBFit serves as prefit (see Figure 5.14).

- In both angular error plots, at $\log_{10}(\alpha) \approx -0.6$, an excess of well-reconstructed events is visible for the red AO-AF curve. Furthermore, its slope in the cumulative plots seems to be the steepest. In Table 5.2 no conspicuous behaviour can be determined.

- Table 5.2 illustrates that AO-S-AF encloses slightly less events than AAFit, but more than the other fit orders in the second angular range. No remarkable tendency appears in the four diagrams.

- The most promising combinations seem to be AO-S and AO-S-AF, because of the big amount of events at small and the small amount of events at high angular errors. These will be topic of the following tests.

The performance of the two curves was finally classified by applying variable quality cuts. The most beneficial quality value Λ_{pot} crystallised to be the one provided by Equation 5.1 with the mentioned a, b and c and the LLH of the particular last Maximum LLH fit. Figures 5.15, 5.17, 5.19 and 5.21 contain AO-S and AO-S-AF without a cut on their particular Λ_{pot}; in Figures 5.16, 5.18, 5.20 and 5.22 it is cut on the individual $\Lambda_{\text{pot}} > -4.5$. This value came out by a comparison with AAFit, which is described in

Chapter 6. The first two plots show the reconstruction resolution and the others show some quality shapes, which are all very similar. As the median plots are slightly better for AO-S-AF and its mis-reconstruction suppression appears to work more efficiently (see Figure 5.16, right peak), this chain was dedicated for further analyses.

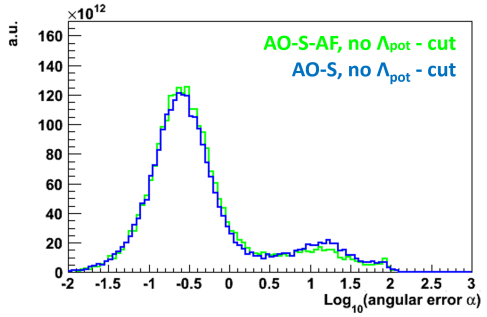

Figure 5.15: Angular error histogram AO-S-AF (in green) and AO-S (in blue); no cuts are applied.

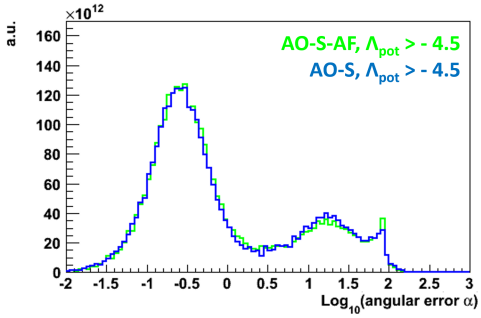

Figure 5.16: Angular error histogram AO-S-AF (in green) and AO-S (in blue) with cuts on $\Lambda_{\text{pot}} > -4.5$, respectively.

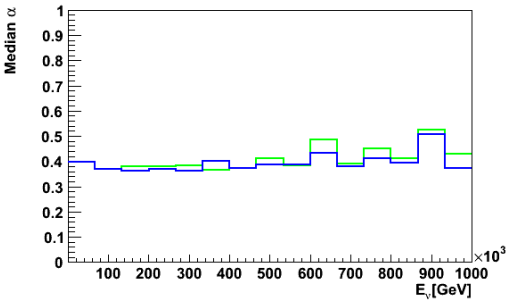

Figure 5.17: Median over energy; no cuts are applied.

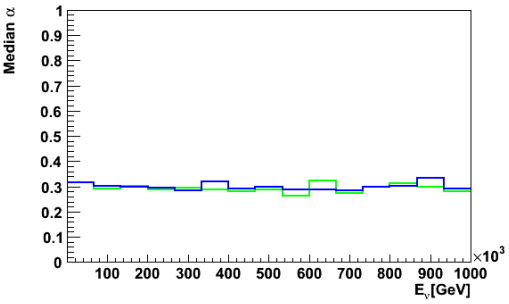

Figure 5.18: Median over energy with cuts on $\Lambda_{\text{pot}} > -4.5$, respectively.

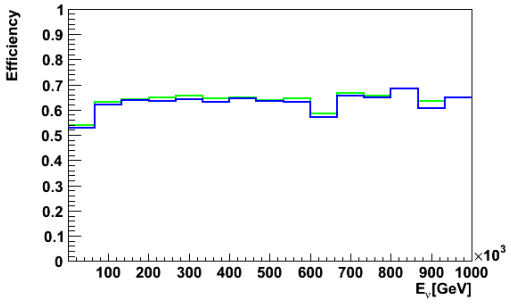

Figure 5.19: Efficiency over energy; no cuts are applied.

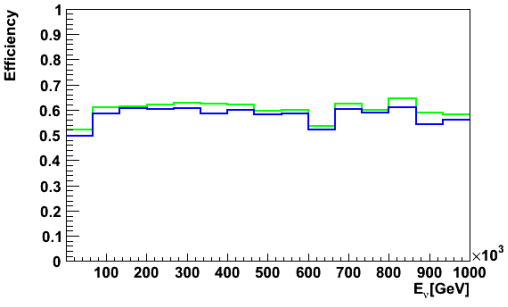

Figure 5.20: Efficiency over energy with cuts on $\Lambda_{\text{pot}} > -4.5$, respectively.

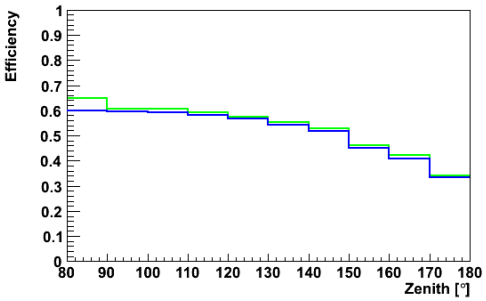

Figure 5.21: Efficiency over zenith angle.

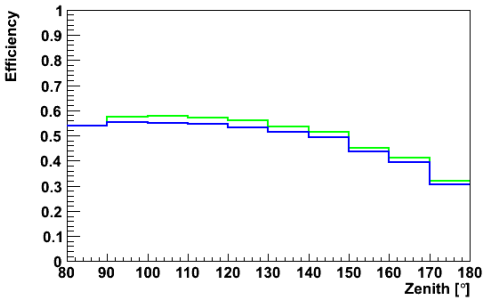

Figure 5.22: Efficiency over zenith angle with cuts on $\Lambda_{\text{pot}} > -4.5$, respectively.

Impact of different energy estimators

In contrast to AAFit, a neutrino energy estimator is a mandatory component for the SeaPdf. So far, the Monte Carlo energy has been interceded. Figure 5.23 contains angular error, median and efficiency diagrams of AO-S-AF using different energy guesses: the Monte Carlo energy in red, the energy estimator *ANNergy* in green and 1 TeV fixed energy in black. *ANNergy* is an energy estimator based on neural networks [15]. As the three curves are competitive, AO-S-AF is nearly independent from the introduced energy guesses. For all of the following studies ANNergy was used as the energy estimator, as it works irrespective of the Monte Carlo truth and it evaluates realistically the particle's energy.

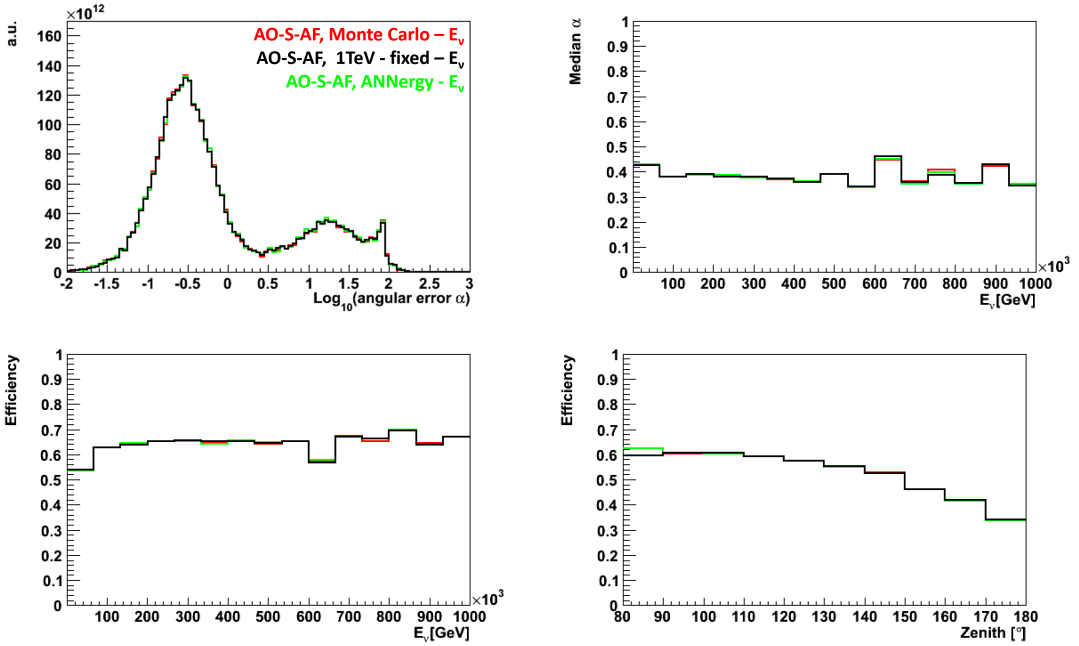

Figure 5.23: Diagrams for the application of the following energy guesses: Monte Carlo energy (red), energy estimator ANNergy (green) and 1 TeV fixed energy (black). They are compatible.

Reconstruction of BBFit's deselected events

The weak point of AO-S-AF is defined in the poor efficiency of the BBFit algorithm. Through BBFit's own hit selection, roughly 36% of the input events are thrown away. Thus, the start-efficiency for AO-S-AF is limited to 74%, whereas it extends to 99% in the case of AAFit (see Table 5.2, right column). Thus, an attempt to reconsider this percentage was made. First, for saving this fraction 1T3 triggered hits have been handed over to BBFit instead of using its own hit selection. Among L1, L2 and 3N3T triggered hits, the mentioned type of hits yielded best results concerning angular error and neutrino efficiency. Second, the 1T3 triggered hits were used as hit selection for FilteringFit, as its usual settings (L1 snapshot hits) could also not lead to improvements. The outcome of both attempts remained disappointing, which is retraceable in Figure 5.24. Therefore, the initial original BBFit algorithm with its 74% efficiency is maintained.

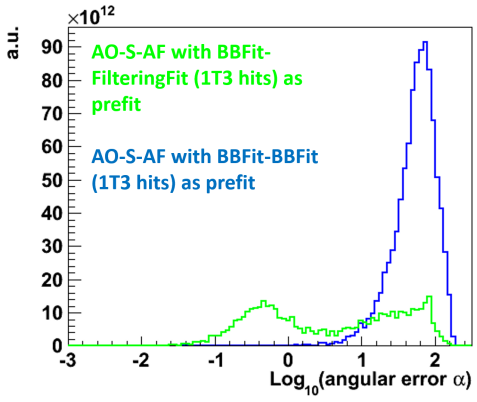

Figure 5.24: Reconstruction of events, initially filtered out by BBFit. In blue: attempt to save them with FilteringFit and 1T3 triggered input hits; in green: attempt to save them with BBFit and 1T3 triggered input hits (instead of using their original hit samples).

Chapter 6

Performance of OSFFit

As has been described in the previous chapter, from the several muon neutrino reconstruction algorithms, AO-S-AF has emerged as the most convenient. In this chapter extensive comparative studies between AO-S-AF and AAFit with regard to their quality cuts shall be given. Furthermore, the intention of Chapter 6.1 is to identify the event types to which AO-S-AF is sensitive. Among others, the quantities studied include the number of hits and hit lines and the zenith angle of the neutrino particle. In analogy to Chapter 5.5, which is about the reconsidering of particles that are filtered out by BBFit, in Chapter 6.2 an attempt is made to save the events that are disregarded by AAFit. It is intended that this percentage would enlarge AAFit's reconstruction efficiency, or at least enhance its reconstruction accuracy (median values). Improving AO-S-AF, which involves deploying new quality criteria, is discussed in Chapter 6.3. Quality cuts will be determined by provoking the transformation of AO-S-AF to *OSFFit*. Finally, studies completed with expanded data-Monte Carlo comparisons and effective area plots are the subjects of Chapters 6.4 and 6.5, respectively. Up to Chapter 6.2 the first test sample and for Chapters 6.3 to 6.5 the second test sample were used.

6.1 Comparison to AAFit

In Figure 6.1 accuracy plots of AAFit with $\Lambda_{\mathrm{AAFit}} > -5.2$ (in red), AO-S-AF with $\Lambda_{\mathrm{pot}} > -4.5$ (in green) and AO-S-AF without any cut (in black) are overlaid. These cut values have been set in a way that the green and red curves enclose nearly the same number of events within the 'left' peak. Table 6.1 lists this quantitatively in terms of the angular error range; the limits are copied from the previous chapter. The green AO-S-AF finds $\approx 2\,\%$ fewer events for angular errors $\alpha < 0.43^\circ$ and is competitive for $0.43^\circ < \alpha \leqq 1^\circ$. The most prominent discrepancy is represented by the 'right' peak. The difference between the red and green curves in this α range is $4\,\%$, and $15\,\%$ between the red and black curves. AAFit therefore appears to be more reliable than AO-S-AF so far. Figure D.8 visualizes the influence of other Λ_{pot}-values.

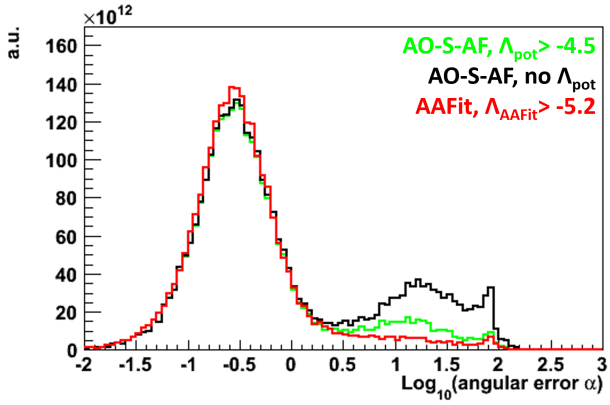

Figure 6.1: Black: AO-S-AF without cuts; only the selection criterion was applied. Green: AO-S-AF with $\Lambda_{\text{pot}} > -4.5$. Red: AAFit with $\Lambda_{\text{AAFit}} > -5.2$.

angular error α	AO-S-AF without quality cut	AO-S-AF $\Lambda_{\text{pot}} > -4.5$	AAFit $\Lambda_{\text{AAFit}} > -5.2$
$\alpha \leqq 0.43°$	37.89 %	37.58 %	40.03 %
$0.43° < \alpha \leqq 1°$	12.99 %	12.60 %	12.86 %
$1° < \alpha$	22.71 %	11.79 %	7.94 %
sum	73.59 %	61.97 %	60.83 %

Table 6.1: Percentage of successfully found muon paths concerning a 3N3T triggered reference sample, split in ranges of the angular error α. The last row contains their sum.

The motivation behind the following tests was to characterise the event properties to which AO-S-AF is more sensitive than AAFit. Double-logarithmic plots of α were made to graphically seek distinguishing marks between AAFit and AO-S-AF (see Figure 6.2). In this kind of plot, an event is only drawn if it survives all of the applied cuts. The following graphs are firstly filled with AO-S-AF results (in green). The green entries are then overlaid with the AAFit results (in red). Some remarkable event characteristics are listed below. In most cases, there are three or even four accumulations of events. These conglomerations can be divided into:

- class A event: fits well with AAFit but not with AO-S-AF (visible at big angular errors)
- class B event: fits well with AO-S-AF but not with AAFit
- class C event: fits equally well with both algorithms (the 'lower' diagonal distribution)
- class D event: fits equally badly with both algorithms (the 'upper' diagonal distribution)
- class E event: not fitted or cut away

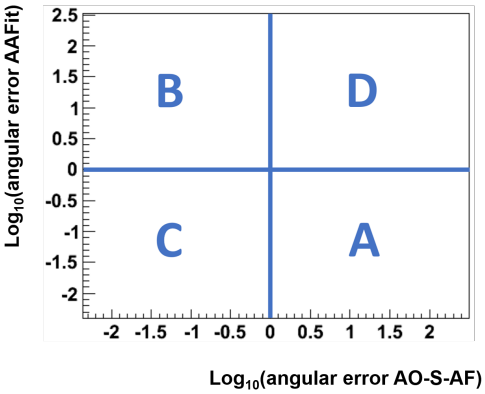

Figure 6.2: Four zones distinguish the following event types: Class A events are events that are fitted well with AAFit but not with AO-S-AF. Class B events are events that are fitted well with AO-S-AF but not with AAFit. Class C events are events that are fitted equally well with both algorithms. Class D events are events that are fitted equally badly with both algorithms. For completeness, events not fitted at all or cut away are denoted as class E events.

Number of RecoPulses, number of lines and energy

The number of RecoPulses (RPs) and lines of an event is the first point of focus. To generate comparable plots as a first guess the Monte Carlo truth has been used instead of reconstructed values. Figures 6.3 and 6.5 contain events that persist cuts on Λ_{pot}, Λ_{AAFit} and on $\leqq 4$ hit Monte Carlo lines or on $\leqq 90$ Monte Carlo hits. In both plots there seem to be at least equal amounts of class A and class B events. Figure 6.4 shows a one-dimensional histogram of hit Monte Carlo lines for both $\alpha < 1°$. This figure emphasizes that for $\geqq 5$ lines AAFit is clearly more efficient than AO-S-AF; it is hard to see, that it behaves the other way around for $\leqq 4$ involved lines. The case for $\leqq 50$ (real) RPs in the last fit, which is nearly comparable to 90 initial Monte Carlo RPs, is displayed in Figure 6.6. If only a few RPs are involved, AO-S-AF is slightly more profitable than AAFit and vice versa. In Figure D.6 these plots are shown without cuts; however, the described tendencies are also recognisable there.

Horizontal and vertical events

A further distinguishing factor between horizontal and vertical events is the initial zenith direction of the muons. The left panel of graphs of Figure 6.8 shows the case for events with zenith angles between 75° and 105°; it is again cut on both Λ values. In the following discussion, they are denoted as *horizontal events*. The plots are fragmented by three different energy zones with regard to the Monte Carlo muon energy E_μ ($E_\mu \leqq 5\,\text{TeV}$, $5\,\text{TeV} < E_\mu \leqq 10\,\text{TeV}$, $10\,\text{TeV} < E_\mu \leqq 20\,\text{TeV}$). Also here, for each energy range there is an approximately equal amount of class A and class B events visible. The associated cumulative plots are included to the right. The cumulative plots provide evidence, that in each energy regime an angular error up to $\log_{10}(\alpha) \approx -0.7$ AO-S-AF is competitive to AAFit. The cumulative distribution concerning the whole energy range (4 GeV to 10^8 GeV) behaves the same and is attached in the Appendix (see Figure D.5). Double-angle plots for the whole energy range are not displayed in this thesis as there are too many entries to gain valuable information. The Appendix also contains the *vertical scenario* for zenith angles between 165° and 195° (see Figures D.1 and D.4). The direct vertical case shall not be addressed in detail, as the corresponding input files

at higher zenith angles are represented by only a few events (see, for instance, upper pictures in Figure 6.7).

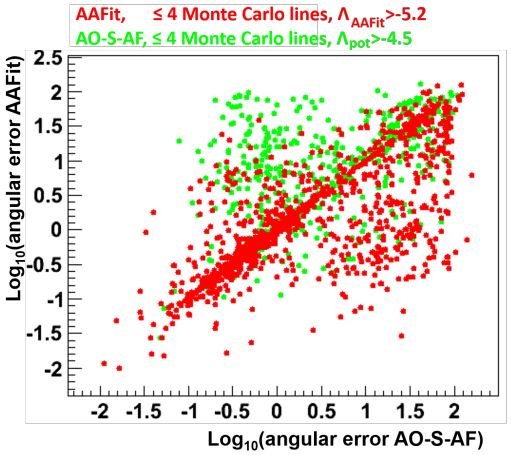

Figure 6.3: AO-S-AF with $\Lambda_{\text{pot}} > -4.5$, AAFit with $\Lambda_{\text{AAFit}} > -5.2$, number of lines $\leqq 4$.

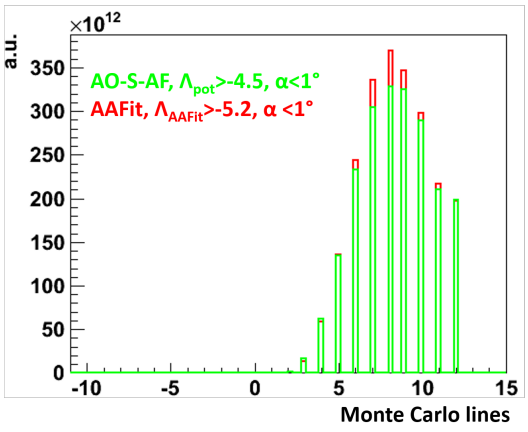

Figure 6.4: Histogram of hit lines for angular errors $\alpha < 1°$.

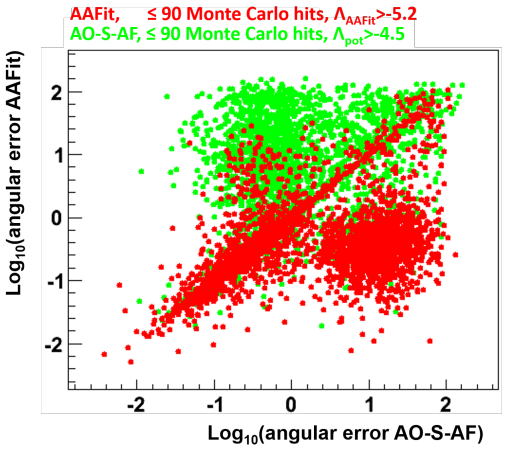

Figure 6.5: AO-S-AF with $\Lambda_{\text{pot}} > -4.5$, AAFit with $\Lambda_{\text{AAFit}} > -5.2$, number of RPs $\leqq 50$.

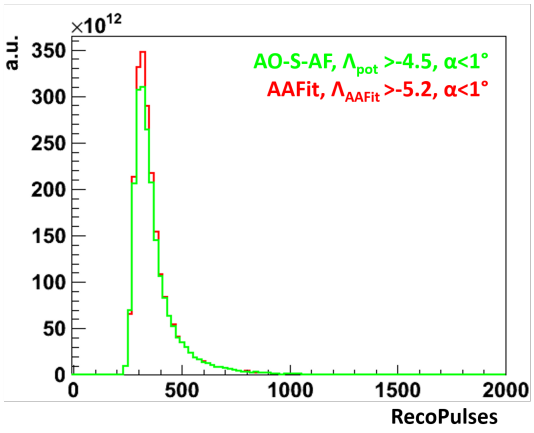

Figure 6.6: Number of RPs for angular errors $\alpha < 1°$.

Graphical comparison of zenith distributions

Figure 6.7 shows histograms of the Monte Carlo zenith angle for events found by AAFit and AO-S-AF and cuts, adapted in a way that both distributions are filled with nearly the same content; this is the case for $\Lambda_{\text{AAFit}} > -5.2$ and $\Lambda_{\text{pot}} > -4.4$ (instead of the previously used $\Lambda_{\text{pot}} > -4.5$). Nevertheless, the two profiles differ slightly. The shape of the red curve can be interpreted as being more sensitive for vertical incidence angles and the green curve as being more sensitive for horizontal incidence angles. This behaviour is consistent with the median distribution of the zenith, which is plotted in the lower right image. However, a cut on $\alpha < 1°$ leads to the disappearance of the effect

(see Figure 6.7, right upper plot). All the other fit sequences described in Chapter 5.5 behave similarly, implying that the distinction in the zenith is initiated by BBFit or the multiplying step. The median distribution of the Monte Carlo azimuth angle is shown in the lower left picture. Here, the green AO-S-AF curve is inferior to AAFit.

Finally, it can be said that for the considered neutrino input files, and if the events survive both cut values of AAFit with $\Lambda_{\mathrm{AAFit}} > -5.2$ and AO-S-AF with $\Lambda_{\mathrm{pot}} > -4.4$ or $\Lambda_{\mathrm{pot}} > -4.5$, the latter strategy finds slightly more events for $\leqq 4$ initial hit lines or $\leqq 50$ RPs in the last fit and AAFit by far more events for the complementary case. There actually exist several class A and class B events, assuming that AAFit and OSFFit could complement each other in any way (see Figures 6.3 and 6.5 and left plots of Figure 6.8). These differences were also noticed concerning their reconstructed zenith direction (see Figures 6.7, the right panel of Figure 6.8 and Figures D.1 to D.4 for vertical events). As especially this value is an important quantity for backtracking the found trace to the neutrino's origin, it should be studied more intensively. The influence of atmospheric muons is mentioned later on.

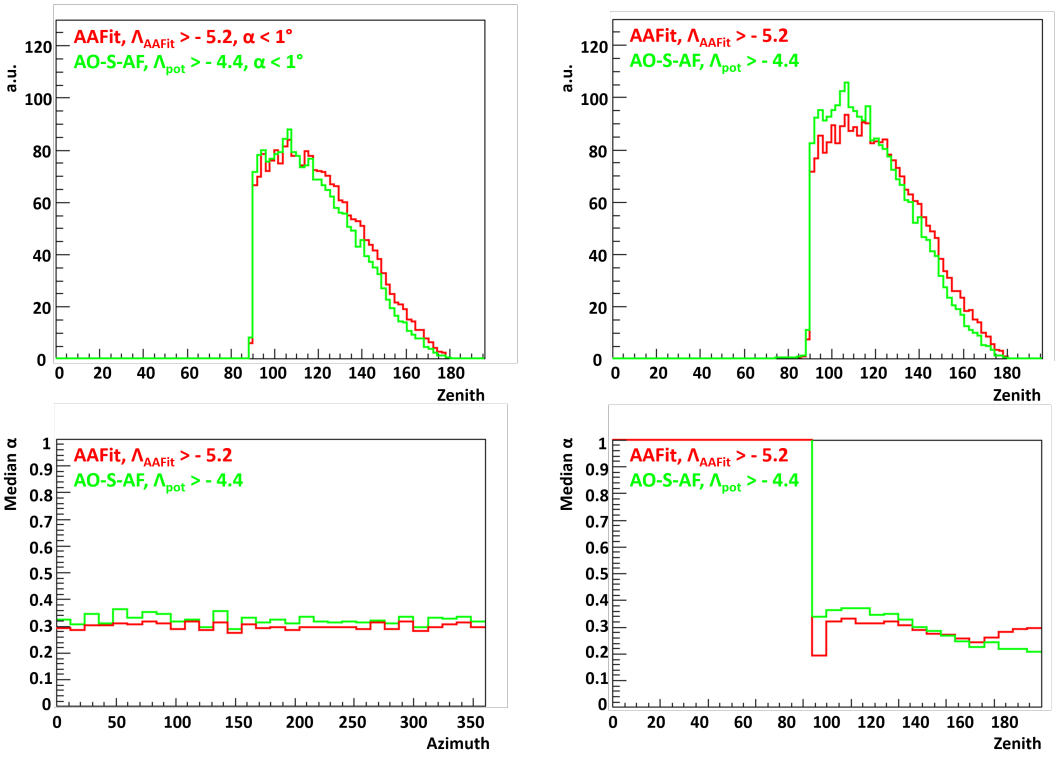

Figure 6.7: Upper plots show histograms of fitted zenith angles without and with a cut on the angular error $\alpha < 1°$. Plots below show related median distributions of zenith and azimuth.

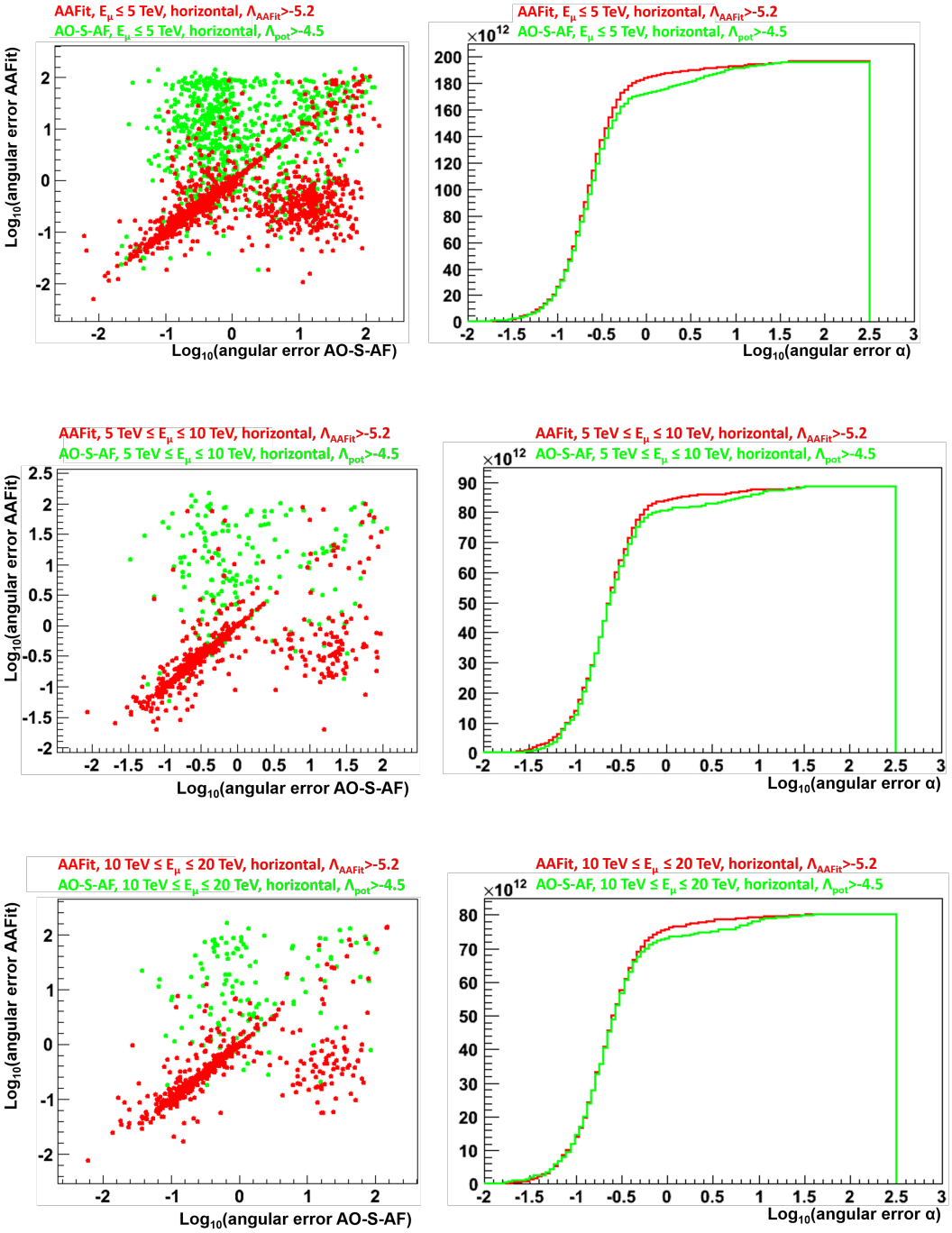

Figure 6.8: Left column: horizontal muons with muon energy E_μ increasing from top to bottom. Right column: related cumulative distributions.

6.2 Reconstruction of events discarded by AAFit

In analogy to the attempt of saving the 36% of the input tracks picked out by BB-Fit (see Chapter 5.5), the same shall be attempted for events denoted by AAFit as having insufficient quality ($\Lambda_{\mathrm{AAFit}} \leqq -5.2$) or as being unreconstructable. Its amount is roughly 39% (see Table 6.1). Furthermore, in Chapter 6.1 it has been shown that many events exist that are better reconstructed with AO-S-AF than with AAFit, which supports this intention.
In the angular error histogram of Figure 6.9, events rejected by $\Lambda_{\mathrm{AAFit}} \leqq -5.2$ are marked in blue. Marked in green are events not found or rejected by AAFit with $\Lambda_{\mathrm{AAFit}} \leqq -5.2$, but by AO-S-AF with $\Lambda_{\mathrm{pot}} > -3.5$ in the left plot (median $\approx 0.53°$) and in the right plot for AO-S-AF with $\Lambda_{\mathrm{pot}} > -4.5$ (median $\approx 0.78°$). The red curve is related to AAFit with $\Lambda_{\mathrm{AAFit}} > -5.2$ (median $\approx 0.30°$). The black distributions are particularly noted to join the red curve with the green curve, which results in a median $\approx 0.31°$ in the left plot and a median $\approx 0.33°$ in the right plot.

Therefore, it can be said that AO-S-AF with $\Lambda_{\mathrm{pot}} > -3.5$ 'saves' a few events ($\approx 5\%$ of the reference input files) AAFit would lost. If the saved events are added to AAFit, the resulting median hardly worsens (black curve, median $\approx 0.31°$). The previous $\Lambda_{\mathrm{pot}} > -4.5$ allows to many events to pass, which worsens AAFit's median a lot.

Further, it was checked which residual amount of atmospheric muon events survived the mentioned cuts. Concerning AAFit with $\Lambda_{\mathrm{AAFit}} > -5.2$ and a cut on the reconstructed zenith declination $\theta_{\mathrm{AAFit}} > 90°$ there were still 4 events left. In case of the events filtered out by AAFit with $\Lambda_{\mathrm{AAFit}} > -5.2$ and saved by AO-S-AF with $\Lambda_{\mathrm{pot}} > -3.5$ there are 22 events left, for AO-S-AF with $\Lambda_{\mathrm{pot}} > -3.2$ there are 2 events left, and for $\Lambda_{\mathrm{pot}} > -2.9$ all atmospheric muons are cut away. In this case, the mentioned 5 % diminishes to only 2 %.

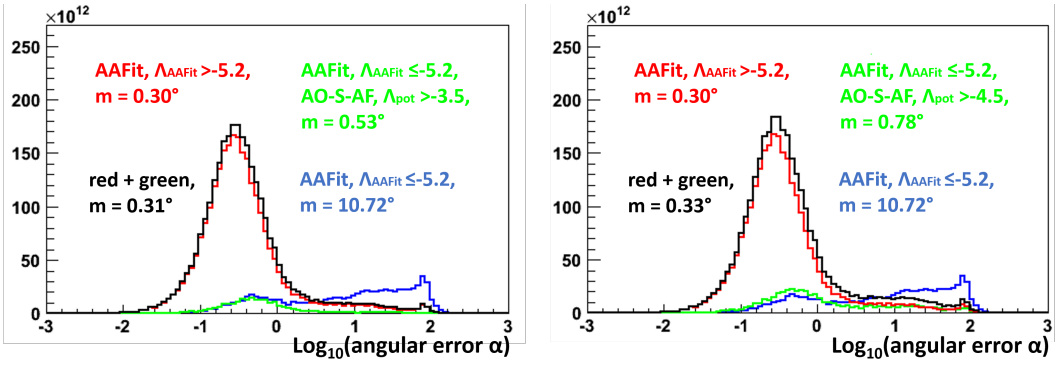

Figure 6.9: Blue: Events cut away with $\Lambda_{\mathrm{AAFit}} \leqq -5.2$. Green: Afterwards these events were reconstructed with AO-S-AF $\Lambda_{\mathrm{pot}} > -3.5$ in the left plot and with $\Lambda_{\mathrm{pot}} > -4.5$ in the right plot. Red: Official AAFit with $\Lambda_{\mathrm{AAFit}} > -5.2$. Black: Green and red curves are joined.

A more detailed analysis of the events saved by AO-S-AF

First, the properties of the events that were reconstructed by AO-S-AF alone will be focused on. This will be done with the help of cuts on diverse parameters (see Figure 6.10). The left plot of Figure 6.10 contains the (original) AO-S-AF distribution with $\Lambda_{\text{pot}} > -3.5$ in blue (median $\approx 0.28°$). The case $N_{\text{conv}} \geqq 19$ (median $\approx 0.27°$) is drawn in green; N_{conv} stands for the number of tracks converging in a cluster. The red curve only considers events generated with $\leqq 90$ initial Monte Carlo RPs (median $\approx 0.36°$) and the black curve only those generated with $\leqq 4$ Monte Carlo lines (median $\approx 0.56°$). Among all the mentioned curves, only the green distribution has smaller median values than the original blue curve. In the right plot of Figure 6.10, the cuts have been made on the complementary quantities. Here, the medians of the red (median $\approx 0.25°$) and black (median $\approx 0.27°$) curves are smaller and thus better than that of the original green curve (median $\approx 0.28°$).

By comparing all the median values it can be concluded that AO-S-AF has a higher reconstruction accuracy for events with a higher number of N_{conv}, as well as a higher number of hits (and thus probably events with a high energy and a high charge), than for the opposite quantities.

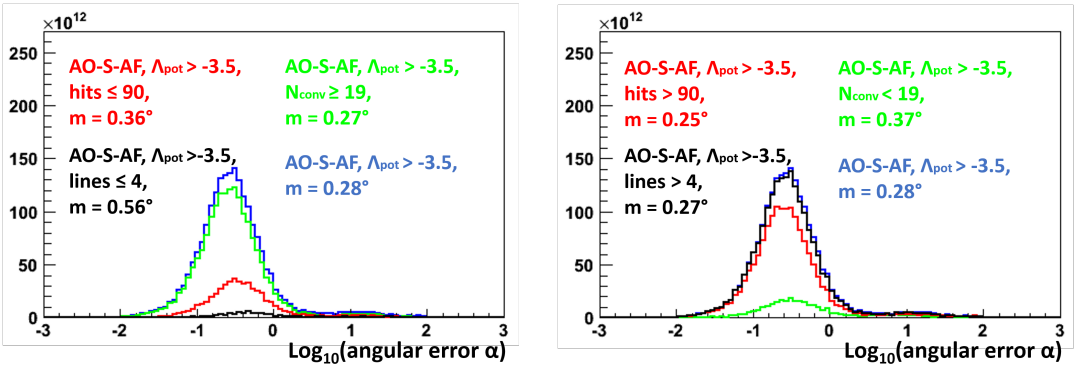

Figure 6.10: Left: Angular error distribution of AO-S-AF with cuts on diverse quantities; the right plot contains cuts on the opposite quantities. The original AO-S-AF is shown in blue. Cuts have been applied: in green a cut on $N_{\text{conv}} = 19$, in red a cut on hits = 90 and in black a cut on lines = 4.

Second, the above established cuts are applied on events deselected by AAFit (see Figure 6.9, blue curve, median $\approx 10.72°$) and reconstructed by AO-S-AF afterwards (green curve, median $\approx 0.53°$). The trend was, that also there, a slightly higher accuracy was achieved for events with a higher number of N_{conv}, as well as a higher number of hits and lines, than for the opposite quantities. This is not graphically attached. Other cuts tested were those in horizontal or vertical zenith directions and on the paraboloid σs; but still no improvement could be gained. Associated plots are not attached. However, there remains more cuts that could be investigated; for instance, only tracks traversing the instrumented detector volume.

Quality of zenith and azimuth reconstructions

Here, the focus is only on the zenith and azimuth resolution of events rejected or unreconstructed by AAFit with $\Lambda_{\mathrm{AAFit}} \leqq -5.2$ and saved by AO-S-AF and $\Lambda_{\mathrm{pot}} > -3.5$. The diagrams of Figure 6.11 show the medians of these values for different reconstructions. The two plots below include events only where the reconstructed AO-S-AF angle is $\alpha < 1°$. The green curves contain only events that are not fitted or cut away by AAFit with $\Lambda_{\mathrm{AAFit}} \leqq -5.2$, and afterwards reconstructed with AO-S-AF and $\Lambda_{\mathrm{pot}} > -3.5$. The green curves above include 5 % of all 3N3T triggered events. In the pictures below they still include 4 %. The red curve represents events reconstructed by AAFit (with $\Lambda_{\mathrm{AAFit}} > -5.2$). This distribution for AAFit plus the events saved by AO-S-AF are shown in black. The red and black median curves nearly overlie.

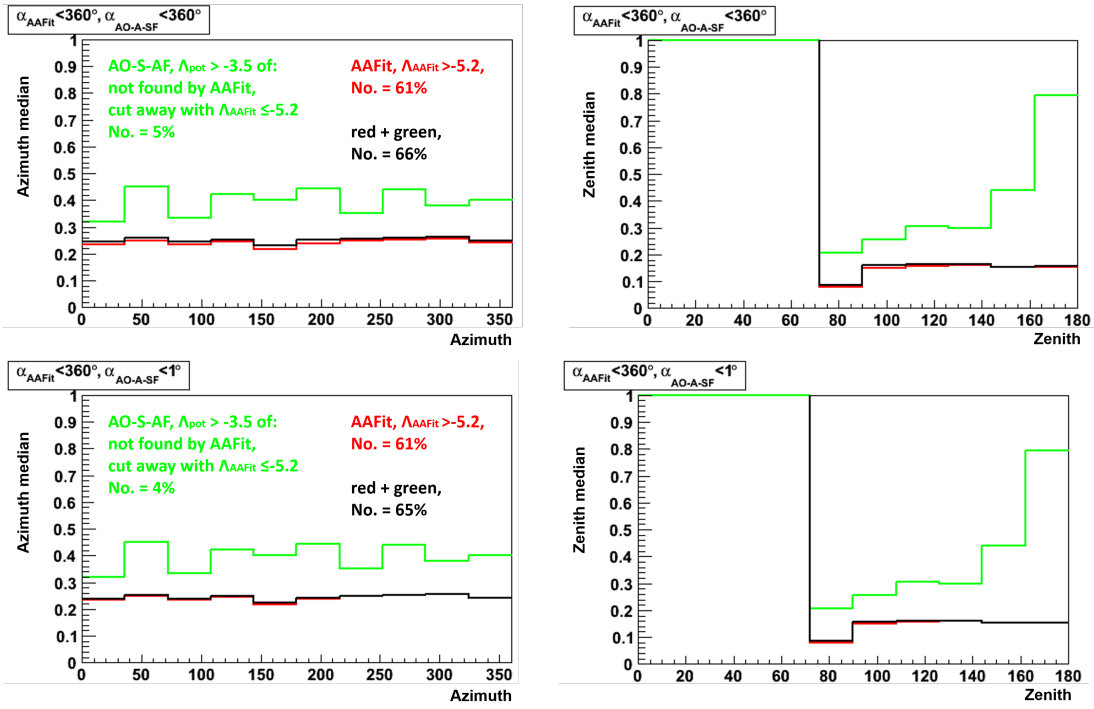

Figure 6.11: Median distributions of zenith and azimuth. Green: Events cut away or not reconstructed by AAFit, but afterwards fitted with AO-S-AF. Red: AAFit with official Λ_{AAFit} value. Black: Includes all 'red' events plus the 'green' ones. That means AAFit plus the events that could be saved with AO-S-AF. Plots below contain only entries if the reconstructed angular error of AO-S-AF $\alpha < 1°$.

It is not yet clarified how class A and class B events can be filtered out. So far, a possible application of AO-S-AF could be the usage of its reconstructed zenith and azimuth direction within AAFit. Furthermore, by applying AO-S-AF the efficiency of AAFit can be enhanced by 2%–5% and, thereby, the median value, as shown above, hardly worsens.

By comparing the median values of only AO-S-AF, the conclusion can be drawn that it is more accurate for events which exhibit a higher number of N_{conv}, as well as a higher number of hits, and thus probably events with a high energy and a high charge. The effective area plots support the high neutrino efficiency at higher energies (see Figure 6.22).

6.3 Further quality parameters

For this section the second test sample as described in Chapter 4.1 has been used. Neutrinos have been simulated with the help of RBR v 2.2 and atmospheric muons with RBR v 2.0 and were weighted as described in Chapter 4.2 with $\Phi_{\text{ref}} = \Phi_0 \cdot E^{-2} = 1 \cdot 10^{-7} \cdot E^{-2} \cdot \text{GeV} \cdot \text{cm}^{-2} \cdot \text{sec}^{-1}$ as the flux assumption of cosmic neutrinos. This section investigates further quality criteria for AO-S-AF since those mentioned in the previous sections did not yield immense success. Therefore, AO-S-AF is renamed to *OSFFit* for the rest of this work. As OSFFit contains three fit steps, it was intended to additionally store and use the information of each. During the previous chapters the quality cut provided by Equation 5.1 (with the mentioned a, b and c) has been applied. However, this equation only uses information from the fit with the *AartFinalPdf*. The LLHs of the fits with the *SeaPdf* (LLH_{S}) and with the *AartFinalPdf* (LLH_{AF}), but not with the *AartOriginalPdf*, offered advantageous details in graphical visualisation. The connections of these LLHs to signal (neutrinos) and background (muons) events are shown in Figure 6.12. The axes are defined by the quality parameters x and y, and the z axis by the entry density. A few more tests were performed to determine the expressions most suited for x and y, but will not be mentioned here. Finally, the two quality parameters x and y are described via the following formulas:

$$x = \frac{\text{LLH}_{\text{AF}}}{N_{\text{hits, AF}} - 5} + 0.03 \cdot (N_{\text{conv}} - 3) \tag{6.1}$$

$$y = \frac{\text{LLH}_{\text{S}}}{N_{\text{hits, S}} - 5} + 0.1 \cdot (N_{\text{conv}} - 1) \tag{6.2}$$

These formulas resemble Equation 5.1. $N_{\text{hits, AF}}$ means the number of hits for the last fit with the AartFinalPdf and $N_{\text{hits, S}}$ is the same for the fit with the SeaPdf. The second summand for x in Equation 6.1 is less weighted than the one of Equation 5.1. The black plotted line in the four plots of Figure 6.12, that include reconstructed neutrinos and muons, follows the linear connection:

$$x = b \cdot y + c \tag{6.3}$$

Whereas x and y are described above, b stands for the slope and c is a constant. On the one hand the line serves as a cut to reject atmospheric muons. On the other hand it

divides the badly reconstructed neutrinos from those that are reconstructed well. The function is chosen in a way so that the same amount of atmospheric muon events as for AAFit are left. This counts to one atmospheric muon event in 21 days. Thereby, the official cuts on AAFit were applied: $\theta_{\mathrm{AAFit}} > 90°$, $\Lambda_{\mathrm{AAFit}} > -5.2$ and $\beta < 1°$ [7, 8]. The line function was solved for the new quality parameters $QP1$ and $QP2$ as shown below. $QP1$ is identical to the already introduced x. $QP2$ can be gained from Figure 6.12 with the help of the linear Equation 6.3.

$$\mathrm{QP1} = x; \qquad \mathrm{QP2} = 76 + \frac{77}{4} \cdot x - y \tag{6.4}$$

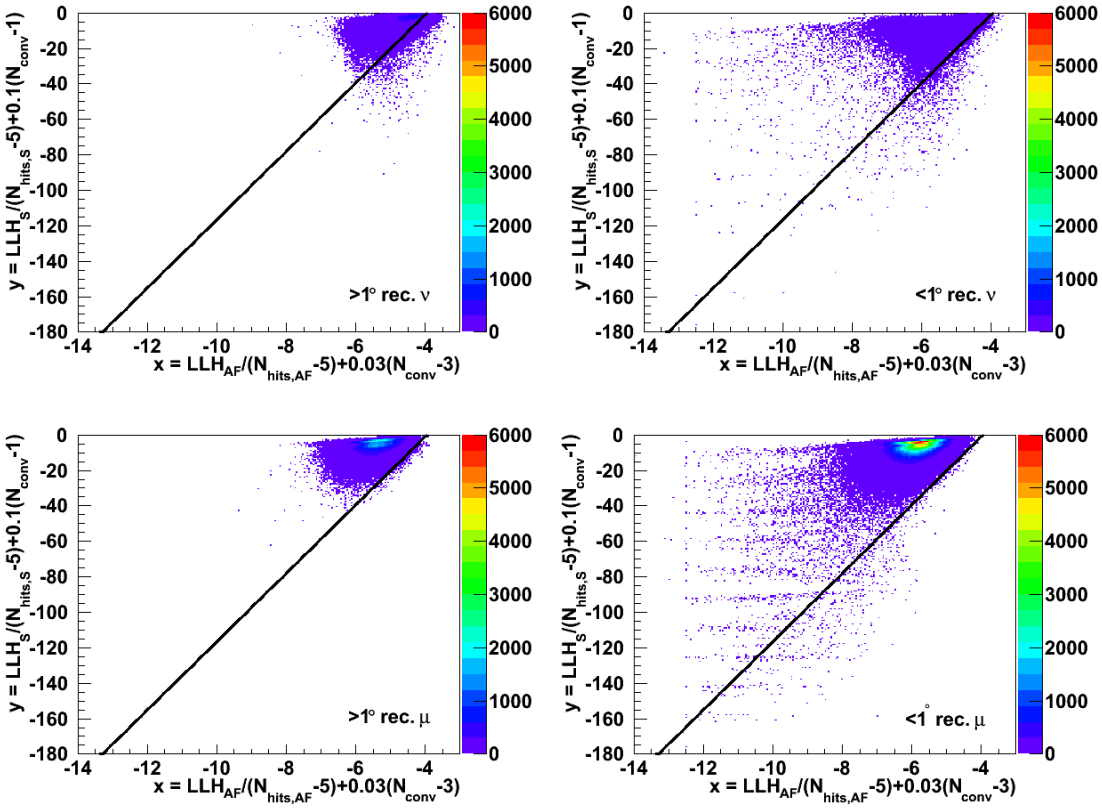

Figure 6.12: Three-dimensional plots. y-axis: $\mathrm{LLH_S}/(N_{\mathrm{hits,\,S}} - 5) + 0.1(N_{\mathrm{conv}} - 1)$; x-axis: $\mathrm{LLH_{AF}}/(N_{\mathrm{hits,\,AF}} - 5) + 0.03(N_{\mathrm{conv}} - 3)$; z-axis: number of entries. Plots above are made with the cosmic muon neutrino sample, plots below with the atmospheric muon sample. In the left plots the cut is on angle errors $\alpha > 1°$, and in the right plots on $\alpha < 1°$.

To suppress atmospheric muons in the mentioned manner, the following additional cuts have to be applied for OSFFit:

- 3N and T3 triggers,
- $QP1 > -5.1$,
- $QP2 > -10$,
- $\theta_{\mathrm{OSFFit}} > 90^\circ$ (zenith),
- $N_{\mathrm{hits,\,AF}} > 45$ (number of used final hits for OSFFit),
- *rdfClass* = 1 with 50% *rdfSafety*,
- *BBFit's track-*$\chi^2 \leqq 500$,
- *BBFit's bright-*$\chi^2 \leqq 400$.

These and more cut values were tested very intensively. The latter χ^2 values were set pretty soft, whereby a reasonable amount of events could pass through, with only really badly reconstructed events being filtered out (see Chapter 5.4). The *rdfClass* is a distinguishing criterion of the so-called *rdf classifier* concerning upward- and downward-going events [88]. It works on the basis of random decision forests. Thereby, the *rdfSafety* stands for a probability indicating how likely the particle track is directed upwards ([0.5;1]) or downwards ([0;0.5 [). Linear functions with a negative slope represent a further quality cut; but for them no beneficial solution has yet been found. Plots are not attached.

Table 6.2 lists the percentage of events that pass diverse quality cuts particulary related to 3N3T triggered events as reference events. $3\mathrm{N3T}_{\mathrm{OSF}}$ means triggered events which are additionally reconstructable by OSFFit. It can be seen that each single cut value rejects a lot of data. A very effective cut for atmospheric muon background is represented by the $QP2$ cuts. The second to last row concerns to a composed quality cut and the last row to the final cut combination applied in this thesis; in the next chapters this cut combination with $QP2 = -10$ is called: *full OSFFit cut combination*; in a few cases $QP2$ takes another value. Both cut combinations mentioned are the most effective cuts. Applying the full cut combination, still 14.58 % of cosmic neutrinos and only 1.69 % of atmospheric neutrinos remains.

cut	data	atm. ν	atm. μ	cosmic ν
no cut	$\approx 3.5 \times 10^7$	–	–	–
3N3T	$\approx 1.9 \times 10^7$ (100 %)	100 %	100 %	100 %
$3N3T_{OSF}$ (+ OSFFit finds)	19.86 %	30.43 %	37.62 %	71.61 %
$3N3T_{OSF} + \theta > 90°$	0.57 %	24.34 %	0.93 %	40.76 %
$3N3T_{OSF} + N_{hits} \geqq 45$	6.31 %	3.79 %	11.24 %	41.52 %
$3N3T_{OSF} + QP2 > -9.5$	0.18 %	7.91 %	0.14 %	28.90 %
$3N3T_{OSF} + QP2 > -10.5$	0.22 %	8.65 %	0.18 %	30.80 %
$3N3T_{OSF} + QP1 > -5.1$	0.21 %	10.44 %	0.33 %	35.47 %
$3N3T_{OSF}$ + rdf = 1	1.22 %	22.84 %	1.81 %	43.57 %
$3N3T_{OSF}$ + track $- \chi^2 \leqq 500$ + bright $- \chi^2 \leqq 400$	19.77 %	30.38 %	37.57 %	71.45 %
$3N3T_{OSF} + QP2 > -10.0 + \theta > 90° + N_{hits} \geqq 45$	$\ll$ 0.01 %	1.74 %	$\ll$ 0.01 %	15.55 %
$3N3T_{OSF} + QP2 > -10.0 + QP1 > -5.1 + \theta > 90° + N_{hits} \geqq 45$ + rdf = 1 + track $- \chi^2 \leqq 500$ + bright $- \chi^2 \leqq 400$	$\ll$ 0.01 %	1.69 %	$\ll$ 0.01 %	14.58 %

Table 6.2: Percentage of data and cosmic neutrinos, atmospheric neutrinos and atmospheric muons that survive diverse quality cuts and the 3N3T trigger concerning the second test sample. The set of cuts contained in the last row suppresses nearly all atmospheric muons (except one within 20.7 days); it will be denoted as *full OSFFit cut combination* in the next parts of this thesis.

The hard cut on atmospheric muons is accompanied by diminished neutrino efficiency. Figure 6.13 gives an impression of the modifications to the reconstruction quality that is brought about by the harder cuts. For comparison purposes AAFit is added. With the official cuts, the green AAFit curve finds 23 % while OSFFit, with the cuts mentioned above, finds only 12 % of the initial 3N3T triggered events. Its deficiency in accumulation is accompanied by clearly better reconstruction resolution. The median values of OSFFit concerning energy, zenith and azimuth are clearly smaller than the ones of AAFit. The median in the angular error α is 0.29° for OSFFit and 0.34° for AAFit. The medians of the azimuth and zenith error differ by $\approx$ 0.05° in favour of OSFFit. The zenith distributions and their splitting at higher angles resemble the ones shown in Figure 6.7, where the first test sample was used.

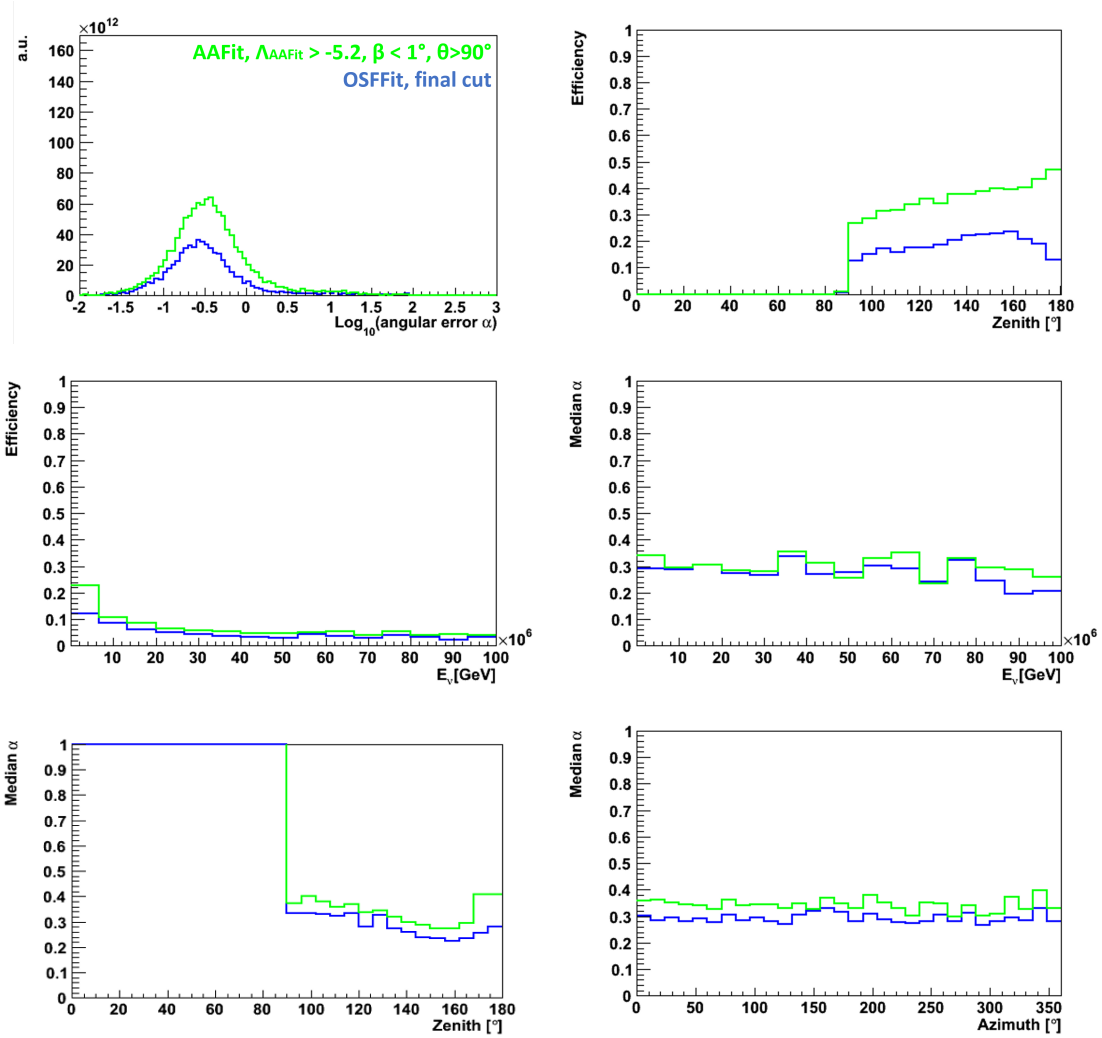

Figure 6.13: OSFFit in blue and AAFit in green applied for RBR neutrino files. Cuts of both algorithms are adjusted to keep one atmospheric muon within 20.7 days of lifetime.

6.4 Data-Monte Carlo comparison

Figures 6.14 to 6.21 contain data-Monte Carlo comparisons on a logarithmic scale without the application of any cuts. For some of them the ratio between data and Monte Carlo files is attached, which is defined as quotient of the amount of data events divided by Monte Carlo events per bin. Up to Chapter 6.2, it has been operated with cosmic muon neutrino and atmospheric muon files only; here, atmospheric and cosmic NC and CC interactions for $\nu_e, \bar{\nu}_e, \nu_\mu, \bar{\nu}_\mu$ are additionally analysed. These were weighted as described in Chapter 4.2. The zenith distributions in Figure 6.14 are nearly congruent up to approximately 140°, at which point they start to diverge. This inequality is due to an obvious lack of Monte Carlo events starting at this value, which is not visible in

the other comparison plots; it still has to be investigated. The azimuth distributions in Figure 6.15 exhibit the same symmetry. There is an excess of Monte Carlo files rather than data. The $QP1$ and $QP2$ curves of Figures 6.16 and 6.17 behave accordingly. On the right end of both distributions only a few events are present. As mentioned above, the cuts finally chosen are $QP1 > -5.1$ and $QP2 > -10$. In connection with the other cut values much background can be filtered out. Figure 6.18 displays the single constituents on which the quality cut $QP1$ is applied. All the atmospheric muons and neutrinos (yellow and red line) would be cut away by $QP1 > -4$, which is a lot harder than $QP1 > -5.1$. The black and green lines stand for the cosmic fraction desired to filter out. As they are partly overlaid by the blue curve (atmospheric neutrino showers), $QP1$ would have to be set stronger, to roughly -3.6, to get rid of all the background. The distributions for $QP2$ is shown in Figure 6.19. By far higher values than the mentioned $QP2 > -10$ are achieved. The trends in the N_{conv} plot in Figure 6.20 are quite uniform; the ratio is nearly one over the whole range. N_{conv} stands for the number of converging tracks in a cluster. Figure 6.21 shows a similar behaviour for the N_{hits} distribution, with the exception for a high amount of hits. Here, it fluctuates around 10 events. N_{hits} stands for the number of hits contributing to the last fit step.

6.5 Effective areas

The production process and meaning of an effective area plot is described in more detail in Chapter 8.2.

The effective areas for neutrinos reconstructed with diverse reconstruction algorithms are depicted in Figure 6.22; AAFit with its official cuts is drawn in red, OSFFit with the full OSFFit cut (the cuts included in the last row of Table 6.2) is shown in green, BBFit with cuts optimised for a point source search with 2007 data as described in [89] is plotted in blue and BBFit with cuts, that were actually optimised for OSFFit, is shown in black. For low neutrino energies AAFit has a higher effective area than OSFFit, whereas for neutrino energies $\approx 10\,\text{PeV}$ (x-value = 7) the effective area of OSFFit starts to lie slightly above AAFit. This effect disappears if it is cut on angular errors $< 1^\circ$, respectively (see Figure D.9). The blue BBFit curve behaves up to an energy of $\approx 3\,\text{TeV}$ (x-value = 3.5) like AAFit and falls afterwards. BBFit with the cuts of OSFFit proceeds as OSFFit but in each energy range it encloses slightly more events.

6.6 Application of OSFFit

Among the introduced fit sequences, OSFFit has been chosen as an appropriate fit sequence. It works with an analytical PDF, which is a new and different attempt for neutrino track reconstruction. Much effort was put into finding new quality parameters, with the aim to get a neutrino sample with a relatively high purity. It could be shown that OSFFit might be applicable for certain classes of events such as vertical events or events where $\leqq 4$ lines or $\leqq 50$ hits (in the last fit step) participate. This should be tested in more detail with a higher statistics test sample. OSFFit could probably complete AAFit in any way. Another potential application for OSFFit is the reconsideration of events that are rejected by AAFit. AAFit's neutrino efficiency can be enlarged by 5 %. Effective area plots show that OSFFit functions well at high energies. The mismatch in the comparison plot of the zenith distribution is most likely caused by a few neglected mupage files. They were saved with another name and could not be called by the program. Figures 6.14 to 6.21 are concerned, too. The calculated lifetime, which is written on the left side of the comparison plots, supports the idea of neglected files; it actually should be 20.7 days.
In the next part of this thesis OSFFit is used to look for neutrino events from 24 known pre-defined high-energy γ-ray sources.

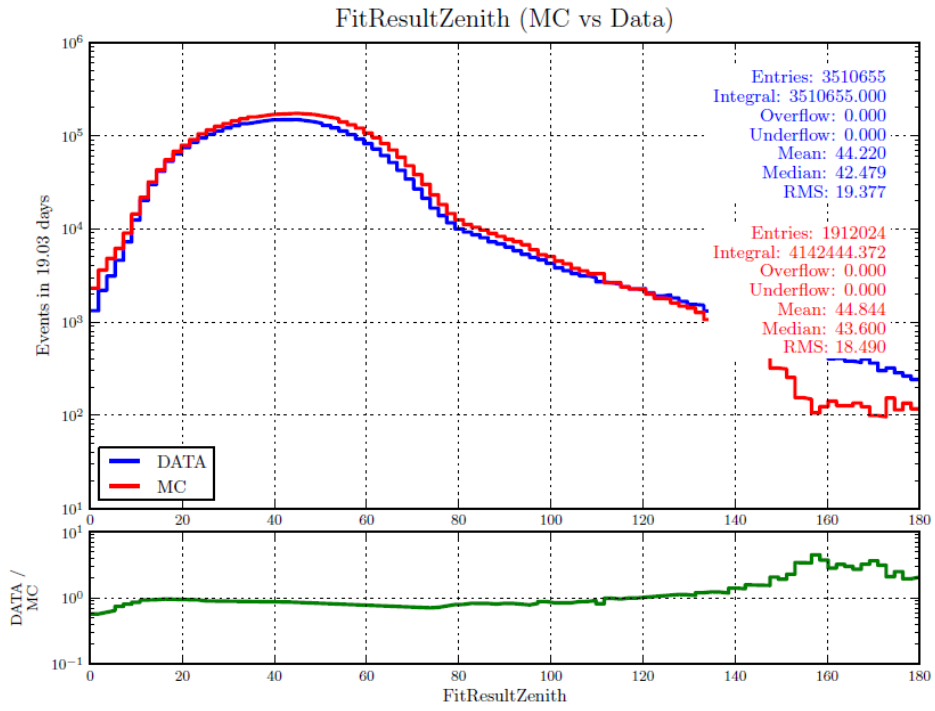

Figure 6.14: Data-Monte Carlo comparison - Zenith distribution.

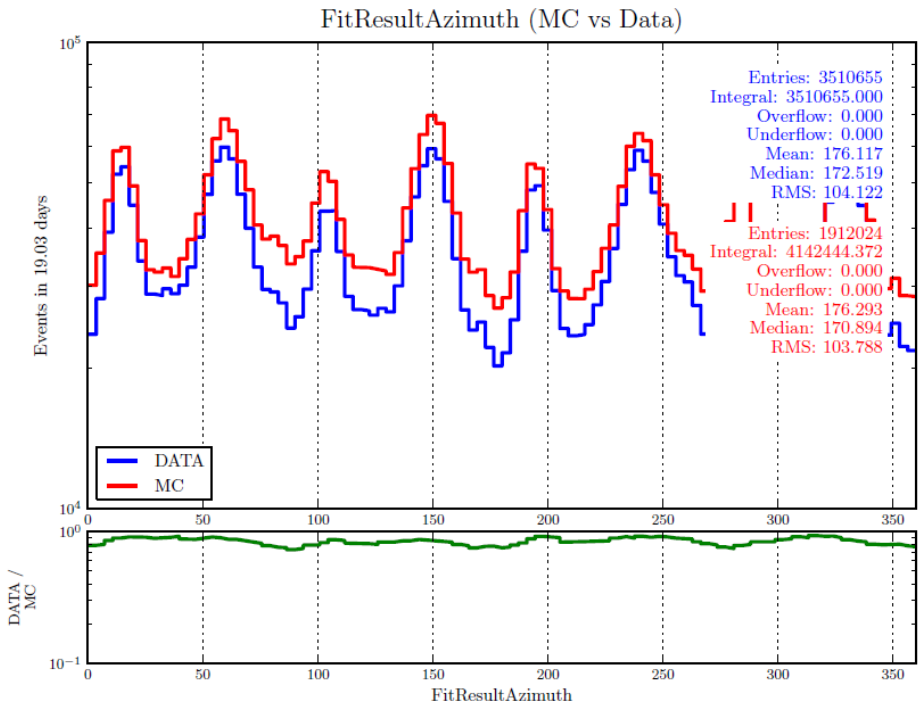

Figure 6.15: Data-Monte Carlo comparison - Azimuth distribution.

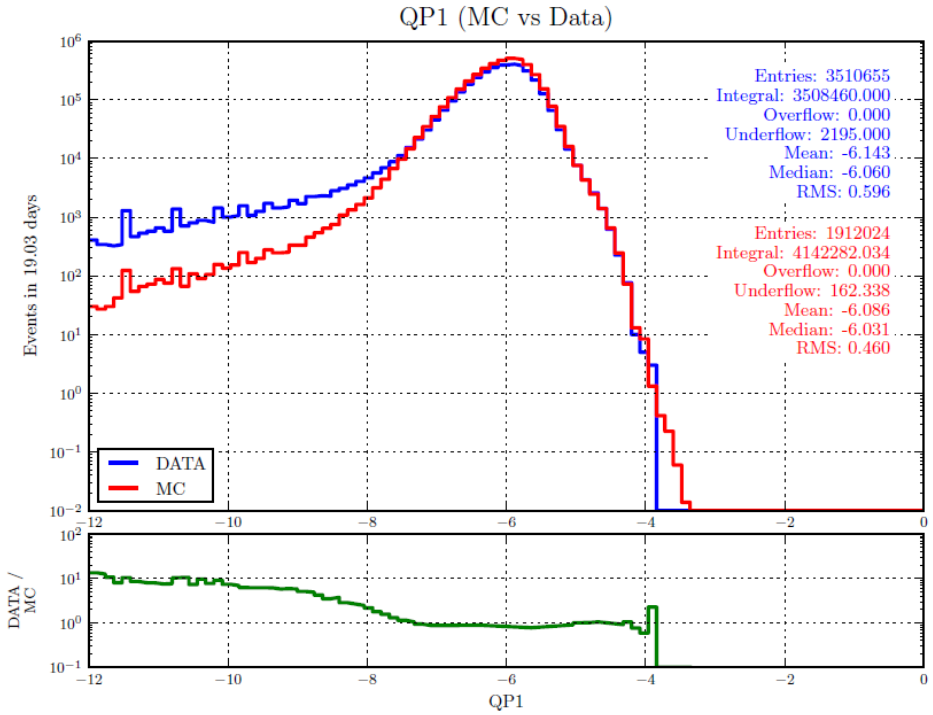

Figure 6.16: Data-Monte Carlo comparison - $QP1$ distribution.

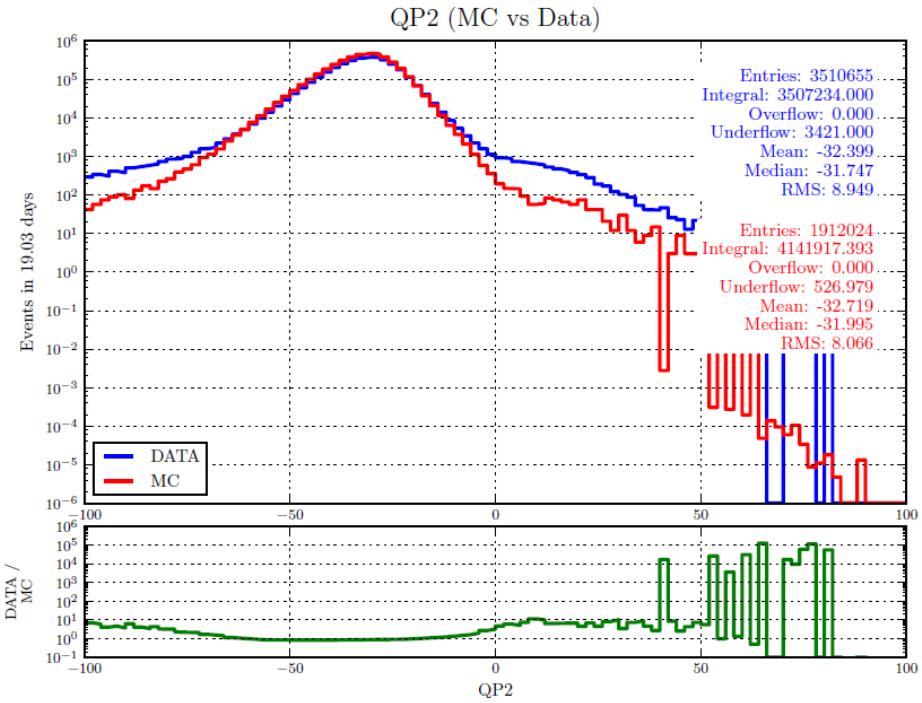

Figure 6.17: Data-Monte Carlo comparison - $QP2$ distribution.

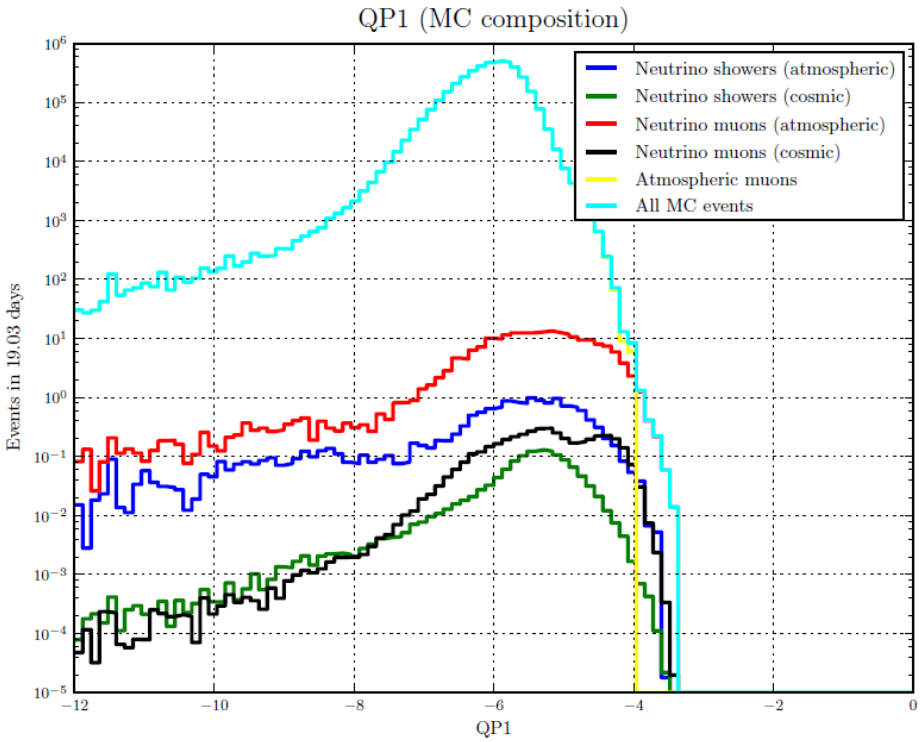

Figure 6.18: Data-Monte Carlo comparison - $QP1$ distribution, whole MC composition.

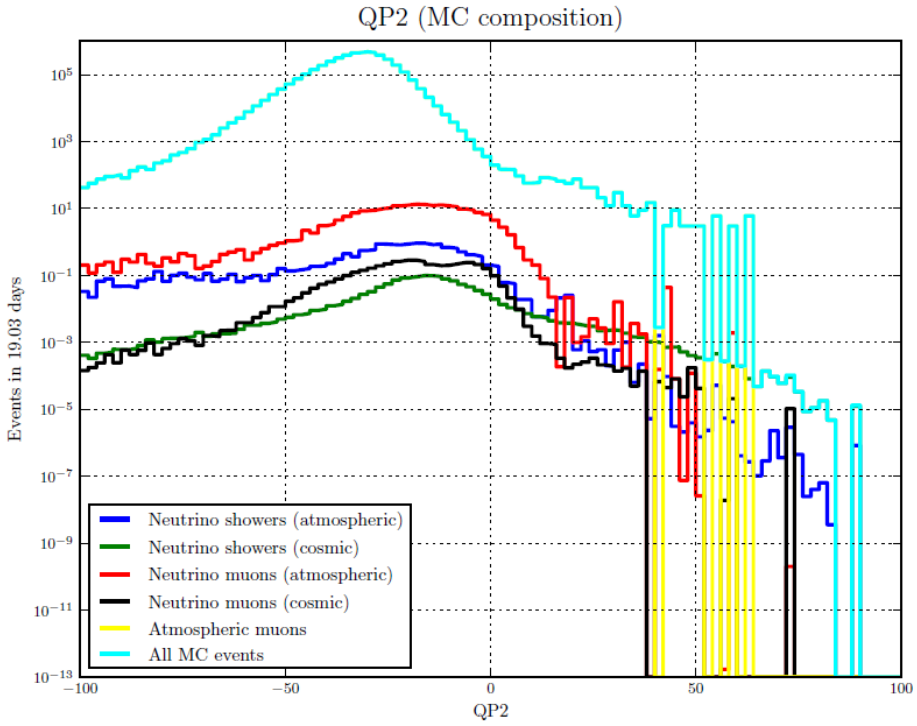

Figure 6.19: Data-Monte Carlo comparison - $QP2$ distribution, whole MC composition.

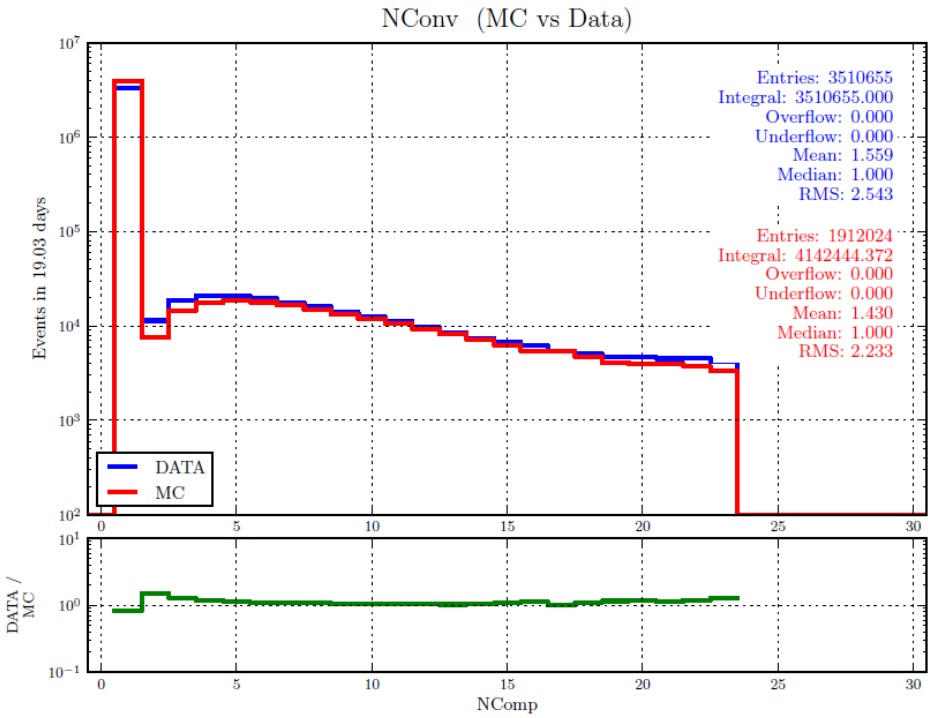

Figure 6.20: Data-Monte Carlo comparison - N_{conv} distribution.

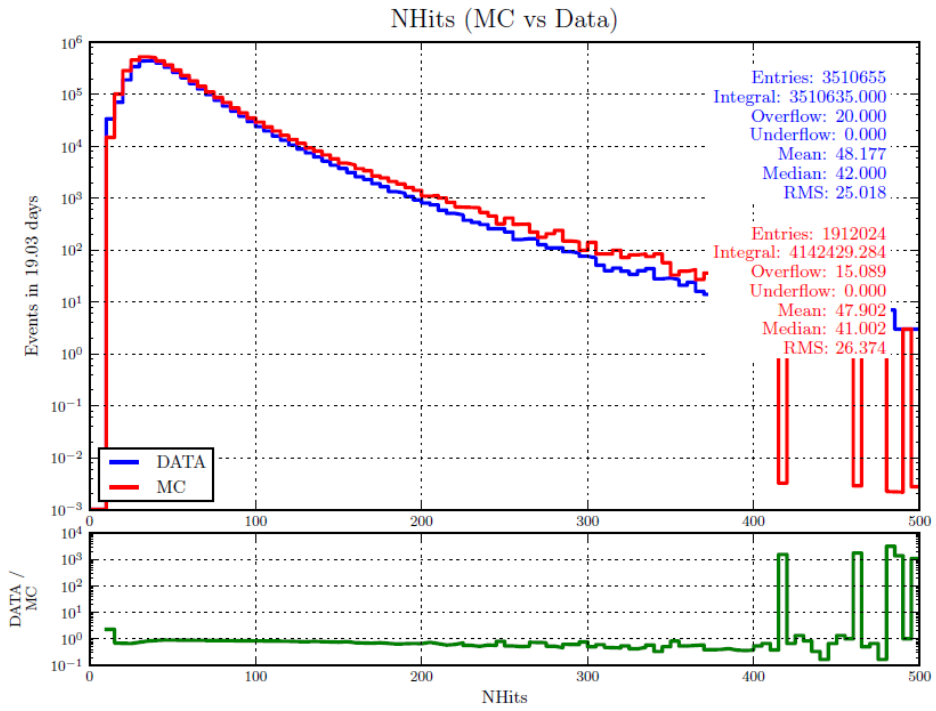

Figure 6.21: Data-Monte Carlo comparison - OSFFinalHits distribution.

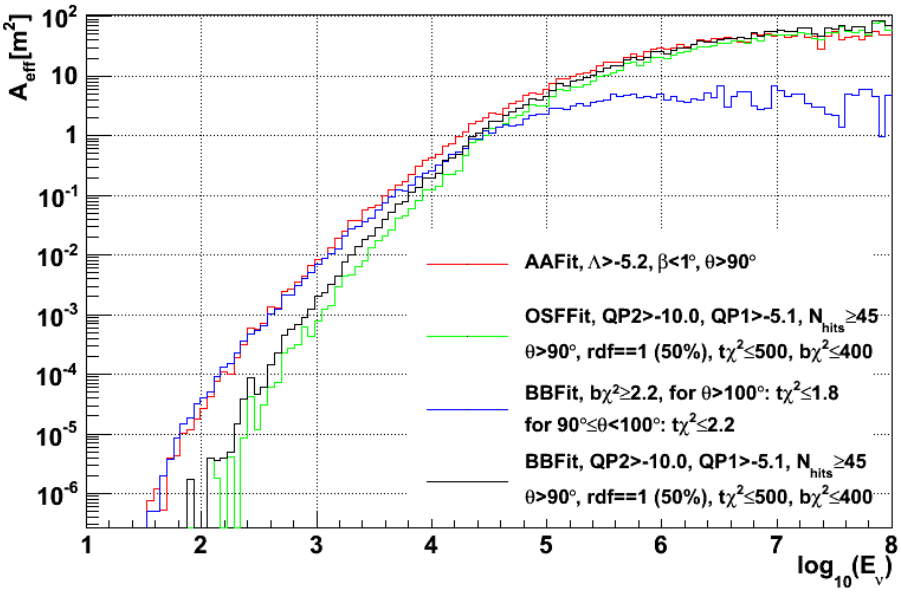

Figure 6.22: Effective areas of AAFit in red, OSFFit in green, BBFit and cuts that were opimized for a point source search with 2007 data [89] in blue and BBFit with the cuts of OSFFit in black.

Part III

Analysis

Chapter 7

Run and event selection

OSFFit, as an elaborate muon neutrino reconstruction strategy, was applied on 2007 and 2008 data. This dataset can be analysed without the necessity of an unblinding request (see Chapter 4.1). In this chapter, deeper insight into which runs and events were finally used and excluded and a quantitative listing of the influence of the contributing quality cuts is given. As in the previous chapter it was worked with the RBR v 2.2 and RBR v 2.0 Monte Carlo files and with $\Phi_{\text{ref}} = \Phi_0 \cdot E^{-2} = 1 \cdot 10^{-7} \cdot E^{-2} \cdot \text{GeV} \cdot \text{cm}^{-2} \cdot \text{sec}^{-1}$ as the flux assumption of cosmic neutrinos.

7.1 Run selection

The first run with five lines installed that was considered for this analysis was run 25682, which started on 28 January 2007. The last was run 38230 taken on 31 December 2008. During this two-year period, lines were connected successively to a fully operational detector with the exception of a short period of nine lines (regression from ten to nine lines) that was caused by communication problems between line four and the junction box. Table 7.1 gives an overview of the four data taking periods that were considered and their associated run numbers, dates and lifetimes. The total lifetime of the 3537 selected runs is $\approx$ 1.17 years. There were 723 runs with a lifetime of $\approx$ 0.16 years that were excluded from the analysis. These runs are assigned a *QualityBasic flag* = 0, a *SCAN flag* or a *sparking flag*. The *QualityBasic* classifies runs into five categories (0–5) based on their run duration, baseline rate, burst fraction and the amount of working OMs. The *sparking flag* is seldom assigned; it is related to events with a high hit multiplicity that is due to an immense charge release within an OM that turns this OM into a light source itself. Runs with test setups are marked with the *SCAN flag* and should generally not contribute to data analysis. These parameters were obtained from the ANTARES database; their meaning is described on the ANTARES homepage [59] in more detail. Figures 2.10 to 2.12 give an impression of the quantity of excluded runs.

Detector configuration	First run	Date of first run	Last run	Date of last run	Lifetime in years
Line 5	25682	27-1-2007	30460	4-12-2007	0.63
Line 10	30508	7-12-2007	32491	3-3-2008	0.15
Line 9	32525	3-3-2008	34417	27-5-2008	0.13
Line 12	34419	28-5-2008	38230	31-12-2008	0.27
in total	25682	27-1-2007	38230	31-12-2008	1.17

Table 7.1: Detector configurations and lifetimes during the data taking period from 2007 to 2008. The total lifetime of data analysed in this thesis is 1.17 years.

7.2 Event selection

Only events surviving the full OSFFit cut combination with $QP2 = -10$ that has been determined for the second test sample were selected for the following analysis (see last row of Table 6.2). The impact of the single cut components on the 2007 and 2008 data sample is summarised in Table 7.2. It lists the percentage of data, atmospheric neutrinos, atmospheric muons and cosmic neutrinos that survived diverse cuts related to their initial amount of 3N3T triggered events, respectively. $3N3T_{OSF}$ means triggered events that are additionally reconstructable by OSFFit. It can be seen that each cut strongly affects the initial event volume. The most effective rejection for the atmospheric muon background is given by the $QP2$ cuts. In analogy to Chapter 6.3, also here, the most profitable cut is the full OSFFit cut combination that is contained in the last row of Table 7.2. This cut keeps 14.97 % of cosmic neutrinos and only 2.15 % of atmospheric neutrinos in the selected 2007–2008 data sample. In both data samples, atmospheric muons are completely suppressed by these cuts.

cut	data	atm. ν	atm. μ	cosmic ν
no cut	$\approx 2.4 \cdot 10^8$	–	–	–
3N3T	$\approx 1.4 \cdot 10^8$ (100 %)	100 %	100 %	100 %
$3N3T_{OSF}$ (+ OSFFit finds)	30.29 %	34.87 %	63.59 %	76.72 %
$3N3T_{OSF} + \theta > 90°$	0.65 %	28.13 %	2.36 %	43.69 %
$3N3T_{OSF} + N_{hits} \geqq 45$	9.35 %	3.99 %	19.12 %	42.09 %
$3N3T_{OSF} + QP2 > -9.5$	0.26 %	10.75 %	0.21 %	32.47 %
$3N3T_{OSF} + QP2 > -10.5$	0.32 %	11.71 %	0.26 %	34.58 %
$3N3T_{OSF} + QP1 > -5.1$	0.55 %	14.74 %	0.76 %	40.95 %
$3N3T_{OSF}$ + rdf = 1	1.43 %	26.92 %	3.56 %	47.20 %
$3N3T_{OSF}$ + track $- \chi^2 \leqq 500$ + bright $- \chi^2 \leqq 400$	30.27 %	34.86 %	63.56 %	76.59 %
$3N3T_{OSF} + QP2 > -10.0 + \theta > 90° + N_{hits} \geqq 45$	$\ll 0.01$ %	2.20 %	0.01 %	16.18 %
$3N3T_{OSF} + QP2 > -10.0 + QP1 > -5.1 + \theta > 90° + N_{hits} \geqq 45$ + rdf = 1 + track $- \chi^2 \leqq 500$ + bright $- \chi^2 \leqq 400$	$\ll 0.01$ %	2.15 %	≈ 0.00 %	14.97 %

Table 7.2: Percentage of data, cosmic neutrinos, atmospheric neutrinos and atmospheric muons that survive diverse quality cuts and the 3N3T trigger concerning the 2007 and 2008 data sample. The full OSFFit cut combination is presented in the last row of this list.

Chapter 8

Detector performance

The main quantities used to classify the performance of a neutrino telescope concerning a special reconstruction algorithm are the angular resolution and the effective area or detector acceptance. If not stated otherwise, the full OSFFit cut combination with $QP2 = -10$ was applied.

8.1 Angular resolution

Figure 8.1 shows the angular resolutions of neutrinos, which are reconstructed by OSFFit with its final cut combination, whereby the contributing $QP2$ takes the values -10.5, -10.0 and -9.5 (for all declinations). The excess of events at angular errors of $\approx 84°$ has already been explained in Chapter 2.4.3 as the *ghost solution*. The distribution is drawn cumulatively in Figure 8.2. The medians of the angular resolutions are calculated as 1.22°, 1.23° and 1.25°, respectively. Thereby, $\approx 89\,\%$ of the events have an angular error $< 1°$.

8.2 Effective area

Effective areas are one possibility for presenting and comparing the performance of reconstruction chains, as they mirror the detector answer to the full simulation and reconstruction of events. They can be considered as the equivalent area of a hundert percent efficient detector. The effective areas for neutrinos A^{ν}_{eff} describe the reconstruction capability for a given flux, energy E_ν and zenith angle θ_ν of the neutrino within the effective volume V_{eff}. Thereby, possible interactions with nucleons (given by the neutrino cross-section per nucleon $\sigma(E_\nu)$), the nucleon density ρN_A and the probability of absorption in the Earth $P_{\text{Earth}}(E_\nu, \theta_\nu)$ are considered (see Equation 8.1). The rotation symmetry of Earth causes an independence of the azimuthal component from the neutrino direction. In this thesis A^{ν}_{eff} is calculated as described in [90]:

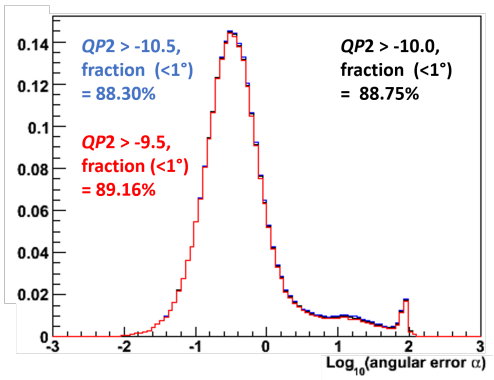

Figure 8.1: Histograms of the angular resolution for neutrinos reconstructed by OSFFit with its final cut combination, whereby $QP2 = $-10.5, -10 and -9.5. The second peak at 84° is produced by mis-reconstructed tracks (ghost solution). Approximately 89 % of events have an angular error $< 1°$.

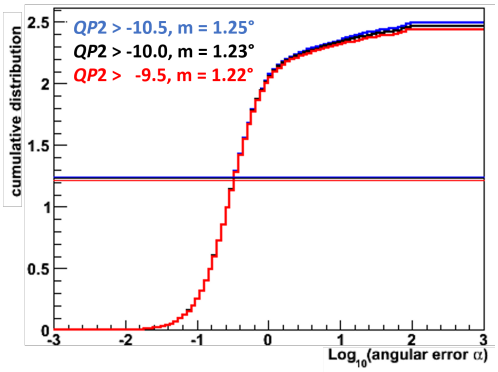

Figure 8.2: Cumulative visualisation of Figure 8.1. The excess of events due to the ghost solution is also recognisable here. The three distributions yield median angular errors of 1.22°, 1.23° and 1.25°.

$$A^{\nu}_{\text{eff}}(E_\nu, \theta_\nu) = V_{\text{eff}}(E_\nu, \theta_\nu) \cdot \rho N_A \cdot \sigma(E_\nu) \cdot P_{\text{Earth}}(E_\nu, \theta_\nu) \tag{8.1}$$

V_{eff} presents the effective volume which is defined as the number of events selected by the reconstruction algorithm divided by the number of all events generated within the generation volume V_{gen}. V_{gen} is chosen such that all detectable neutrino interactions are contained (see Figure 2.8).

$$V_{\text{eff}}(E_\nu, \theta_\nu) = \frac{N_{\text{selected}}}{N_{\text{gen}}} \cdot V_{\text{gen}} \tag{8.2}$$

The effective area of OSFFit is shown in Figure 8.1 for different declination bands.

8.3 Acceptance

The acceptance of the detector concerning a certain neutrino reconstruction algorithm $A^{\nu}_{\text{acc}}(\theta_\nu)$ represents another expression of the reconstruction performance. It describes the connection between the amount of neutrino events N_ν and their declination. It is evaluable as the amount of neutrino events integrated over the run duration and neutrino energy; this is shown in Equation 8.3 in terms of the effective area [8]. The term Φ_0 concerns to the cosmic neutrino flux.

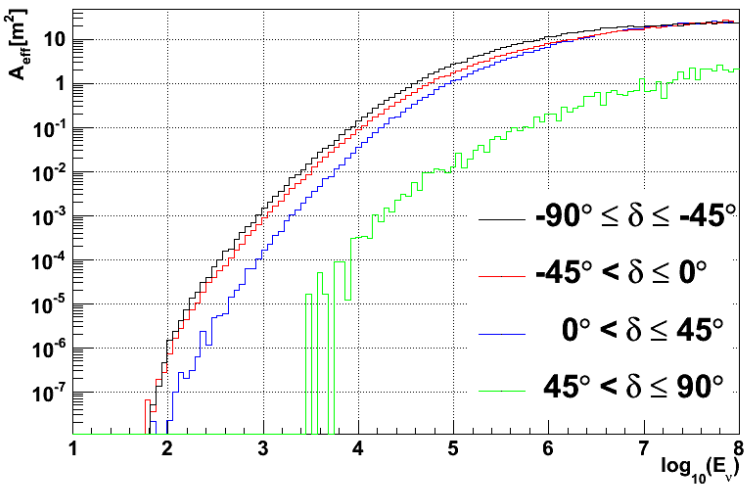

Figure 8.3: Effective area of neutrinos that are found by OSFFit with its final cut combination for four declination bands.

$$A^{\nu}_{\mathrm{acc}}(\theta_\nu) = \Phi_0^{-1} \int\int dt \cdot dE_\nu \cdot A^{\nu}_{\mathrm{eff}}(E_\nu, \theta_\nu) \cdot \frac{dN_\nu}{dE_\nu \cdot dt} \tag{8.3}$$

The acceptance is illustrated for the OSFFit final cut combination and a flux assumption of $\Phi_{\mathrm{ref}} = \Phi_0 \cdot E^{-2} = 1 \cdot 10^{-7} \cdot E^{-2} \cdot \mathrm{GeV} \cdot \mathrm{cm}^{-2} \cdot \mathrm{sec}^{-1}$ in Figure 8.4.

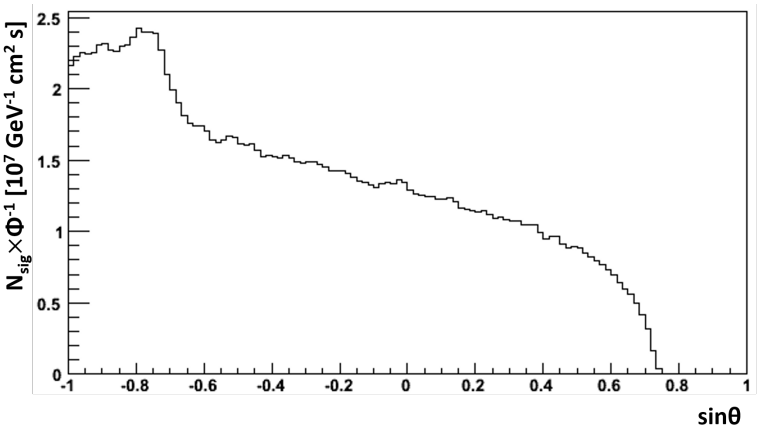

Figure 8.4: Acceptance $n_{\mathrm{ref}}/\Phi_{\mathrm{ref}}$ of the detector by applying OSFFit with its final cut set.

The expected number of signal events n_{ref} for a certain declination band and flux Φ_{ref} can be extracted from this kind of diagram. The values on the y-axis correspond to the number of detected events. Furthermore, such a diagram can be used to calculate limits of the flux Φ_{CL} for the confidence level (CL) of interest by applying Equation 8.4 with known n_{CL} (see Chapter 9.5.3). In this equation the acceptance is given as the expression $n_{\mathrm{ref}}/\Phi_{\mathrm{ref}}$ and represents the constant of proportionality.

$$\Phi_{\mathrm{CL}} = \Phi_{\mathrm{ref}} \cdot \frac{n_{\mathrm{CL}}}{n_{\mathrm{ref}}} \tag{8.4}$$

Chapter 9

Search method

An unbinned maximum likelihood method was used to seek point sources of neutrinos. The signature of a point source is described by a narrow cluster of signal events around the source coordinates over a flat distribution of pure background events. For the following analysis a cluster size of 20° opening angle has been chosen to cover a reasonable amount of events. Information on the p-value, upper limits on the event numbers and the flux in cases where no discovery is made can be extracted from statistical evaluations of the most likely event cluster. The signal hypothesis was tested for 24 known pre-defined high-energy γ-ray sources, which are assumed to emit neutrinos [37]. They include supernova remnants, microquasars and BL Lac objects. A BL Lac object is a type of an active galaxy with an AGN in its core. The potential candidate sources and their equatorial coordinates are listed in Table 9.1; they are mapped using the Hammer-Aitoff equal-area projection as the blue points in Figure 9.1 [91].

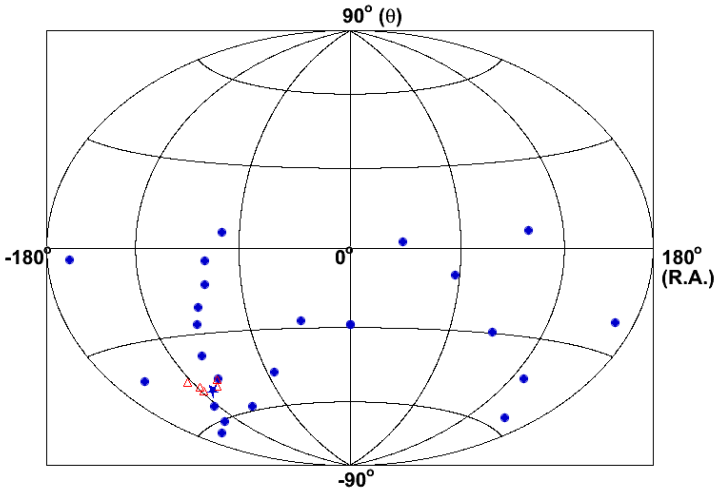

Figure 9.1: Skymap in equatorial coordinates. Nearly all of the 24 potential neutrino source candidates are located in the Southern Hemisphere (blue points). The red triangles belong to source number 7; their meaning is described at the end of this chapter.

In this chapter all calculations and plots are exemplified for source number 7 (HESS J1614-518) and $QP2 = -6$ as part of the full OSFFit cut combination. Among all of the 24 sources and possible cuts the mentioned ones were chosen as they turned out to be the most promising combination for neutrino detection. In Chapter 10 final plots are shown that refer to all of the 24 candidates. Source 7 has a small declination coordinate; for comparison reasons plots for sources 14 and 16 that are located at middle and high declinations are added in Appendix E.

Source number	Source name	RA [°]	θ [°]	l	b
1	HESS J0632+057	98.2417	5.80556	205.66	-1.4
2	RX J0852.0-4622	133.000	-46.3667	266.28	-1.2
3	HESS J1023-575	155.825	-57.7639	284.19	-0.3
4	PSR B1259-63	195.704	-63.8339	304.19	-0.9
5	RCW 86	220.679	-62.4833	315.79	-1.4
6	Cir X-1	230.171	-57.1667	322.12	0.04
7	HESS J1614-518	243.579	-51.82	331.52	0.58
8	GX 339	255.704	-48.7897	338.94	-4.3
9	RX J1713.7-3946	258.25	-39.75	347.28	-0.3
10	Galactic Center	266.421	-29.0061	359.95	-0.0
11	W28	270.425	-23.335	6.66	-0.2
12	LS 5039	276.562	-14.825	16.90	-1.2
13	HESS J1837-069	279.408	-6.95	25.18	-0.1
14	SS 433	287.958	4.98278	39.69	-2.2
15	RGB J0152+017	28.1667	1.78861	152.38	-26.
16	1ES 0347-121	7.3458	-11.9908	201.93	-45.
17	PKS 0548-322	87.6692	-32.2712	237.56	-26.
18	1ES 1101-232	165.908	-23.4919	273.19	33.0
19	3C 279	194.046	-5.78917	305.10	57.0
20	Centaurus A	201.365	-43.0191	309.52	19.4
21	ESO 139-G12	264.415	-59.9414	334.04	-13.
22	PKS 2005-489	302.371	-48.8219	350.39	-32.
23	PKS 2155-304	329.721	-30.2217	17.74	-52.
24	H 2356-309	359.783	-30.6275	12.84	-78.

Table 9.1: List of candidate source names and coordinates that were searched for in this thesis. The expression RA stands for the right ascension; θ means the declination; l and b mean the Galactic longitude and latitude. Most of the plots that are shown in this chapter refer to source number 7, which is highlighted in yellow.

9.1 Maximum likelihood ratio method

The maximum likelihood ratio method helps to distinguish signal from background-like events by searching for a statistical excess of events in a cluster around the hypothetical source position. The background is thereby thought to consist of only atmospheric neutrinos (see Table 7.2). The logarithmic likelihood of finding μ_{sig} signal and $N - \mu_{\text{sig}}$ background events in a cluster with N assumed and independent events is calculated via:

$$\log_{10}(\mathfrak{L}_{S+B}(\mu_{\text{sig}})) = \sum_{\text{event } i=1}^{N} \Big(\frac{\mu_{\text{sig}}}{N} S_i + (1 - \frac{\mu_{\text{sig}}}{N}) B_i \Big) \tag{9.1}$$

S stands for the signal probability density function (*signal PDF*) and B for the background probability density function (*background PDF*). Both probabilities have to be normalised to 1 in the standard scenario [92], which is applied here. The most likely number of neutrino events is defined as $\mu_{\text{sig}}^{\text{max}}$, which maximises Equation 9.1; this expression will be abbreviated with $\log_{10}\mathfrak{L}_{\mu_{\text{sig}}}^{\text{max}}$. The logarithmic likelihood for the background-only case is given by Equation 9.1 setting $\mu_{\text{sig}} = 0$; this term will be shortened with $\log_{10}\mathfrak{L}_{(\mu_{\text{sig}}=0)}$.

9.2 Hypothesis testing

A qualitative separation between signal and background can be pointed out with the likelihood ratio test statistic Q:

$$Q = \log_{10}\mathfrak{L}_{\mu_{\text{sig}}}^{\text{max}} - \log_{10}\mathfrak{L}_{(\mu_{\text{sig}}=0)} \tag{9.2}$$

The two expressions stand for the two test hypotheses H_0 and H_1, respectively. The hypothesis H_1 includes background and signal events. H_0 is called the *null hypothesis* and assumes that all events are due to background ($\mu_{\text{sig}} = 0$) [93]. The monotonic function $\log_{10}$ causes a steeper and more robust distribution of the test statistic Q than a simple log dependency which is used in [92]. High Q values indicate a higher compatibility with the signal hypothesis.

9.3 Signal PDF

The distribution of signal events S follows the point spread function (PSF). The PSF describes the response of an imaging system to a point object (such as a neutrino source). One illustration possibility of the PSF is realised in Figure 9.2 concerning a horizontal coordinate system. On its y-axis the difference in the zenith angle $\Delta\theta$ between reconstructed and simulated neutrino direction is plotted. The term $\sin\theta$ that is multiplied to the azimuthal angular error $\Delta\phi$ on the x-axis compensates for the initial elliptical appearance of the PSF. The coloured scale shows the tendency of its filling; the highest entry density belongs to the areas that are marked in red.

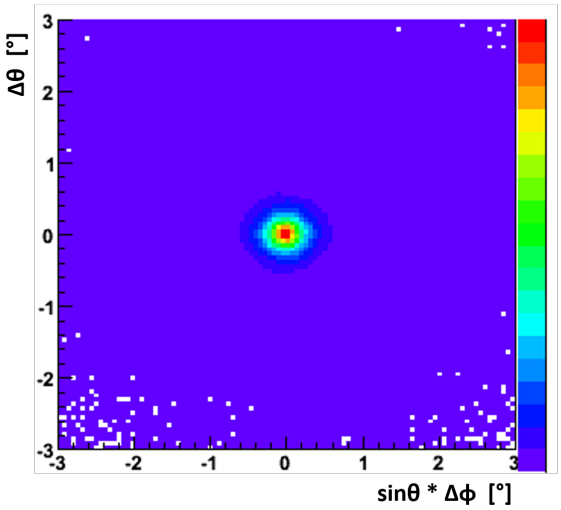

Figure 9.2: Visualisation of the PSF for the 2007–2008 data sample and the full OSFFit cut combination with $QP2 = -10$. The term $\Delta\theta$ corresponds to the difference in the zenith angle between the reconstructed and the simulated neutrino direction. The term $\Delta\phi$ accordingly means the difference in the azimuthal angle. The z-axis highlights the content density of the histogram; red regions contain the most events.

For working with such a profile of signal events, the following points have been taken into consideration. As the PSF is assumed to be axial symmetrical (see Figure 9.2), it was first decided to reduce this structure to its basic one-dimensional form. The resulting distribution $S = dN/d\omega$ is unnormalised visualised in Figure 9.3. Its production process will be described in the following sections.

The PSF can likewise be defined as the probability density of reconstructing an event with a certain angular distance ω from the true source coordinates. Hence, the PSF is closely related to the angular error α in the local system, which is defined as the angular distance of a reconstructed event to the simulated Monte Carlo muon neutrino event (see, for instance, Figure 8.1). A few arithmetic steps can be performed to transform the angular error histogram $dN/d\alpha$ into the PSF histogram $S = dN/d\omega$ [94]; they will be discussed in the following sections.

With the double integral over the unit surface element in spherical coordinates as the starting point, the solid angle ω of a cone with apex angle $2\,\alpha$ is calculable as follows:

$$\begin{aligned} \omega = \int\int \sin\alpha \cdot d\alpha \cdot d\phi &= 2\pi \cdot \int \sin\alpha \cdot d\alpha = 2\pi \cdot [-\cos\alpha]_0^\alpha = 2\pi \cdot (1 - \cos\alpha) \\ \Rightarrow \frac{d\omega}{d\alpha} &= 2\pi \cdot \sin\alpha \\ \Rightarrow \frac{d\alpha}{d\omega} &= \frac{1}{2\pi \cdot \sin\alpha} \end{aligned} \tag{9.3}$$

The last term of Equation 9.3 modifies $dN/d\omega$ to:

$$\begin{aligned} \frac{dN}{d\omega} &= \frac{dN}{d\alpha} \cdot \frac{d\alpha}{d\omega} \\ \Rightarrow \frac{dN}{d\omega} &= \frac{dN}{d\alpha} \cdot \frac{1}{2\pi \cdot \sin\alpha} \end{aligned} \tag{9.4}$$

For the integration over $\sin\alpha$ in a histogram, the conversion provided by Equation 9.5 has to be considered. Thereby, the indices i_{down} and i_{up} stand for the borders of each bin i of the initial histogram. For the creation of the histogram $dN/d\omega$, each bin j of $dN/d\alpha$ has to be divided by the expression of Equation 9.5. The distinction between $d\omega$ and $d\alpha$ is insignificantly small in the first approximation; therefore, the quantities were treated as equal in the final histograms (Figures 9.3 and 9.4).

$$\int_{i_{\text{down}}}^{i_{\text{up}}} 2\pi \cdot \sin(\alpha) \cdot d\alpha = 2\pi \cdot [\cos(i_{\text{down}}) - \cos(i_{\text{up}})] \tag{9.5}$$

But before this was done, the histogram $dN/d\alpha$ had been extracted from a two-dimensional histogram of the reconstructed declination over the angular error (of the 2007–2008 data sample). For each final OSFFit cut combination, such a two-dimensional histogram had been established; whereby $QP2$, incorporated in the mentioned cut set, was varied in the range from -20.0 to -5.0 in steps of 1.0 and 0.1. Within such a histogram, the slices of $\pm\,2.5^\circ$ around the source declination of interest have been unified to only one slice at this declination value.

In Figure 9.4 the contour of the PSF from Figure 9.3 is smoothed and overlaid by a spline function [1] (in red); for solid angles $\omega \leqq 0.1^\circ$ values are averaged and the excess at $\approx 84^\circ$ is removed. The reasons for the smoothing step are explained in Chapter 9.5. The purple shaded areas in Figures 9.3 and 9.4 mark the angular error range for $\omega \leqq 10^\circ$, which is related to the $\pm 10^\circ$ declination band around the potential neutrino source (here for candidate 7).

For the calculation of the likelihood of the events (see Chapter 9.5.2), probabilities are taken from such a PSF slice, which is plotted over the angular error. The values have to be multiplied by a factor $4\,\pi$ to restore the rotational symmetry and divided by the enclosed integral (number of events N) for a correct normalisation. This procedure has been performed for each source. The consistency of Equation 9.4 concerning the correct integral N_{SG} (normalization) is demonstrated in Equation 9.6.

$$
\begin{aligned}
N_{SG} &= \int S \cdot d\Omega \\
&= \int \frac{dN}{d\omega} \cdot d\Omega = \int \left(\frac{dN}{d\alpha} \cdot \frac{d\alpha}{d\Omega} \right) \cdot d\Omega \\
&= \int \left(\frac{dN}{d\alpha} \cdot \frac{1}{2\pi \cdot \sin\alpha} \right) \cdot d\Omega \\
&= \int \left(\frac{dN}{d\alpha} \cdot \frac{1}{2\pi \cdot \sin\alpha} \right) \cdot \sin\alpha \cdot \, d\alpha \cdot \int d\phi \\
&= \int \left(\frac{dN}{d\alpha} \cdot \frac{1}{2\pi} \right) \cdot \, d\alpha \cdot \int d\phi \\
&= \int \left(\frac{dN}{d\alpha} \cdot \frac{2\pi}{2\pi} \right) \cdot d\alpha \\
\Rightarrow N_{SG} &= N
\end{aligned}
\tag{9.6}
$$

[1] A spline is a numerical function that is defined piecewise by polynomial functions; one of their properties is their high differentiability at the points where the polynomial pieces are connected.

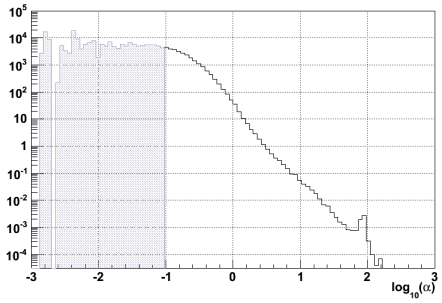

Figure 9.3: Transformation of the angular error histogram $dN/d\alpha$ into the histogram of the PSF $dN/d\omega$ for a 20° cone around the source coordinates of source number 7 (see Table 9.1) with applied full OSFFit cut set with $QP2 = $-6. The fluctuations on the left side of the distribution are due to only little statistics. The excess on the right side occurs at the ghost resolution.

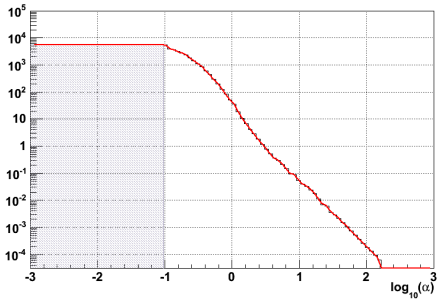

Figure 9.4: To ensure physically correct behaviour in the calculation of the likelihood values (see Chapter 9.5), the PSF is averaged for angular errors $\omega \leqq 0.1°$ and the excess at 84° is disposed of.

9.4 Background PDF

A consequence of the rotational movement of the Earth is the uniformly distributed right ascension ϕ of incidenting events. The location of the ANTARES detector on Earth causes a partial visibility concerning the declination θ of the detected sources. This is described by a descending distribution (see Figure 8.4). In Figure 9.5 the distribution of measured data events is drawn over $\sin\theta$. This histogram was produced in such a way that its integral is scaled to the real number of measured events N_{obs} that survived the OSFFit cut combination with $QP2 = -6$. Again, as is was done for the signal PDF S, histograms with $QP2$ ranging from -20.0 to -5.0 were produced.

In Figure 9.6 the data histogram is overlaid by a polynomial of fourth power (the blue curve). Here, the shaded areas correspond to the $\pm 10°$ declination bands around source number 7 for which $\sin\theta \approx -0.79$ (see Table 9.1). The number of background events N is set to the content of the blue interval enclosed by the polynomial fit. It would also be possible to get an estimation of the background from evaluations using Monte Carlo files (see Table B.1). However, as it was assumed that this would yield a similar uncertainty as the method described above, it was decided in favour of the latter.

As was done for the signal PDF S, also the background PDF B needs to be related to the space angle Ω. For this step another approach was chosen than for S, which is shown in Equation 9.7. It can be deduced that each probability value taken from $B(\theta, \phi) = B(\theta) = dN/d\sin\theta$ has to be divided by 4π and the number of events enclosed by the blue band N. These values are used in the calculation of the likelihood (see Chapter 9.5.2).

$$\begin{aligned} \int d\Omega &= \underbrace{\int d\phi}_{=2\pi} \cdot \underbrace{\int B(\theta)}_{=2} = 4\pi \\ \Rightarrow \int B(\theta) \cdot d\Omega &= 4\pi \cdot N \\ \Rightarrow N_{BG} &= 4\pi \cdot N \end{aligned} \tag{9.7}$$

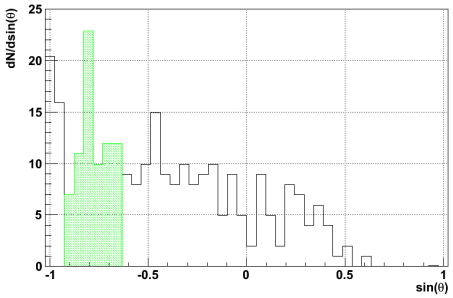

Figure 9.5: Background probability density function $dN/d\sin\theta$. The shaded region is assigned to the search cone around source 7.

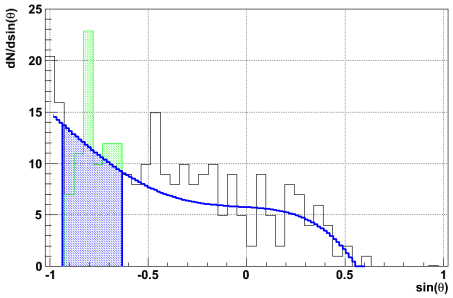

Figure 9.6: The background probability density function $dN/d\sin\theta$ is overlaid by a polynomial of fourth power (in blue). The measured number of events is related to the green dyed area; the number of background events is given by the integral over the blue dyed construct (polynomial function of fourth power).

9.5 Pseudo experiments

The pseudo experiments applied here mirror the scenario of detecting signal and background events from different points in the sky. In the context of a candidate list search these points correspond to the candidate coordinates. Associated pseudo events are generated with the help of the signal and background profiles described above. These events are put in a 20° cone around the particular source position. Vectors are created that are filled with these events. The exact procedure will be explained in the next section in more detail. Pseudo experiments have been repeated 10^7 times for the background-only case (H_0 hypothesis) and 10^5 times for a vector that additionally contains signal events (H_1 hypothesis). With this numbers a significance of $5\,\sigma$ was reachable. In this manner statistical statements about limits, fluxes and so on can be derived.

9.5.1 Creation of an event vector

The signal n_s and background events n_b around the source are stored in a particle vector that is filled with the angular error, the declination and the RA of each event. n_s and n_b are extracted from the one-dimensional histograms introduced above. The following steps are performed for source number 7 ($\sin\theta \approx -0.79$).

First, the background fraction will be focused on. The corresponding declination coordinate of an event θ is randomly taken from the solid blue region of Figure 9.6; thereby, the frequency of declination value selected is correlated with the content of the bins (see the ROOT website [95]). As a result of the one-dimensional drawing of the events, the information of the associated RA ϕ and angular error α are lost and have to be evaluated.

Since the RA of the background events is assumed to be constantly distributed over the sky, this value is randomly and uniformly chosen within the admitted range of $4\,\pi$. The angular difference α to the source was calculated as provided by Equation 9.8 [96]. Here, the vectors $\vec{r}_\mathrm{src}$ and $\vec{r}_\mathrm{rec}$ stand for a particle path that directly points to the source and a reconstructed muon path within the mentioned cone, respectively. The same is valid for all other quantities that carry these indices. The coordinates of declination and RA are abbreviated with θ and ϕ. A particle vector that is filled with only background events is used to calculate the H_0 hypothesis. This will be explained in Chapter 9.5.2.

$$\begin{aligned}
\cos(\alpha) &= \vec{r}_\mathrm{src} \cdot \vec{r}_\mathrm{rec} \\
&= \cos(\theta_\mathrm{src}) \cdot \cos(\theta_\mathrm{rec}) \cdot (\sin(\phi_\mathrm{src}) \cdot \sin(\phi_\mathrm{rec}) + \\
&\qquad + \cos(\phi_\mathrm{src}) \cdot \cos(\phi_\mathrm{rec})) + \sin(\theta_\mathrm{src}) \cdot \sin(\theta_\mathrm{rec}) \\
&= \cos(\theta_\mathrm{src}) \cdot \cos(\theta_\mathrm{rec}) \cdot \cos(\phi_\mathrm{src} - \phi_\mathrm{rec}) + \sin(\theta_\mathrm{src}) \cdot \sin(\theta_\mathrm{rec}) \\
\Rightarrow \alpha &= \arccos(\cos(\theta_\mathrm{src}) \cdot \cos(\theta_\mathrm{rec}) \cdot \cos(\phi_\mathrm{src} - \phi_\mathrm{rec}) + \sin(\theta_\mathrm{src}) \cdot \sin(\theta_\mathrm{rec}))
\end{aligned} \tag{9.8}$$

The second step is the establishing of nine further vectors that consist of the initial background vector plus particularly one to only nine signal events; more events are not assumed to be detectable by OSFFit and the associated cuts. The signal events are randomly extracted from the corresponding PSF distribution; also here, their selection is correlated with the content of the bins. In Figure 9.3 the PSF distribution of source 7 is shown.

Associated declination and RA of the signal events have to be gathered from the angular error. Therefore, a three-dimensional rotation into another spherical coordinate system was performed to keep the angular error and assign new declination and RA. It was followed similar ideas that are presented in [3]. First, an initial vector $\vec{v}_{\text{ini}}$ is created depending on the angular error α and the initial RA coordinate of the source ϕ_{src} (see Equation 9.9). Then, $\vec{v}_{\text{ini}}$ is turned $\frac{\pi}{2} - \theta_{\text{src}}$ around the y-axis (see Equation 9.10) and the angular error α around the z-axis (see Equation 9.11) [97]. The new coordinates of the declination, θ_{new}, and the RA, ϕ_{new}, are then given as shown by Equations 9.12 and 9.13; these values have still the initial angular distance α from the source candidate.

$$\vec{v}_{\text{ini}} = \begin{pmatrix} v_x \\ v_y \\ v_z \end{pmatrix} = \begin{pmatrix} \sin(\alpha) \cdot \cos(\phi_{\text{src}}) \\ \sin(\alpha) \cdot \sin(\phi_{\text{src}}) \\ \cos(\alpha) \end{pmatrix} \tag{9.9}$$

$$\vec{w}_{\text{rot}\,\vec{y}} = \begin{pmatrix} w_x \\ w_y \\ w_z \end{pmatrix} = \begin{pmatrix} v_x \cdot \cos(\frac{\pi}{2} - \theta_{\text{src}}) + v_z \cdot \sin(\frac{\pi}{2} - \theta_{\text{src}}) \\ v_y \\ v_z \cdot \cos(\frac{\pi}{2} - \theta_{\text{src}}) - v_x \cdot \sin(\frac{\pi}{2} - \theta_{\text{src}}) \end{pmatrix} \tag{9.10}$$

$$\vec{u}_{\text{rot}\,\vec{z}} = \begin{pmatrix} u_x \\ u_y \\ u_z \end{pmatrix} = \begin{pmatrix} w_x \cdot \cos(\phi_{\text{src}}) - w_y \cdot \sin(\phi_{\text{src}}) \\ w_x \cdot \sin(\phi_{\text{src}}) + w_y \cdot \cos(\phi_{\text{src}}) \\ w_z \end{pmatrix} \tag{9.11}$$

$$\begin{aligned} \theta_{\text{new}} &= u_z \\ \Rightarrow \theta_{\text{new}} &= \arcsin(\cos(\alpha) \cdot \cos(\tfrac{\pi}{2} - \theta_{\text{src}}) - \sin(\alpha) \cdot \cos(\phi_{\text{src}}) \cdot \sin(\tfrac{\pi}{2} - \theta_{\text{src}})) \end{aligned} \tag{9.12}$$

$$\begin{aligned} \phi_{\text{new}} &= \text{atan2}(u_y, u_x) \\ \Rightarrow \phi_{\text{new}} &= \text{atan2}(\ (\sin(\alpha) \cdot \cos(\phi_{\text{src}}) \cdot \cos(\tfrac{\pi}{2} - \theta_{\text{src}}) + \cos(\alpha) \cdot \sin(\tfrac{\pi}{2} - \theta_{\text{src}})) \cdot \\ &\qquad \sin(\phi_{\text{src}}) + \sin(\alpha) \cdot \sin(\phi_{\text{src}}) \cdot \cos(\phi_{\text{src}}), \\ &\qquad (\ \sin(\alpha) \cdot \cos(\phi_{\text{src}}) \cdot \cos(\tfrac{\pi}{2} - \theta_{\text{src}}) + \cos(\alpha) \cdot \sin(\tfrac{\pi}{2} - \theta_{\text{src}})) \cdot \\ &\qquad \cos(\phi_{\text{src}}) - \sin(\alpha) \cdot \sin^2(\phi_{\text{src}})\ ) \end{aligned} \tag{9.13}$$

Finally, the number of measured events N_{obs} for the particular source, which is assumed to consist of signal and background events together, was set to the unaffected green shaded interval shown in Figure 9.5.

9.5.2 Calculation of the likelihood

It has to be determined which of the ten event clusters described above is the most likely one. For each of them, Equation 9.1 was tried to optimize by the variation of μ_{sig} from zero to an upper border of twelve in steps of 0.05. Insertion of the optimised value $\mu_{\mathrm{sig}}^{\mathrm{max}}$ into Equation 9.2 yields the test statistic Q; the distributions of $\mu_{\mathrm{sig}}^{\mathrm{max}}$ and Q are plotted in Figures 9.7 and 9.8, respectively. Figure 9.9 contains the connection (Q values versus varied μ_{sig}).

For the first vector that consists of a pure background sample this procedure was repeated 10^7 times. As the data events are assumed to occur independently of each other, they follow a Poisson distribution $\mathcal{P}(\, N_{\mathrm{obs}} \,|\, n_{\mathrm{b}} \,)$ with n_{b} as the expectation value and N_{obs} as the variable quantity, see Equation 9.14. Comparable results were obtained if the vector size n_{b} was kept constant.

$$\mathcal{P}(\, N_{\mathrm{obs}} \,|\, n_{\mathrm{b}} \,) \;=\; \frac{n_{\mathrm{b}}^{N_{\mathrm{obs}}}}{N_{\mathrm{obs}}!} \cdot e^{-n_{\mathrm{b}}} \tag{9.14}$$

The mixed vector underwent the calculation only 10^5 times. For the calculations, the contours of the spline function and the polynomial fit mentioned above acted as S and B, respectively, to ensure continuous deviation behaviour over the whole angular error and declination range. Furthermore, the steady curves mirror more realistic conditions than the rough histograms. To normalise the PDFs to 1, they were divided by the corresponding integrals. For the normalisation to the whole solid angle 4π, the probabilities of S are multiplied with 4π and those of B are divided by 4π (as was described in Chapters 9.3 and 9.4).

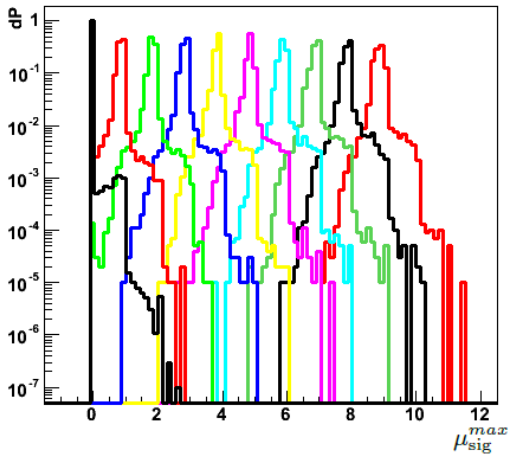

Figure 9.7: Distribution of $\mu_{\text{sig}}^{\text{max}}$ that maximise Equation 9.1 for a variation of μ_{sig} from zero to nine inserted signal events in steps of 0.05.

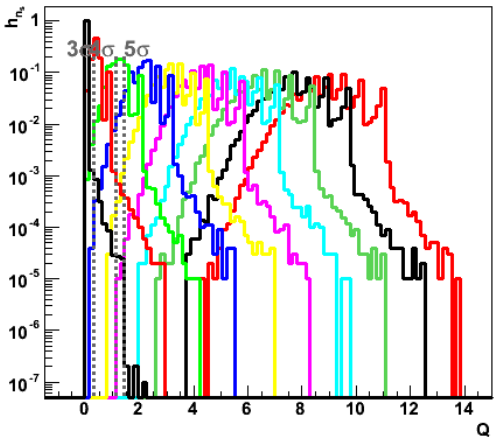

Figure 9.8: Distribution of the optimised test statistic Q that corresponds to Figure 9.7. The 3σ, 4σ and 5σ limits are highlighted with grey dashed lines.

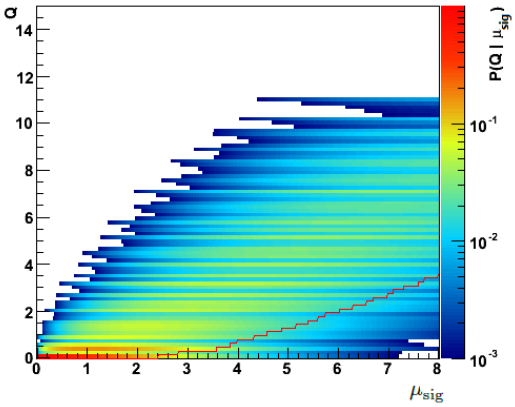

Figure 9.9: Two-dimensional histogram of Q versus μ_{sig}. The red line confines the ten-percent range; the point on the μ_{sig}-axis where the curve starts to rise over $Q = 0$ is utilised in a test calculation of the upper limit with a confidence interval of 90 % (see Chapter 9.5.3).

9.5.3 Calculation of discovery potential and median upper limit

In the following section statistical calculations that were applied on the 24 candidates listed in Table 9.1 will be described and exemplified for source number 7. Since an excess of events was not found for any of the sources, limits were set up.
The *model discovery potential (MDP)* was used to evaluate the averaged number of expected signal events $\langle n_{\mathrm{CL}} \rangle$ that yields a discovery for the confidence levels (CLs) of 3σ, 4σ and 5σ with 50 % probability ($MDP(\,\mu_{\mathrm{sig}}\,) = 0.5$). The MDP ranges from zero to one, see Equation 9.15 and Figure 9.10. A CL $= 3\sigma$ is associated with evidence of the existence of a source candidate and CL $= 5\sigma$ with the discovery of a neutrino source.

$$\begin{aligned} MDP(\,\mu_{\mathrm{sig}}\,) &= P(\,Q \geqq Q_{\mathrm{CL}}^{\mathrm{thresh}} \,|\, n_{\mathrm{s}}\,) \\ &= \int_{Q_{\mathrm{CL}}^{\mathrm{thresh}}}^{\infty} P(\,Q \,|\, n_{\mathrm{s}}\,) \cdot dQ \\ &= \sum_{n_{\mathrm{s}}=0}^{\infty} \mathcal{P}(\,n_{\mathrm{s}} \,|\, \mu_{\mathrm{sig}}\,) \cdot \int_{Q_{\mathrm{CL}}^{\mathrm{thresh}}}^{\infty} h_{n_{\mathrm{s}}}(Q) \cdot dQ \end{aligned} \tag{9.15}$$

The test statistic Q has already been introduced in Chapter 9.2; $Q_{\mathrm{CL}}^{\mathrm{thresh}}$ is the lower limit of the integral that reaches up to ∞; $\mathcal{P}(\,n_{\mathrm{s}} \,|\, \mu_{\mathrm{sig}}\,)$ means the Poisson distribution with expectation value μ_{sig} and n_{s} as variable quantity with 12 as its maximal value; $h_{n_{\mathrm{s}}}(Q)$ denotes the distribution of the Q values for n_{s} assumed signal events and background events n_{b} that follow a Poisson distribution itself; $h_{n_{\mathrm{s}}}(Q)$ is plotted in Figure 9.8.

The so-called p-value describes the probability to obtain a test statistic Q that is at least as extreme as the one observed if the background-only case is true (see Equation 9.16). It is computed as the integral over the particular $Q_{\mathrm{CL}}^{\mathrm{thresh}}$ up to ∞; n_{b} is the expectation value of the number of background events.

$$p\text{-value} = P(\,Q \geqq Q_{\mathrm{CL}}^{\mathrm{thresh}} \,|\, n_{\mathrm{b}}\,) = \int_{Q_{\mathrm{CL}}^{\mathrm{thresh}}}^{\infty} h_{n_{\mathrm{s}}=0}(Q) \cdot dQ \tag{9.16}$$

The 90 % upper limit was set on the number of signals μ_{sig}. All values above this value are rejected for more than 90 % of the pseudo experiments. For the following discus-

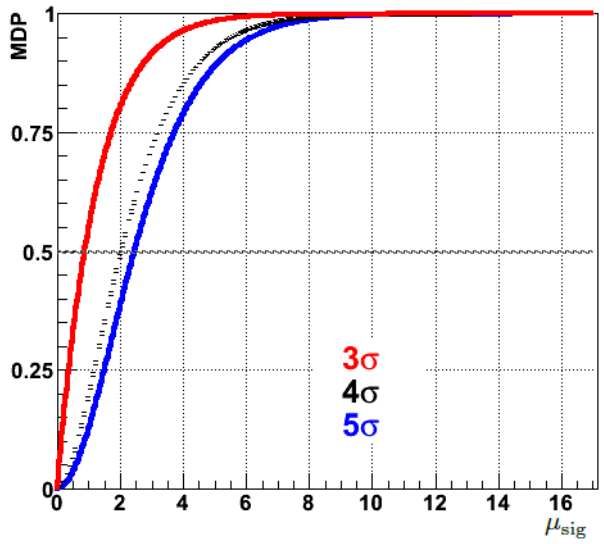

Figure 9.10: MDP over the number of estimated signal events μ_{sig} for the confidence intervals $3\,\sigma$, $4\,\sigma$ and $5\,\sigma$ for source 7 and $QP2 = -6.0$.

sions $n^{up}_{90\%}$ means the median number of signal events that can be excluded at a 90% CL. The limit setting procedure will be exemplified for candidate 7 and $QP2 = -6.0$ on Monte Carlo data:

Therefore, a median Q-value was extracted from the first bin of the two-dimensional histogram in Figure 9.9. This bin corresponds to the hypothetical case $\mu_{sig} = 0$. The median 90% upper limit on the signal events, $n^{up}_{90\%}$, is obtained when the ten-percent curve, marked in Figure 9.9 as the red line, exceeds this Q-value. The related median upper limit on the flux $\Phi^{up}_{90\%}$ can finally be gained with the help of $n^{up}_{90\%}$ and Equation 8.4, which linearly combines the acceptance (defined as n_{ref}/Φ_{ref}) with the number of signal events and the flux of interest (n_{CL}/Φ_{CL}). The value $\Phi^{up}_{90\%}$ and the discovery flux concerning a CL of $3\,\sigma$, $4\,\sigma$ and $5\,\sigma$, $\langle\,\Phi_{CL}\,\rangle$, are drawn over $QP2$ in the left diagram of Figure 9.12. The corresponding event numbers which have been gained from the MDP plot for a 50 % probability are visualised aside.

The $QP2$ cut, as part of the OSFFit cut combination, was varied from -20.0 to -5.0. For establishing limits on the signal flux, it has to be determined for which $QP2$ the expected number of signal events is minimal. This has been investigated using the *model rejection factor (MRF)* [98]. The MRF has to be minimised; its definition is shown in Equation 9.17. High values of the MRF indicate a weak constraint on the reference quantities n_{ref} and Φ_{ref}, whereas values < 1 constrain the model.

$$\mathrm{MRF} = \frac{n^{up}_{90\%}}{n_s} \tag{9.17}$$

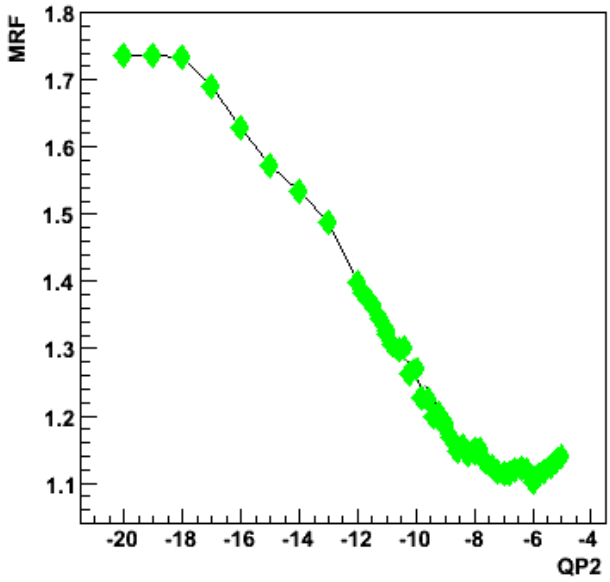

Figure 9.11: MRF over $QP2$ for candidate number 7. The smallest MRF value is assigned to the strongest constraint on the signal flux. Here, a MRF $\approx$ 1.10 is reached for $QP2 = -6.0$.

Here, n_{s} stands for n_{ref}, the number of signal events that pass the quality cuts. The expression $n_{90\%}^{\mathrm{up}}$ corresponds to the value mentioned above. The MRF values concerning variable $QP2$ are illustrated for source 7 in Figure 9.11.

The smallest MRF value ($\approx$ 1.10) is reached for $QP2 = -6.0$ as part of the final cut combination. The median upper limit that OSFFit obtains, defined as $\Phi_{90\%}^{\mathrm{up}}$ and evaluable with the help of Equation 8.4 and $n_{90\%}^{\mathrm{up}}$ as its denominator, is attached in the left plot of Figure 9.12. The corresponding number of events $n_{90\%}^{\mathrm{up}}$ is shown in the right diagram.

In Figure 9.12 it is noticable that for $QP2 > -15$ the shape of the 5σ curve lies above the 90% limit. As already explained, the cuts applied are quite strong. The interpretation is that if only a few galactic neutrino events are found the result indicates a discovery; for a $QP2 = -6$ its three events (with small angular separation from the source).

Finally, the events found in the 20° cone around source 7 with $QP2 = -6.0$ were examined. OSFFit was able to filter out five events; they are illustrated with red triangles in Figure 9.1. These events lie in the far distance of, on average, 6° from source 7; Equation 9.2 yielded a Q value of zero, which is in accordance with the background-only hypothesis. Therefore, the introduced (post-trial) p-value is set to 1 (see Equation 9.16). Chapter 10 summarises the results for all the sources over the declination with optimized MRF values.

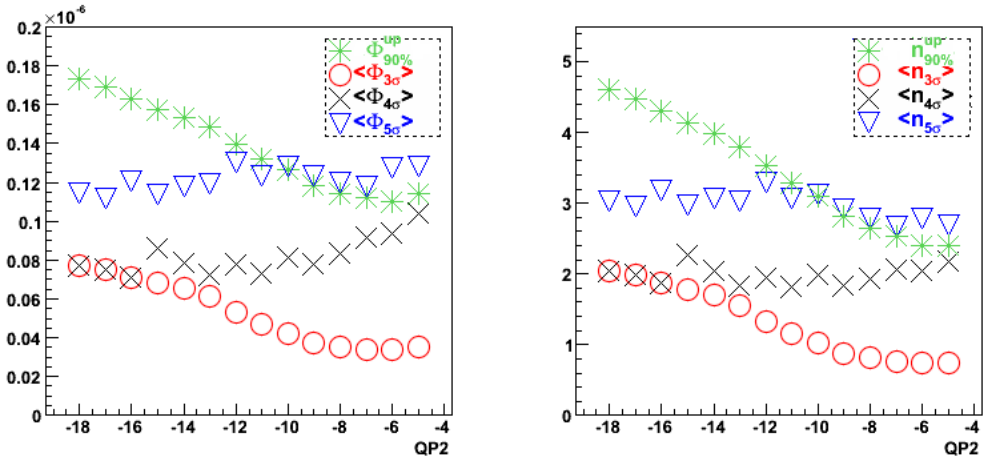

Figure 9.12: Left: Discovery flux $\langle\, \Phi_{\mathrm{CL}} \,\rangle$ for a CL of $3\,\sigma$, $4\,\sigma$ and $5\,\sigma$ over the quality cut $QP2$ for a 50 % probability. Star markers are related to the median upper limit of the flux for Monte Carlo data $\Phi^{\mathrm{up}}_{90\,\%}$; Right: Expectation value of the number of signal events $\langle\, n_{\mathrm{CL}} \,\rangle$ for a CL of $3\,\sigma$, $4\,\sigma$ and $5\,\sigma$ over the quality cut $QP2$ for a 50 % probability. Star markers are related to the median upper limit of the number of signal events for Monte Carlo data $n^{\mathrm{up}}_{90\,\%}$.

Chapter 10

Results of the analysis

In this chapter the results of the candidate search will be evaluated. They were strongly affected by the hard final OSFFit cuts. For none of the sources post-trial p-values smaller than 1 could be achieved for the 2007 and 2008 data, as not enough events could be found within the 20° search cone of each of the 24 sources.

The values of the averaged number of events $\langle\, n_{\mathrm{CL}} \,\rangle$ and fluxes $\langle\, \Phi_{\mathrm{CL}} \,\rangle$ for 50 % probability (see Figure 9.10) that are assigned the smallest MRF values of each source are drawn over the declination in Figure 10.1. The distribution starts to rise at a declination $\theta = -30°$, approaching the latitude of the ANTARES detector ($42° 50'$). This phenomenon is a consequence of the orientation of the PMTs within the detector; they have been set up to be sensitive for upwards moving muons. The median upper limit $\Phi^{\mathrm{up}}_{90\,\%}$ that OSFFit obtains for the 24 candidates is illustrated in the left plot of Figure 10.1 over the declination; the right plot corresponds to the number of events $n^{\mathrm{up}}_{90\%}$. Table 10.1 summarises all the values.

The lowest median upper limit $\Phi^{\mathrm{up}}_{90\,\%}$ of all sources was calculated for source 7. This neutrino source (HESS J1614-518) is a stellar cluster consisting of inter alia supernova remnants and pulsar wind nebulae [9] with a declination coordinate $\theta = -51.82°$. Five neutrino events with a median angular error of approximately 6° have been found in the surrounding search cone (20°). The associated median upper limit was calculated to:

$$\Phi^{\mathrm{up}}_{90\,\%} = 1.103 \cdot 10^{-7} \cdot \frac{1}{\mathrm{GeV} \cdot \mathrm{cm}^2 \cdot \mathrm{sec}} \tag{10.1}$$

The hard OSFFit cut set rejects approximately 50% of the triggered neutrino events (see Chapter 6.3). This is followed by quite high upper limits that are partly comparable with the 5σ discovery curve for each neutrino candidate. If only a few signal events with appropriate angular errors had detected ($\approx$ 3, see right plot in Figure 10.1), a discovery would have been made, but found events exhibited a to high angular error for any of the sources.

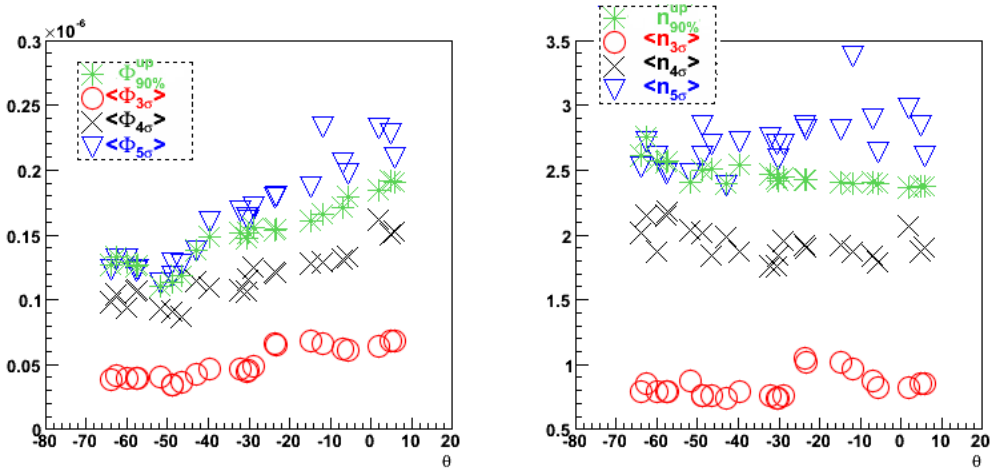

Figure 10.1: Discovery flux and number of signal events for a CL of $3\,\sigma$, $4\,\sigma$ and $5\,\sigma$ of each of the 24 source candidates over the declination. The median upper limit for a 90 % CL on the flux and the number of signal events is added in green. Here, only entries for the smallest MRF values reached are drawn.

Source number	Source	$QP2$	$\Phi^{\mathrm{up}}_{90\,\%}$	$\Phi_{3\sigma}$	$\Phi_{5\sigma}$
1	HESS J0632+057	-11.2	1.908	0.681	2.090
2	RX J0852.0-4622	-7.6	1.183	0.361	1.269
3	HESS J1023-575	-5.4	1.260	0.391	1.214
4	PSR B1259-63	-5.4	1.266	0.385	1.223
5	RCW 86	-6.0	1.331	0.410	1.312
6	Cir X-1	-5.4	1.265	0.390	1.227
7	HESS J1614-518	-6.0	1.103	0.402	1.128
8	GX 339	-6.8	1.130	0.346	1.179
9	RX J1713.7-3946	-8.6	1.489	0.465	1.594
10	Galactic Center	-9.4	1.560	0.487	1.714
11	W28	-10.6	1.550	0.650	1.789
12	LS 5039	-11.4	1.605	0.679	1.868
13	HESS J1837-069	-11.4	1.712	0.624	2.053
14	SS 433	-11.0	1.912	0.683	2.276
15	RGB J0152+017	-10.6	1.849	0.641	2.322
16	1ES 0347-121	-11.2	1.656	0.665	2.327
17	PKS 0548-322	-9.4	1.513	0.469	1.683
18	1ES 1101-232	-10.8	1.533	0.661	1.788
19	3C 279	-11.0	1.792	0.613	1.967
20	Centaurus A	-5.4	1.385	0.425	1.374
21	ESO 139-G12	-6.0	1.290	0.398	1.309
22	PKS 2005-489	-6.8	1.131	0.346	1.282
23	PKS 2155-304	-8.6	1.514	0.461	1.613
24	H 2356-309	-9.4	1.472	0.444	1.624

Table 10.1: List of candidate source locations that were searched for in this thesis. The three flux values have the unit $10^{-7}\,/(\mathrm{GeV}\cdot\mathrm{cm}^2\cdot\mathrm{sec})$. The green column marks the source with the lowest upper limit (source 7).

Chapter 11

Conclusion and outlook

In this thesis the reconstruction strategy OSFFit has been developed with the aim of finding and reconstructing neutrinos within the ANTARES telescope. Two years of data collected from January 2007 to December 2008 have been analysed; thereby, the relevant observation time was 1.17 years. One particularity of OSFFit is its analytical fit step. It incorporates a PDF (the SeaPdf) that uses an analytical description of the propagation of Cherenkov photons. In the simplest case such a PDF is the probability density distribution of the arrival time of Cherenkov photons at the photomultipliers. Almost all the PDFs that are contained within ANTARES neutrino reconstructions work with Monte Carlo information only. Thereby, for instance, tables are filled with the mentioned photon arrival times that are emitted from a simulated muon track. The approved AAFit strategy works with such kinds of Monte Carlo tables; it is the main algorithm used within the ANTARES collaboration so far. In contrast to that, the used analytical PDF is based on physical considerations and functions only. It can not be pointed out which of the two assumptions describe reality more truthfully: PDFs that result from physical functions or those that are gained from Monte Carlo information. This generally rectifies a reconstruction procedure that is based on such an analytical approach. Thereby, the angular difference of the reconstructed muon neutrinos to the Monte Carlo track served as mark of reconstruction quality. Further, it was figured out that OSFFit and AAFit are sensitive to partly disjunct event types concerning a dataset that was filtered out by both strategies. Finally, OSFFit was used to investigate a potential neutrino flux from 24 known γ-ray sources. As no source and also no evidence for sources could be validated, median upper limits on 90% CL were calculated. All introduced calculations have been performed in the SeaTray framework, which is the main analysis framework for ANTARES. Data-Monte Carlo comparisons were performed with RBR v 2.0 and RBR v 2.2 files.

In this work the ideas behind the design and the final constituents of OSFFit have been illuminated in detail. Beginning with the prefit, a mixture of hit selections, minimising algorithms, fit combinations and adjustment possibilities have been devised and tested. The interplay of all these components has been investigated in detail. The final

chain incorporates BBFit as its first rough track guess and three maximum likelihood fit steps for refining purposes. First, the BBFit track was multiplied 22 times. Thereby, six copies are shifted in a way, that they form a cylindrical shape around BBFit track; the other 16 copies are tilted around the original track in form of a double cone with the vertex point as the apex. Eventually, a final cut set was elaborated that consists of six cuts itself. It is applied on the residual fit result that was selected out of the 23 tracks by a cluster searching routine. The full OSFFit cut combination includes the BBFit quality cuts, the rdfClass, functions in dependency of the likelihood of the last two fits, the number of hits in the last fit and a cut on the reconstructed zenith angle. The final cut combination was set up with the goal of achieving proper efficiency for neutrinos and at the same time a suppression of the background. The data-taking periods where environmental variations influenced the rates and runs assigned a low quality flag were excluded from the analysis. The large residual amount of background was due to cosmic rays and presented the main challenge for OSFFit. For the neutrino energy estimation within the SeaPdf the program ANNergy [15] yielded the most convincing results.

Events have been analysed that surpassed both reconstructions successfully; they have been classified into four categories. One of them has been assigned to events that are well reconstructed with OSFFit and worse with AAFit. Diverse event properties of these datasets have been investigated as the number of lines and hits that contribute in the final fit step, the incoming vertical angle of the found events and others. It turns out that for a number of final hits below 50 and also below four contributing lines, OSFFit is more sensitive than AAFit. Concerning the associated reconstructed zenith angle error, OSFFit has a higher efficiency for horizontal incidenting neutrinos and AAFit for upward-going events. These effects influence roughly 1-2% of the common data set.

Further effort was directed towards the reconstruction of events that were rejected by AAFit and BBFit. AAFit's efficiency concerning 3N and T3 triggered events and an applied $\Lambda_{\mathrm{AAFit}} = -5.2$ could be improved by 2 %-5 %, whereas its median angular error remained nearly unaffected (0.30°). No useful solution could be gained for BBFit; the resulting angular errors are by far to large.

Concerning the amount of neutrinos in the final data sample OSFFit is comparable to AAFit. However, when it is adjusted to have the same suppression rate of atmospheric muons, its efficiency concerning cosmic neutrino events dramatically decreases. If all atmospheric muon events are suppressed, except one of a data sample with a lifetime of 20.7 days, OSFFit achieves a reconstruction efficiency of 12% concerning the triggered reference test sample, whereas AAFit achieves 23%. For the data-taking period from 2007 to 2008, AAFit yielded a median estimated angular error of $(0.53 \pm 0.08)^\circ$ [3]. OSFFit achieved for the same time period a median value of $\approx 1.23^\circ$.

Finally, 24 high-energy γ-ray sources were investigated with OSFFit concerning a potential neutrino emission. These sources include supernova remnants, microquasars and BL Lac objects. The reconstruction of neutrino signals originating from such an acceleration region could allow drawing conclusions about how particles come to their high velocities that have been detected on Earth. Furthermore, it could prove the scenario of a hadronic acceleration model instead of a leptonic. In this work, an unbinned likelihood ratio method has been used in order to search for an excess of signal events over the atmospheric neutrino background in a 20° cone around the mentioned sources. For all of them the background-only hypothesis turned out to be by far more likely. Therefore, limits on the flux and the number of detectable signals were derived. This was done with the help of pseudo experiments. The smallest median upper limit that could be reached by optimising for the lowest MRF was $\Phi^{\mathrm{up}}_{90\,\%} = 1.103 \cdot 10^{-7} \mathrm{GeV}^{-1} \cdot \mathrm{cm}^{-2} \cdot \mathrm{sec}^{-1}$ for the stellar cluster HESS J1614-518 [9]. Due to the low number of data events in the final event sample the 5σ discovery values are partly superimposed by the 90 % upper limits for all the neutrino candidates. A high number of well identified galactic neutrino events that are close to a source (3 to 4) are needed to indicate a discovery. This number could not be found for any of the candidates. Another consequence of the small residual event numbers are high post-trial p-values; all of them have been evaluated to 1. Although the calculated limits do not improve the already existing limits for the ANTARES telescope, they represent the first limits achieved by a reconstruction algorithm that incorporates an analytical approach.

With its analytical approach OSFFit represents an alternative reconstruction strategy. It finds neutrinos as accurate as AAFit, if background could be more selectively filtered out. The applied background suppression is not yet at the possible optimum. The cuts $QP1$ and $QP2$ that connect the knowledge of different likelihood probabilities represent promising quality cuts. More effort should be put into refining the hit selections that belong to the three main fits. Tuning this strategy to find event characteristics can be worth investigating; here, the zenith distribution shall be mentioned as an example, or the evidence for the higher efficiency at higher energies in the effective area plots. Furtheron, as OSFFit uses an analytical PDF, its results could yield hints for neutrino signals, that would not be gained with conventional reconstruction algorithms. Nevertheless, as a first step the hit selection should be optimized to gain a more precise angular resolution.

For eight years the ANTARES telescope has been detecting muon events. The range where possible neutrino emitters can be detected is being steadily constrained to lower limits. Related experiments such as IceCube and the planned KM3NeT are expected to be more efficient since they are larger in volume; scientists are waiting excitedly for a significant discovery that leads us one step deeper in neutrino physics.

Appendix A

First test sample

The first test sample is divided in atmospheric muons and muon neutrino events. It is used in Chapters 4 to 5. Input files for upward-going cosmic muon neutrinos analysed within this thesis are listed in Table A.1. They are located on the HPSS storage on the CC-IN2P3 cluster in Lyon, in the directory '/hpss/in2p3.fr/group/antares/-mc/neutrino/mu/dic08/r12_c00_s01/gea/up/' and contain all together roughly $5 \cdot 10^4$ physic frames. Their simulated neutrino energy spans from 10 GeV to 10^7 GeV. Each file is weighted with the cosmic weight $w2 \cdot E_\nu$, and constant factors are omitted. See [99] for more information.

gea.numu_lowe_1234_3.evt.bz2	gea.numu_lowe_1234_4.evt.bz2
gea.numu_lowe_1234_5.evt.bz2	

Table A.1: Input files for upgoing cosmic muon neutrinos for the first test sample.

Input files for atmospheric muons were generated with mupage version v3r5. Their production is extensively described in [100, 101]. The files used within the first test sample are listed in Table A.2; they are located on the HPSS storage on the CC-IN2P3 cluster in Lyon in the directory '/hpss/in2p3.fr/group/antares/mc/muon/mupage/-dec08/r12_c00_s01/km3v3r6/' and were randomly chosen. In total, these files contain roughly $7.2 \cdot 10^6$ frames with a lifetime of roughly 16 h. They are weighted only with $w3$ (Bartol flux).

km3.mupagev3r4.run_0001.evt.bz2	km3.mupagev3r4.run_0016.evt.bz2
km3.mupagev3r4.run_0060.evt.bz2	km3.mupagev3r4.run_0120.evt.bz2
km3.mupagev3r4.run_0180.evt.bz2	km3.mupagev3r4.run_0240.evt.bz2
km3.mupagev3r4.run_0300.evt.bz2	

Table A.2: Input files for atmospheric muons for the first test sample (mupagev3r5).

Appendix B

Second test sample

The second test sample is used in Chapters 6.3 to 6.6. Table B.1 lists parts of RBR files v 2.0 and v 2.2 that are used in this thesis. Therein, for the generation of high-energetic shower files, the so-called *One-Particle Approximation (OPA)* was applied. In the OPA, a single particle with a certain charge stands for a whole shower event [102]. The whole RBR generation is documented in more detail in [67, 103].
In Table B.1 the values (a), (b) and (x) stand for different energy ranges which partly overlap. It is up to the user to remove the overlap for an analysis. Furthermore, the user has to adopt the correct flux assumption for each event. Therefore, within SeaTray, the cosmic and atmospheric weights $w2$ and $w3$ are provided.

signature	neutrino energy [GeV]	v	OPA	weight
ν_e CC	(a) $100 - 10^5$	v2.0		w2 / w3
$\overline{\nu}_e$ CC	(a) $100 - 10^5$	v2.0		w2 / w3
ν_e CC	(b) $5 \cdot 10^4 - 10^8$	v2.0	OPA	w2 / w3
$\overline{\nu}_e$ CC	(b) $5 \cdot 10^4 - 10^8$	v2.0	OPA	w2 / w3
ν_e NC	(a) $100 - 10^5$	v2.0		w2 / w3
$\overline{\nu}_e$ NC	(a) $100 - 10^5$	v2.0		w2 / w3
ν_e NC	(b) $5 \cdot 10^4 - 10^8$	v2.0	OPA	w2 / w3
$\overline{\nu}_e$ NC	(b) $5 \cdot 10^4 - 10^8$	v2.0	OPA	w2 / w3
ν_e NC	(x) $4 - 300$	v2.2		w2 / w3
$\overline{\nu}_e$ NC	(x) $4 - 300$	v2.2		w2 / w3
ν_e CC	(x) $4 - 300$	v2.2		w2 / w3
$\overline{\nu}_e$ CC	(x) $4 - 300$	v2.2		w2 / w3
ν_μ CC	(a) $5 - 20 \cdot 10^3$	v2.2		w2 / w3
$\overline{\nu}_\mu$ CC	(a) $5 - 20 \cdot 10^3$	v2.2		w2 / w3
ν_μ CC	(b) $20 \cdot 10^3 - 10^8$	v2.2		w2 / w3
$\overline{\nu}_\mu$ CC	(b) $20 \cdot 10^3 - 10^8$	v2.2		w2 / w3
ν_μ NC	(a) $100 - 10^5$	v2.0		w2 / w3
$\overline{\nu}_\mu$ NC	(a) $100 - 10^5$	v2.0		w2 / w3
ν_μ NC	(b) $5 \cdot 10^4 - 10^8$	v2.0	OPA	w2 / w3
$\overline{\nu}_\mu$ NC	(b) $5 \cdot 10^4 - 10^8$	v2.0	OPA	w2 / w3
ν_μ NC	(x) $4 - 300$	v2.2		w2 / w3
$\overline{\nu}_\mu$ NC	(x) $4 - 300$	v2.2		w2 / w3
mupage atm. μ	adjusted	v2.0		w3

Table B.1: List of used RBR input files (version 2.0 and 2.2). If the OPA was used in the RBR shower generation, it is marked (for completenes only). Furthermore, for each signature, the simulated energy window is shown, as well as the cosmic and atmospheric weights $w2$ and $w3$ that were applied in this thesis.

Appendix C

Simple fit sequences

Among several fit sequences, AO-S-AF has been proven to be the most convenient. Figure C.1 shows the angular error histogram of simple fit sequences with the Monte Carlo track *(mctrack)* as prefit. This prefit was multiplied 23 times as described in Chapter 5.2 and also the hit selection was identically composed. The *mctrick* was applied, meaning that out of the 23 fits this track was chosen, which has the smallest angular difference to the Monte Carlo track. Contained are five rudimentary fits including the *AartOriginalPdf (AO)*, the *SeaPdf (S)* and the *PandelPdf (P)*. Two fits are arranged in a row: *AO-S* and *P-S*. Corresponding tilt angles had been figured out in several optimisation studies. As can be seen, the combination *AO-S* seems to be the most lucrative, favouring the connection of more fits in a row instead of using only one fit. In Figure 5.11 *AO-S* is added among a lot of other more complex combinations.

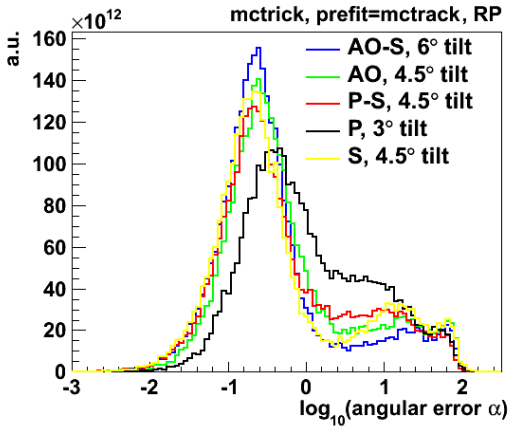

Figure C.1: Angle error distribution of rudimentary fit chains with the Monte Carlo track as prefit. The tilt angles came out after several optimisation processes.

Appendix D

Vertical incidenting muons

A further distinguishing feature is the initial zenith direction of the muon. The horizontal case for different energy regimes has been illustrated in Chapter 6.1. Here, cumulative plots of the angular error of events with zenith angles from 165° to 195° are shown (the vertical case). The input files only contain a few events at this high zenith angles. The following plots are divided into three different energy zones with regard to the Monte Carlo muon energy E_μ: $E_\mu \leqq 5\,\mathrm{TeV}$, $5\,\mathrm{TeV} < E_\mu \leqq 10\,\mathrm{TeV}$ and $10\,\mathrm{TeV} < E_\mu \leqq 20\,\mathrm{TeV}$ (see Figures D.1 to D.3). For the whole energy range ($4\,\mathrm{GeV} < E_\nu \leqq 10^8\,\mathrm{GeV}$) see Figure D.4. Figure D.5 shows the same for horizontal events. In all these plots, it is still cut on Λ_{AAFit} and Λ_{pot}. Concerning the vertical events AO-S-AF is competitive to AAFit only for very small angular errors up to $\approx 0.1°$ (see Figures D.1 to D.4).

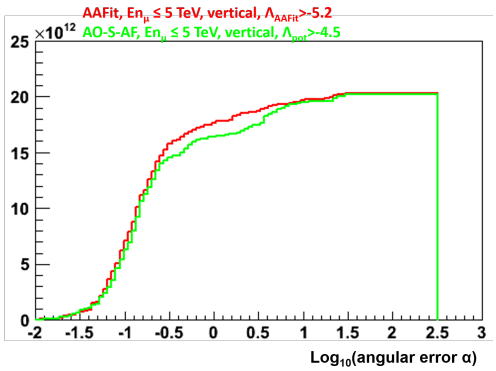

Figure D.1: Vertical muons with Monte Carlo muon energy $E_\mu < 5\,\mathrm{TeV}$. It is cut on $\Lambda_{\mathrm{pot}} > -4.5$ and $\Lambda_{\mathrm{AAFit}} > -5.2$.

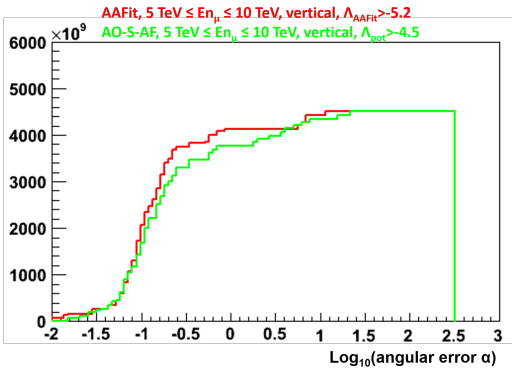

Figure D.2: Vertical muons with Monte Carlo energy between 5 TeV and 10 TeV. It is cut on $\Lambda_{\mathrm{pot}} > -4.5$ and $\Lambda_{\mathrm{AAFit}} > -5.2$.

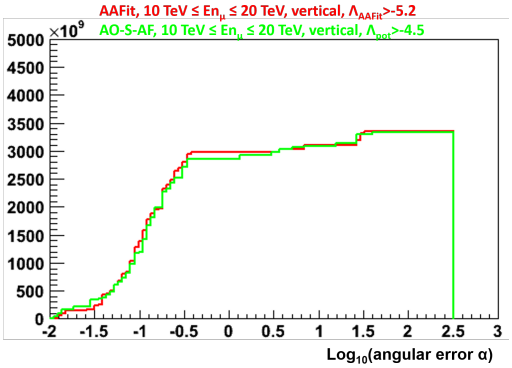

Figure D.3: Vertical muons with Monte Carlo energy between 10 TeV and 20 TeV. It is cut on $\Lambda_{\mathrm{pot}} > -4.5$ and $\Lambda_{\mathrm{AAFit}} > -5.2$.

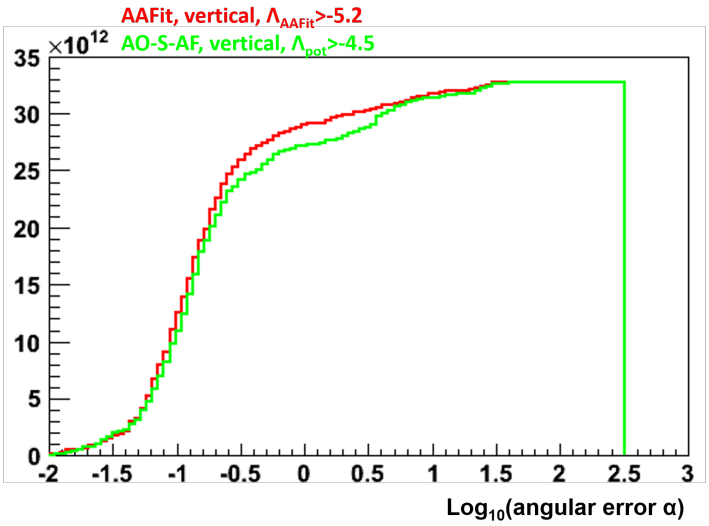

Figure D.4: Cumulative angular error distribution of vertical muons (165° to 195°). It is cut on $\Lambda_{\mathrm{pot}} > -4.5$ and $\Lambda_{\mathrm{AAFit}} > -5.2$.

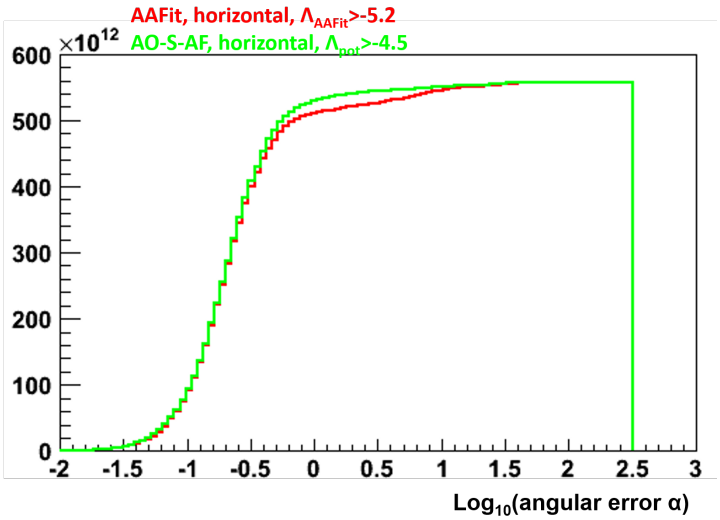

Figure D.5: Cumulative angular error distribution of horizontal muons (75° to 105°). It is cut on $\Lambda_{\mathrm{pot}} > -4.5$ and $\Lambda_{\mathrm{AAFit}} > -5.2$.

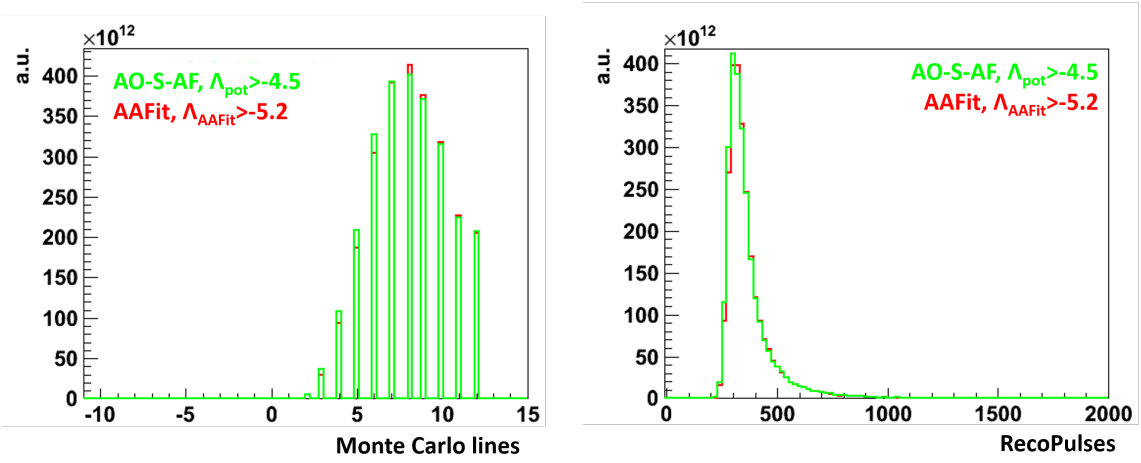

Figure D.6: Histogram of Monte Carlo lines and input pulses which belong to an event that survives the given cuts. Here, no cut on the angular error α has been performed.

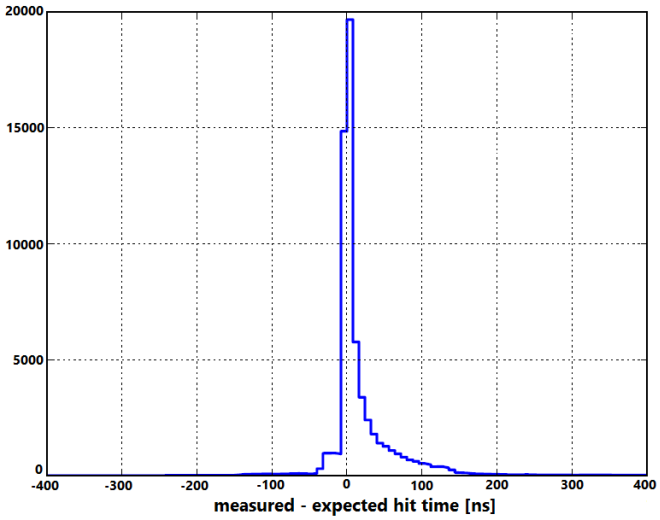

Figure D.7: The SeaTray module *I3RemovePulsesAfterARSDeadTime* filters out all information of the second ARS and also the data after the dead time of the first ARS (250 ns). This cut is motivated as the pulses are assumed to mainly belong to scattered hits or late pulses. The second test sample described in B was used for this diagram.

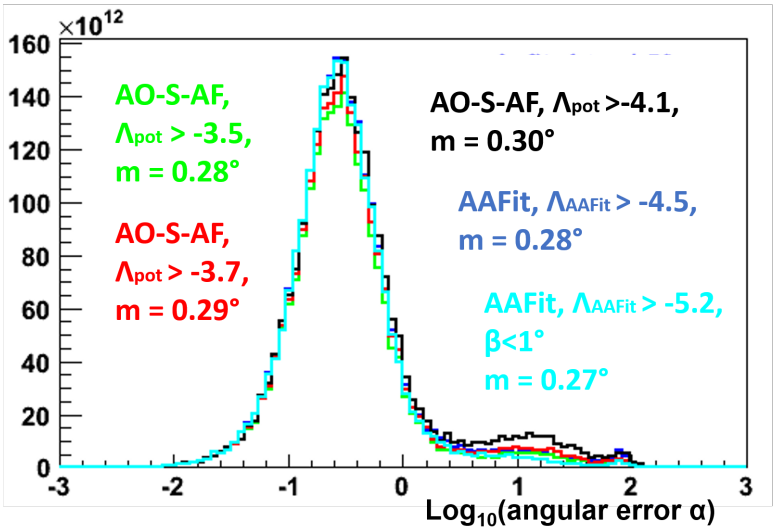

Figure D.8: Angular error histogram with different cut values on Λpot of Equation 5.1. For the light blue AAFit curve also the intrinsic cut value $\beta < 1^\circ$ is applied.

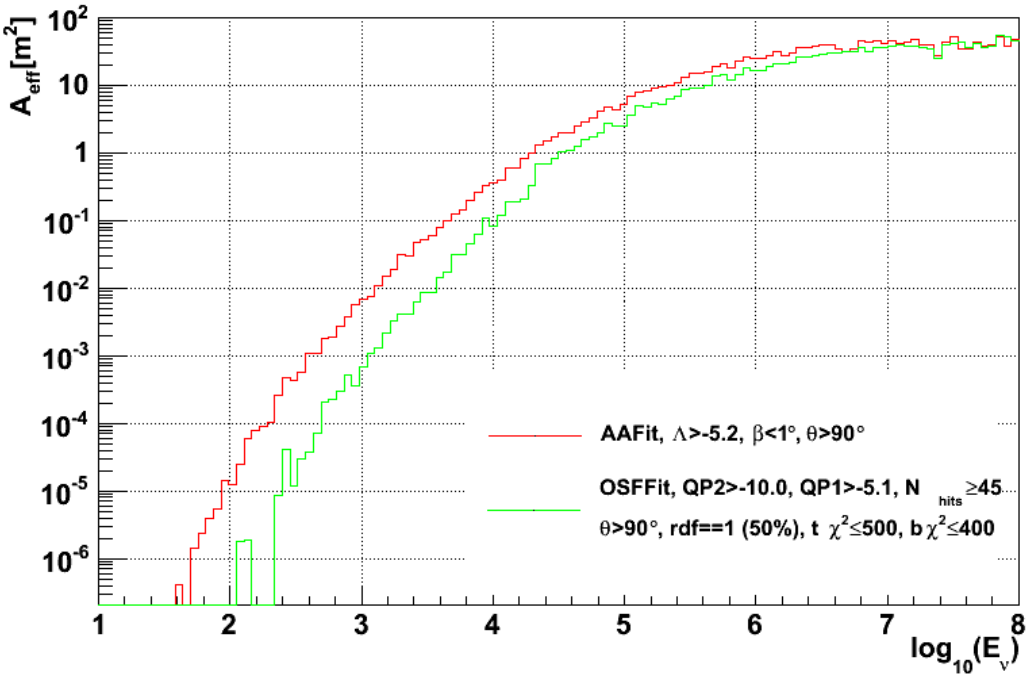

Figure D.9: Effective areas of AAFit in red and OSFFit in green for neutrinos that were reconstructed with an angular error $\alpha < 1^\circ$, respectively.

Appendix E

PDFs of other source locations

Chapter 10 reports about the results of the candidate search. The most promising source, source 7, is located at a small declination coordinate $\sin\theta \approx -0.79$. The MRF values, signal and background distributions of two sources that are assigned with middle and high declination values are shown in Figures E.1 to E.6.

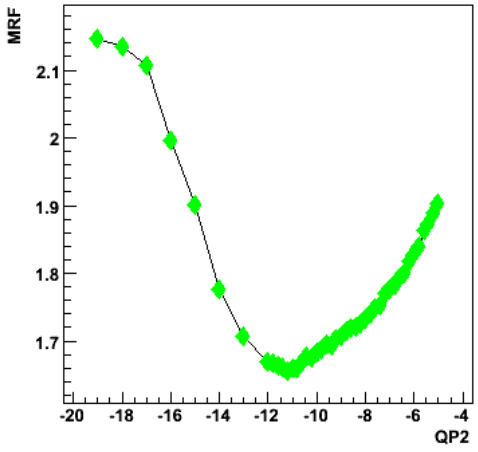

Figure E.1: MRF distribution of source 16 with declination coordinate $\sin\theta \approx -0.21$. The smallest MRF value 1.66 is reached for $QP2 = -11.2$.

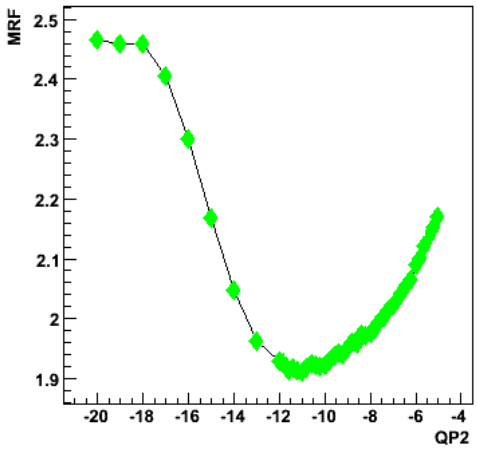

Figure E.2: MRF distribution of source 14 with declination coordinate $\sin\theta \approx 0.09$. The smallest MRF value 1.92 is reached for $QP2 = -11$.

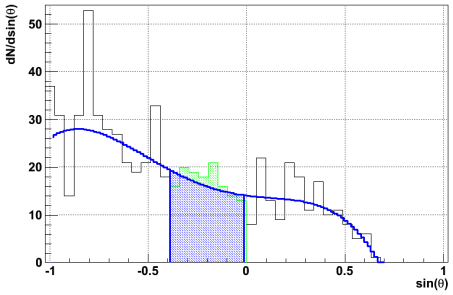

Figure E.3: Background probability density function $dN/d\sin\theta$. The shaded region is assigned to the search cone around source 16. The background probability density function $dN/d\sin\theta$ is overlaid by a polynomial of fourth power (in blue).

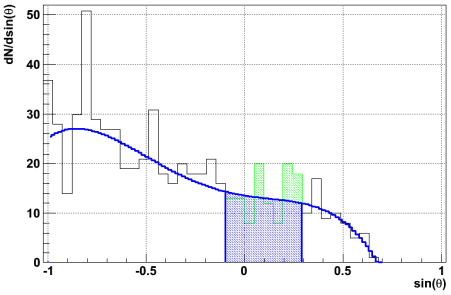

Figure E.4: Background probability density function $dN/d\sin\theta$. The shaded region is assigned to the search cone around source 14. The background probability density function $dN/d\sin\theta$ is overlaid by a polynomial of fourth power (in blue).

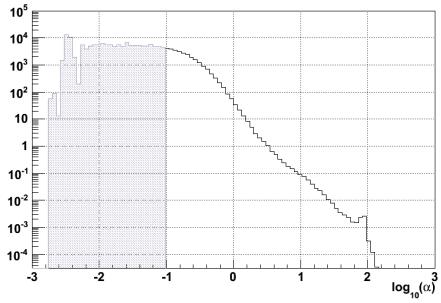

Figure E.5: Point spread function for a 20° cone around the source coordinates of source number 16.

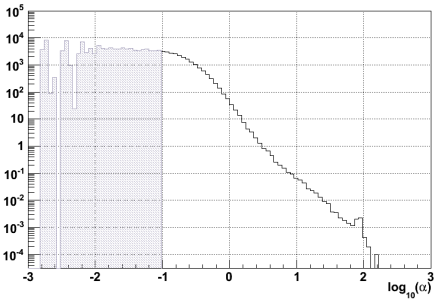

Figure E.6: Point spread function for a 20° cone around the source coordinates of source number 14.

Bibliography

[1] The IceCube Collaboration. Evidence for high-energy extraterrestrial neutrinos at the IceCube detector. *Science*, 342(6161), 2013.

[2] M. G. Aartsen et al. Observation of high-energy astrophysical neutrinos in three years of IceCube data. *Phys. Rev. Lett.*, 113:101101, 2014.

[3] C. Bogazzi, J. Hartman, A. Heijboer. Point Source Search with 2007 and 2008 data. ANTARES internal note ANTARES-SOFT-2010-008, 2010.

[4] The ANTARES Collaboration. Search for Cosmic Neutrino Point Sources with Four Years of Data from the ANTARES Telescope. Jul 2012. Available online at `http://arxiv.org/abs/1207.3105v2`.

[5] J. Brunner. The BBfit Reconstruction algorithm. ANTARES internal note ANTARES-SOFT-2009-012, 2009.

[6] G. Halladjan. Search for neutrino point sources in the antares 2007 data using bbfit (update). Presented at the AWG meeting, June, 2009.

[7] C. Bogazzi. Point source search with 2007-2010 data. ANTARES-PHYS-2011-005, 2011.

[8] S. Adrián-Martínez et al. Search for cosmic neutrino point sources with four years of data from the ANTARES telescope. *Astrophys. J.*, 760(1):53, 2012.

[9] The H.E.S.S. Collaboration. H.E.S.S. observations of massive stellar clusters. *High Energy Phenomena in Massive Stars ASP Conference Serie*, 422:265, 2010.

[10] M. Ageron et al. ANTARES: The first undersea neutrino telescope. *Nucl. Inst. and Meth. A*, 656:11–38, 2011.

[11] J. Beringer et al. (Particle Data Group). Neutrino mass, mixing, and flavor change. *Phys. Rev. D*, 86(010001):177–198, 2012.

[12] The KM3NeT Collaboration. KM3NeT - Conceptual design report for a deep-sea research infrastructure in the Mediterranean Sea incorporating a very large volume neutrino telescope, 2008. Available online at `http://www.km3net.org/CDR/CDR-KM3NeT.pdf`.

[13] D. Chirkin, W. Rhode. Muon Monte Carlo: a high-precision tool for muon propagation through matter. 2004. Available online at `http://arxiv.org/abs/hep-ph/0407075v1`.

[14] M. de Jong. The probability density function of the arrival time of light. ANTARES internal note ANTARES-SOFT-2010-002, 2010.

[15] J. Schnabel. The ANNergy estimator - Using Artificial Neural Networks for muon energy reconstruction. ANTARES internal note ANTARES-SOFT-2012-010, 2012.

[16] E. Visser, S. Wagner. Studies of the performance of different track reconstruction strategies using the FilteringFit track reconstruction. ANTARES internal note ANTARES-SOFT-2013-002, 2013.

[17] C. Grupen. *Astroparticle physics*. Springer-Verlag Berlin Heidelberg New-York, 2005.

[18] N. Schmitz. *Neutrinophysik*. Teubner-Studienbcher, 1997.

[19] F. Halzen. The Search for the Sources of the Cosmic Rays One Century after their Discovery. 2010. Available online at `http://arxiv.org/abs/1010.0235v1`.

[20] Z. Xing, S. Zhou. *Neutrinos in Particle Physics, Astronomy and Cosmology*. Springer-Verlag Berlin Heidelberg, 2011.

[21] Pierre Auger Observatory. A Timeline of High-Energy Cosmic Rays History. Website, 2014. Available online at `http://www.auger.org/cosmic_rays/timeline.html`.

[22] J.R. Hoerandel. Cosmic Rays from the Knee to the Highest Energies. *Prog. Part. Nucl. Phys.*, 63(1):293–338, 2009.

[23] J. R. Hoerandel. On the knee in the energy spectrum of cosmic rays. *Astropart. Phys.*, 19(2):193–220, 2003.

[24] T. Chiarusi, M. Spurio. High Energy Astrophysics with Neutrino Telescopes. *Eur. Phys. J. C*, 65(v1):649–701, 2009.

[25] P. Blasi. Origin of Galactic Cosmic Rays, 2012. Available online at `http://arxiv.org/abs/1211.4799v1`.

[26] A. Haungs. Cosmic Rays from the Knee to the Ankle. *Phys. Procedia*, 61:425–434, 2015.

[27] S. Knurenko, Z. Petrov, R. Sidorov, I. Sleptsov, S. Starostin, G. Struchkov. Cosmic ray spectrum in the energy range $10^{15} - 10^{18}$ eV and the second knee according to the small Cherenkov setup at the Yakutsk EAS array. Available online at `http://arxiv.org/abs/1310.1978v1`.

[28] U. Katz, C. Spiering. High-energy neutrino astrophysics: Status and perspectives. *Progress in Particle and Nuclear Physics*, 67(3):651–704, 2012.

[29] The Pierre Auger Collaboration. Observation of the suppression of the flux of cosmic rays above $4x10^{19}eV$. *Phys. Rev. Lett.*, 101(061101), 2008.

[30] HiRes Collaboration. Final Results from the High Resolution Fly's Eye (HiRes) Experiment. *Nuclear Physics B (Proceedings Supplements*, 212:74–78, 2011.

[31] Telescope Array Collaboration. The Cosmic Ray Energy Spectrum Observed with the Surface Detector of the Telescope Array Experiment. *Astrophys. J. Letters*, 768(L1), 2013.

[32] K. Kampert, P. Tinyako. Cosmic rays from the ankle to the cutoff. *Comptes Rendus Physique*, 15:318–328, 2014.

[33] E. Fermi. On the Origin of the Cosmic Radiation. *Phys. Rev.*, 75(8):1169–1174, 1949.

[34] A. Bell. The acceleration of cosmic rays in shock fronts - I. *Mon. Not. R. astr. Soc.*, 182:147–156, 1978.

[35] K. Kotera, A. V. Olinto. The Astrophysics of Ultrahigh Energy Cosmic Rays, 2011. Available online at `http://arxiv.org/abs/1101.4256`.

[36] J. Gonzaléz. Search for point sources of high energy neutrinos with 2007-10 data. ANTARES internal note ANTARES-SOFT-2011-006, 2011.

[37] S. Wakely, D. Horan. Welcome to TeVCat. Website, 2014. Available online at `http://tevcat.uchicago.edu`.

[38] W. Bednarek. Neutrinos from the pulsar wind nebulae. *Astronomy and Astrophysics*, 407:1–6, 2003.

[39] W. Bednarek, M. Bartosik. Gamma-rays and neutrinos from the pulsar wind nebulae. *Nuovo Cim. B*, 120:751–755, 2005.

[40] F. Aharonian, L. Anchordoqui, D. Khangulyan, T. Montaruli. Microquasar LS 5039: a TeV gamma-ray emitter and a potential TeV neutrino source. *J. Phys. Conf. Ser.*, 39(1):408–415, 2006.

[41] G. E. Romero, D. F. Torres, M. M. Kaufman Bernadó, I.F. Mirabel. Hadronic gamma-ray emission from windy microquasars. *Astron. Astrophys.*, 410(2):L1–L4, 2003.

[42] W. Bednarek. TeV neutrinos from microquasars in compact massive binaries. *Astrophys. J.*, 631:466, 2005.

[43] M. Su et al. Giant gamma-ray bubbles from Fermi-LAT: Active galactic nucleus activity or bipolar galactic wind? *Astrophys. J.*, 724(2):1044, 2010.

[44] C. Lunardini, S. Razzaque. High Energy Neutrinos from the Fermi Bubbles. *Phys. Rev. Lett.*, 108:221102, 2012.

[45] P. Mészáros. Ultra-high Energy Cosmic Rays and Neutrinos from Gamma-Ray Bursts, Hypernovae and Galactic Shocks. *Nuclear Physics B*, 256-257:241–251, 2014.

[46] S. Adrián-Martínez et al. Search for muon neutrinos from gamma-ray bursts with the ANTARES neutrino telescope using 2008 to 2011 data. *A&A*, 559:A9, 2013.

[47] R. Abbasi et al. An absence of neutrinos associated with cosmic-ray acceleration in γ-ray bursts. *Nature*, 484:351–354, 2012.

[48] The ANTARES Collaboration. ANTARES proposal - A deep sea telescope for high energy neutrinos, 1999. Available online at `http://antares.in2p3.fr/Publications/index.html`.

[49] K. Nakamura et al. *Particle Physics booklet.* Particle data group at LBNL and CERN, 2010.

[50] F. Schüssler et al. Energy reconstruction in neutrino telescopes. Proceedings of the ICRC 2013 conference, Available online at `http://arxiv.org/pdf/1312.4308v1.pdf`.

[51] C. Kopper. Energy reconstruction of high-relativistic muon neutrinos with the Water-Čerenkov-Telescope ANTARES. Diploma thesis, University of Erlangen-Nürnberg, 2005.

[52] A. Heijboer. Shower Direction Reconstruction for Antares: aashowerfit. ANTARES internal note ANTARES-SOFT-2014-002, 2014.

[53] T. Michael, J. Marti, A. Heijboer. Point Source Search using Tracks and Showers. ANTARES internal note ANTARES-SOFT-2015-003, 2015.

[54] A. Bhattacharya et al. The Glashow resonance at IceCube: signatures, event rates and pp vs. pγ interactions. *JCAP*, 2011(10):017, 2011.

[55] D. Zaborov. The K-40 calibration method. ANTARES internal note ANTARES-CALI-2011-001, 2011.

[56] S. Escoffier, A. Cussatlegras. Correlations between bioluminescence and environmental parameters with ANTARES data in 2003 (PSL) and 2005 (MILOM). ANTARES internal note ANTARES-PHYS-2006-007, 2006.

[57] S. Adrián-Martínez et al. Measurement of the atmospheric ν_μ energy spectrum from 100 GeV to 200 TeV with the ANTARES telescope. *Eur. Phys. J. C*, 73(10):1434–6044, 2013.

[58] A. Martin, M. Ryskin, A. Stasto. Prompt neutrinos from atmospheric $c\bar{c}$ and $b\bar{b}$ production and the gluon at very small x. *Acta Phys. Polon. B, volume = 34*, pages 3273–3304, 2003.

[59] The ANTARES Collaboration. Experiment documentation. Website. Available online at `http://antares.in2p3.fr/`.

[60] V. Van Elewyck. Recent results from the ANTARES neutrino telescope . *Nucl. Instrum. Methods Phys. Res. A*, 742:63–70, 2014.

[61] J. A. Aguilar et al. The data acquisition system for the ANTARES neutrino telescope. *Nucl. Inst. and Meth. A*, 570(1):107–116, 2007.

[62] The ANTARES Collaboration. Study of Large Hemispherical Photomultiplier Tubes for the ANTARES Neutrino Telescope. *Nucl. Instrum. Methods Phys. Res., A*, 555:132–141.

[63] B. A. P. van Rens. The software trigger in ANTARES. ANTARES internal note ANTARES-SOFT-2004-001, 2004.

[64] M. De Jong. The ANTARES trigger software. ANTARES internal note ANTARES-SOFT-2005-005, 2005.

[65] T. Seitz R. Shanidze, B. Herold. Study of data filtering algorithms for the km3net neutrino telescope. Presented at the VLVnT-09 in Athens, 2009.

[66] C. Kopper. Application of icecube software framework to water detectors. Presented at the WP2 session at Pylos, 2007.

[67] C. Rivière. Run-by-run Monte Carlo simulation for ANTARES: v2. ANTARES internal note ANTARES-PHYS-2012-001, 2012. Version 6.

[68] P. Coyle. ANTARES Introduction, p6. Presented at the collaboration meeting in Leiden, 2014.

[69] The Apache Software Foundation. Apache Subversion. Website. Available online at `http://subversion.apache.org`.

[70] The GNU Scientific Library (GSL). Quasi-random number generator algorithms. Website, 2013. Available online at `http://www.gnu.org/software/gsl/manual/html_node/Quasi_002drandom-number-generator-algorithms.html`.

[71] F. James. MINUIT Function Minimization and Error Analysis. *Cern Program Library*, D506, 1994. Reference Manual.

[72] M. Roos F. James. Minuit - a system for function minimization and analysis of the parameter errors and correlations. *Comput. Phys. Commun.*, 10:343–367, 1975.

[73] N. Hansen. *The CMA Evolution Strategy: A Tutorial*, January 2009. Continuously updated technical report, available online at `https://www.lri.fr/~hansen/cmatutorial.pdf`.

[74] N. Hansen, S. Kern. Evaluating the CMA Evolution Strategy on Multimodal Test Functions, 2004. Proceedings of International Conference on Parallel Problem Solving from Nature PPSN VIII.

[75] N. Hansen, A. Ostermeier. Completely Derandomized Self-Adaptation in Evolution Strategies. *Evolutionary Computation*, 9(2):159–195, 2001.

[76] G. Japaridzea, M. Ribordyb. Realistic arrival time distribution from an isotropic light source, 2005. Available online at `http://arxiv.org/abs/astro-ph/0506136v1`.

[77] N. van Eijndhoven, O. Fadiran, G. Japaridze. Implementation of a Gauss convoluted Pandel PDF for track reconstruction in Neutrino Telescopes, 2007. Available online at `http://arxiv.org/abs/0704.1706v2`.

[78] C. Kopper. *Performance Studies for the KM3NeT Neutrino Telescope*. PhD thesis, University of Erlangen-Nürnberg, 2010.

[79] The IceCube Collaboration. First observation of PeV-energy neutrinos with IceCube, 2013. Available online at `http://arxiv.org/abs/1304.5356`.

[80] The IceCube Collaboration. Search for time-independent neutrino emission from astrophysical sources with 3 years of IceCube data, 2013. Available online at `http://arxiv.org/abs/1307.6669`.

[81] The IceCube Collaboration. First Neutrino Point-Source Results From the 22-String IceCube Detector. *Astrophys. J.*, 701(1):L47, 2009.

[82] A. Heijboer. *Track Reconstruction and Point Source Searches with ANTARES*. PhD thesis, University of Amsterdam, 2004.

[83] The AMANDA Collaboration. Muon Track Reconstruction and Data Selection Techniques in AMANDA. *Nucl. Instrum. Meth. A*, 524:169–194, 2004.

[84] S. Escoffier. Performance of the T3 triggers on MC data. ANTARES internal note ANTARES-SOFT-2008-009, 2008.

[85] T. Neunhöffer. *Die Entwicklung eines neuen Verfahrens zur Suche nach kosmischen Neutrino-Punktquellen mit dem AMANDA-Neutrinoteleskop*. PhD thesis, Johannes-Gutenberg-University in Mainz, 2003.

[86] T. Neunhöffer. Estimating the angular resolution of tracks in neutrino telescopes based on a likelihood analysis. *Astropart. Phys.*, 25:220–225, 2006.

[87] The IceCube collaboration. IC-40 PS Cut Variables. Website. Available online at `https://wiki.icecube.wisc.edu/index.php/IC-40_PS_Cut_Variables`.

[88] S. Geisselsoeder. RDFClassify Tutorial. ANTARES internal note ANTARES-SOFT-2012-002, 2012.

[89] G. Halladjian, P. Coyle. Search for Neutrino Point Sources in the ANTARES 2007 Data Using BBfit. 2010.

[90] D. J. L. Bailey. Calculating effective areas for neutrinos. ANTARES internal note ANTARES-PHYS-2001-011, 2001.

[91] J. P. Snyder. *Map Projections–A Working Manual.* United States Government Printing, 1983.

[92] J. R. Barlow. *Statistics.* Wiley-Verlag Chichester, 1999.

[93] H. Georgii. *Stochastik.* Walter de Gruyter & Co., Berlin, 2009.

[94] S. Wagner. Private communication. ECAP, University of Erlangen-Nürnberg.

[95] The ROOT team. ROOT - A data analysis framework. Website. Available online at `http://root.cern.ch/`.

[96] E. Weisstein. Great Circle, From MathWorld–A Wolfram Web Resource. Website. Available online at `http://mathworld.wolfram.com/GreatCircle.html`.

[97] H. Anton. *Lineare Algebra: Einführung, Grundlagen, Übungen.* Spektrum Akademischer Verlag, Heidelberg, Berlin, 1998.

[98] G. C. Hill et al. Unbiased cut selection for optimal upper limits in neutrino detectors: The model rejection potential technique. *Astropart. Phys.*, 19(3):393–402, 2003.

[99] The ANTARES Collaboration. ANTARES HPSS Data Summary. Website. Available online at `http://antares.in2p3.fr/internal/software/prod_hpss/nu_prod0401.txt`.

[100] M. Bazzotti et al. An update of the generator of atmospheric muons from parametric formulas (MUPAGE). *Comp. Phys. Comm.*, 181(4):835–836, 2010.

[101] G. Carminati et al. Atmospheric MUons from PArametric formulas: a fast GEnerator for neutrino telescopes (MUPAGE). *Comp. Phys. Comm.*, 179(12):915–923, 2008.

[102] M. Dentler. Investigation of the One-Particle Approximation in the ANTARES simulation package KM3. Bachelor thesis, University of Erlangen-Nürnberg, 2012. Available online at `http://www.ecap.physik.uni-erlangen.de/publications/pub/2012_Dentler_Bachelor.pdf`.

[103] L. A. Fusco. Status of the RBR 2012. Presented at the collaboration meeting in Marseille, 2013.